Norwegian University of
Science and Technology

Comparative Study of CdZnTe Substrates Prepared by Different Methods

Oda Lauten

Master of Science in Physics and Mathematics
Submission date: June 2017
Supervisor: Turid Worren Reenaas, IFY
Co-supervisor: Randi Haakenaasen, Forsvarets forskningsinstitutt

Norwegian University of Science and Technology
Department of Physics

Comparative Study of CdZnTe Substrates Prepared by Different Methods

Oda Lauten

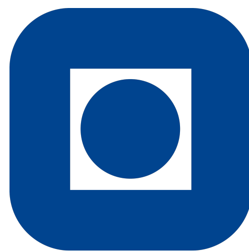

Department of Physics
Faculty of Natural Sciences
Norwegian University of Science and Technology

June 2017

NTNU

Norwegian University of Science and Technology

Department of Physics
Faculty of Natural Sciences

Oda Lauten: *Comparative Study of CdZnTe Substrates Prepared by Different Methods*, June 2017

Supervisors:
Randi Haakenaasen, Norwegian Defence Research Establishment (FFI), Kjeller, Norway
Turid Worren Reenaas, Norwegian University of Science and Technology, Trondheim, Norway

Location:
Norwegian Defence Research Establishment (FFI), Kjeller, Norway

Printed by NTNU-trykk

Preface

This master's thesis is submitted as the final work required for the Master's degree (MSc) in Applied Physics and Mathematics at the Norwegian University of Science and Technology (NTNU). The study presented in this thesis was carried out at the Norwegian Defence Research Establishment (FFI) from January to June 2017 under the supervision of Professor Randi Haakenaasen.

The study was a continuation of the Specialisation Project in Physics (TFY4510, 15 ECTS), as presented in the author's report titled "Characterisation of As-Received CdZnTe Substrates" (Lauten, 2017). Some of the results are reiterated here in order to better present the full scope of the study that has been performed during the final year of my MSc studies.

I would like to thank Professor Randi Haakenaasen for giving me the possibility to carry out the work presented in this thesis. I am grateful for the valuable discussions and guidance during my work. I would also like to thank Chief Scientist Espen Selvig at FFI for his patient advice and follow up in the development of this work; Associate Professor Turid Worren Reenaas at NTNU for taking the time to read my thesis and provide useful feedback; Senior Scientist Kjell Ove Kongshaug and Technician Laila Trosdahl-Iversen at FFI for demonstrating the preparation methods used before epitaxial growth; and Senior Engineer Torgeir Lorentzen at FFI for giving me training at the atomic force microscope and for generally being helpful in practical matters.

Oda Lauten
Kjeller, Norway
June 2017

Abstract

In this study, three different $Cd_{1-y}Zn_yTe$ (CZT) substrates were characterised for surface impurity contamination, particles, and defects. The substrates were examined both as-received and after surface pre-growth preparation. As the final step, a layer of $Hg_{1-x}Cd_xTe$ (MCT) film was grown on each substrate and examined. It is of great interest to obtain a better understanding of how impurities, defects, and particles on the CZT substrate surface affect the quality of the grown MCT film.

Two of the substrates were (111)B-oriented and used for liquid phase epitaxy (LPE) growth of MCT: substrate A from vendor A, generally recognised as fabricating the best CZT substrates, and substrate B from vendor B, which was compared to vendor A. One additional substrate from vendor B, substrate B2, was studied as well. The third substrate was (211)B-oriented and used for molecular beam epitaxy (MBE) growth of MCT, substrate C from vendor A. The characterisation consisted of a study by optical microscopy, scanning electron microscopy (SEM), energy-dispersive X-ray spectroscopy (EDS), atomic force microscopy (AFM), near-infrared (IR) transmission microscopy, and Fourier transform infrared spectroscopy (FTIR).

The as-received substrate A had the best surface polish and crystal quality and had almost no particles on the surface. Surprisingly, the preparation etch procedure introduced more particles on the surface. The as-received substrate B had scratches, particles, and voids on the surface, and it had a larger surface roughness than the as-received substrate A by a factor of 10. The roughness decreased after the polishing procedure to about the same value as substrate A. The number of particles also decreased, but it was not as low as on substrate A. While the as-received substrate A had a density of polishing grit less than $2 \cdot 10^4\,\mathrm{cm}^{-2}$, the as-received substrate C had an average density of $4 \cdot 10^7\,\mathrm{cm}^{-2}$. The polishing grit density on substrate C was reduced by a factor of 10 after etch.

The surface of the MCT epilayers that were grown by LPE on substrate A and substrate B2 showed wavy structures on the surface with doughnut-shaped defects and large circular defects with a density of $1 \cdot 10^4\,\mathrm{cm}^{-2}$–$2 \cdot 10^4\,\mathrm{cm}^{-2}$ and $\sim 2\,\mathrm{cm}^{-2}$ respectively. The doughnut-shaped defects seemed to correlate with the polishing grit on substrate B2, but showed no correlation with the polishing grit on substrate A. The MCT epilayer that was grown by MBE on substrate C had a microvoid density of $1 \cdot 10^5\,\mathrm{cm}^{-2}$, which correlated with polishing grit observed before growth.

Sammendrag

I dette studiet ble tre ulike $Cd_{1-y}Zn_yTe$ (CZT) substrater karakterisert for urenheter, partikler og defekter. Substratene ble karakterisert både som motatt fra leverandør og etter forbehandling før groing. Til slutt ble det grodd ett lag med $Hg_{1-x}Cd_xTe$ (MCT) film på hvert av substratene og filmen ble karakterisert. Det er av interesse å få en bedre forståelse av hvordan urenheter, defekter og partikler på overflaten av substratet påvirker kvaliteten på den grodde MCT filmen.

To av substratene var (111)B-orienterte og brukt til å gro MCT ved væskefaseepitaksi (LPE): substrat A fra leverandør A, kjent for å produsere de beste substratene, og substrat B fra leverandør B, som ble sammenlignet med leverandør A. Ett ekstra substrat fra leverandør B, substrat B2, ble også studert. Det tredje substratet, substrat C fra leverandør A, var (211)B-orientert og brukt til å gro MCT ved molekylstråleepitaksi (MBE). Karakteriseringen ble gjennomført ved bruk av optisk mikroskop, sveipeelektronmikroskop (SEM), energidispersiv røntgenspektroskopi (EDS), atomærkraftmikroskopi (AFM), nær-IR transmisjonsmikroskopi og Fouriertransform infrarød spektroskopi (FTIR).

Substrat A hadde den beste overflatepoleringen og krystallkvaliteten som motatt fra leverandør, og hadde omtrent ingen partikler på overflaten. Overraskende nok hadde substrat A mer partikler på overflaten etter etseprosedyren. Substrat B hadde riper, partikler og hulrom på overflaten, og overflateruheten var 10 ganger større enn for substrat A som motatt. Ruheten minket til omtrent det samme som substrat A etter polering og etsing. Antall partikler minket også, men ble ikke like lavt som for substrat A. Substrat C hadde en gjennomsnittlig tetthet at poleringspartikler på $4 \cdot 10^7\,\mathrm{cm}^{-2}$ som motatt fra leverandør i motsetning til substrat A som hadde en poleringspartikkeltetthet mindre enn $2 \cdot 10^4\,\mathrm{cm}^{-2}$ som motatt fra leverandør. Tettheten av poleringspartikler på substrat C ble redusert med en faktor 10 etter etsing.

Overflaten på de LPE-grodde lagene viste en bølgete struktur typisk for LPE med smultringformede defekter og større sirkulære defekter med en tetthet på henholdsvis $1 \cdot 10^4\,\mathrm{cm}^{-2}$–$2 \cdot 10^4\,\mathrm{cm}^{-2}$ og $\sim 2\,\mathrm{cm}^{-2}$. De smultringformede defektene så ut til å korrelere med poleringspartikler på substrat B2, men viste ingen korrelasjon med poleringspartikler på substrat A. MCT filmen som ble grodd på substrat C hadde en tetthet av mikrohulrom på $1 \cdot 10^5\,\mathrm{cm}^{-2}$. Mikrohulrommene korrelerte med partikler observert på overflaten av substratet før groing.

Table of Contents

List of Figures **xi**

List of Tables **xv**

List of Acronyms **xvii**

1 Introduction **1**

1.1 Background 1

1.2 Literature Survey 3

1.3 Problem Formulation 4

1.4 Structure of the Report 4

2 Characterisation Methods **7**

2.1 Optical Microscopy 7

2.2 Near-Infrared Transmission Microscopy 9

2.3 Scanning Electron Microscopy 9

2.4 Energy Dispersive X-ray Spectroscopy 11

2.5 X-ray Photoelectron Spectroscopy 14

2.6 Atomic Force Microscopy 15

2.7 Fourier Transform Infrared Spectroscopy 18

3 Experimental Details **21**

3.1 Epitaxy 21

3.2 CdZnTe Substrates 21

3.3 As-Received 25

3.4 Pre-Growth Surface Preparation 25

3.5 Equipment 27

4 Results and Discussion **31**
4.1 Surface Analysis of As-Received Substrate A 31
4.2 Surface Analysis of As-Received Substrate B 44
4.3 Surface Analysis of As-Received Substrate C 61
4.4 Surface Analysis of Substrate A after Etching 69
4.5 Surface Analysis of Substrate B after fine Polishing and Etching 77
4.6 Surface Analysis of Substrate C after Etching 86
4.7 MCT Film Grown by LPE on Substrate A 93
4.8 MCT Film Grown by LPE on Substrate B2 100
4.9 MCT Film Grown by MBE on Substrate C 104

5 Conclusions **111**

6 Recommendations for Future Work **115**

A Summary and Comparison of the Substrates **117**

References **119**

List of Figures

1.1 Atmospheric transmittance versus wavelength. 2

2.1 Illustration of the various modes of electron or X-ray emission from an incident electron. 12

2.2 Range and spatial resolutions of backscattered electrons, secondary electron, X-rays, and Auger electrons produced from a SEM. 13

2.3 Illustration of the principles behind AFM. 16

2.4 Illustration of the convolution effect in an AFM image due to tip size. . . . 17

2.5 Illustration of the principles behind FTIR. 18

3.1 Crystal structure of CZT. 22

3.2 Optical microscopy images of the substrates. 24

3.3 Graph showing the wavelength range of the near-IR transmission microscopy setup. 28

4.1 Dark field image of substrate A. 32

4.2 SEM images of substrate A. 33

4.3 SEM images, EDS spectra, and EDS atomic compositions of three different types of particles found on as-received substrate A. 34

4.4 SEM image of surface scratches on substrate A. 36

4.5 AFM of as-received substrate A. 37

4.6 X-ray photoelectron spectroscopy (XPS) spectra from substrate A. 39

4.7 EDS spectrum from the centre of the as-received substrate A. 40

4.8 FTIR measurements of the as-received substrate A. 42

4.9 Near-IR microscopy images of Te precipitates in substrate A. 43

4.10 Dark field images of substrate B. 44

4.11 Comparison of dark field microscopy and SEM images. 45

4.12 SEM images of a typical area in the middle of substrate B. 46

4.13 SEM images, EDS spectra, and EDS atomic compositions of one void and six different types of particles found on as-received substrate B. 47
4.14 SEM images of an accumulaton of polishing grit on substrate B. 49
4.15 SEM images of CZT particles on as-revceived substrate B. 50
4.16 SEM image of NaClO particles on substrate B. 51
4.17 SEM images of voids on substrate B. 52
4.18 AFM measurements of voids on as-received substrate B. 53
4.19 Map of the void density on the as-received substrate B. 53
4.20 SEM images of stains on substrate B. 55
4.21 SEM images of scratches on substrate B. 56
4.22 AFM of as-received substrate B. 56
4.23 FTIR measurements of the as-received substrate B2. 58
4.24 SEM image of the semicircle with low IR transmission on substrate B2. . . 59
4.25 Near-IR microscopy images of Te precipitates in substrate B. 60
4.26 Bright and dark field optical microscopy images of as-received substrate C. 61
4.27 SEM images, EDS spectra, and EDS atomic compositions of two different types of particles found on as-received substrate C. 62
4.28 SEM image taken near the centre of the as-received substrate C. 63
4.29 Map of the polishing grit density on the as-received substrate C. 64
4.30 AFM of as-received substrate C. 65
4.31 Comparison of an AFM image with a SEM image taken at the same location on substrate C. 66
4.32 FTIR measurements of the as-received substrate C. 67
4.33 Near-IR microscopy images of Te precipitates in substrate C. 68
4.34 Dark field optical microscopy image of substrate A after a Br:methanol etch. 69
4.35 SEM images of typical areas on substrate A after a Br:methanol etch. . . . 70
4.36 SEM images, EDS spectra, and EDS atomic compositions of three different types of particles and one type of stain found on substrate A after a Br:methanol etch. 72
4.37 SEM image of the corner of the as-received substrate A. 73
4.38 Map of the polishing grit density on substrate A after a Br:methanol etch. 74
4.39 SEM image of large silica agglomeration. 74
4.40 AFM of substrate A after a Br:methanol etch. 75
4.41 Dark field optical microscopy image of substrate B and B2 with surface pre-growth preparation. 77

4.42 SEM images of typical areas on substrate B and B2 with surface pre-growth preparation. . . . 78
4.43 Twin boundaries on substrate B. . . . 79
4.44 SEM images, EDS spectra, and EDS atomic compositions of four different types of particles found on substrate B and substrate B2 after surface pre-growth preparation. . . . 80
4.45 Maps of the polishing grit density on substrates B and B2 after surface pre-growth preparation. . . . 82
4.46 AFM of substrate B and substrate B2 after polishing and etching. . . . 84
4.47 Dark field optical microscopy image of substrate C after Br:methanol etch. 86
4.48 SEM images of typical areas on substrate C with surface pre-growth preparation. . . . 87
4.49 SEM images, EDS spectra, and EDS atomic compositions of two different types of particles found on substrate C after surface pre-growth preparation. 88
4.50 Map of the polishing grit density on substrate C after surface pre-growth preparation. . . . 90
4.51 AFM of substrate C with surface pre-growth preparation. . . . 91
4.52 Nomarski phase contrast microscopy images of MCT film grown by LPE on substrate A. . . . 93
4.53 Bright field optical microscopy images of defects seen on MCT film grown by LPE on substrate A. . . . 93
4.54 Map of the density of doughnut-shaped structures on the MCT film grown on substrate A. . . . 94
4.55 SEM images, EDS spectra, and EDS atomic compositions of five different types of particles and defects found on MCT film grown on substrate A. . 95
4.56 SEM images of doughnut-shaped defects filled with carbon based particles and boron nitride particles. . . . 97
4.57 FTIR measurements of the MCT film grown on substrate A. . . . 98
4.58 Nomarski phase contrast microscopy images of MCT film grown by LPE on substrate B2. . . . 100
4.59 Map of the density of doughnut shaped structures on the MCT film grown on substrate B2. . . . 101
4.60 FTIR measurements of the MCT film grown on substrate B2. . . . 102
4.61 Bright field microscopy images of MCT film grown by MBE on substrate C. 104
4.62 SEM images, EDS spectra, and EDS atomic compositions of one particle and one defect found on MCT film grown on substrate C. . . . 105

4.63 SEM images of microvoids found in MCT film grown by MBE on substrate C. 106
4.64 Map of the density of microvoids on the MCT film grown on substrate C. . 106
4.65 Residue on etched substrate C visible as microvoids in the film. 107
4.66 FTIR measurement from one spot on the MCT film grown on substrate C. 108

List of Tables

4.1 XPS analysis of the as-received substrate A. 38
4.2 EDS impurity analysis of the as-received substrate A. 41
4.3 EDS impurity analysis of the as-received substrate B. 57
4.4 EDS impurity analysis of the as-received substrate C. 67
4.5 EDS impurity analysis of substrate A after a Br:methanol etch. 76
4.6 EDS impurity analysis of substrate B after polishing and a Br:methanol etch. 83
4.7 EDS impurity analysis of substrate C after a Br:methanol etch. 92
4.8 EDS impurity analysis of MCT film grown by LPE on substrate A. 99
4.9 EDS impurity analysis of MCT film grown by LPE on substrate A. 103
4.10 EDS impurity analysis of MCT film grown by MBE on substrate C. 109

A.1 Comparison of the types of particles observed on the four CZT substrates. 117
A.2 Comparison of the density of the different features observed on the four CZT substrates. 118
A.3 Comparison of the RMS roughness of the four CZT substrates. 118
A.4 Comparison of the defects in the MCT films that were grown on the CZT substrates. 118

List of Acronyms

AE Auger Electron

AFM Atomic Force Microscopy

BSE Backscattered Electron

CZT $Cd_{1-y}Zn_yTe$, cadmium zinc telluride

EDS Energy-dispersive X-ray Spectroscopy

FFI Norwegian Defence Research Establishment

FTIR Fourier Transform Infrared Spectroscopy

IR Infrared

IRFPA Infrared Focal Plane Array

LPE Liquid Phase Epitaxy

LWIR Long Wavelength Infrared

MBE Molecular Beam Epitaxy

MCT $Hg_{1-x}Cd_xTe$, mercury cadmium telluride

MWIR Medium Wavelength Infrared

NIRTS Near-infrared Transmission Microscopy

OPD Optical Path Difference

PE Primary Electron

PSPD Position Sensitive Photo Detector

RMS Root Mean Squared

ROIC Readout Integrated Circuit

SE Secondary Electron

SEM Scanning Electron Microscopy

SIMS Secondary Ion Mass Spectroscopy

SPM Scanning Probe Microscopy

SWIR Short Wavelength Infrared

XPS X-ray Photoelectron Spectroscopy

Chapter 1

Introduction

The semiconducting material $Hg_{1-x}Cd_xTe$ (MCT) is used to produce infrared focal plane arrays (IRFPAs) for imaging of objects in the infrared (IR) region. The IRFPA consists of a 2-dimensional array of IR detector elements at the focal plane of a lens. When an IR photon with energy greater than the band gap is absorbed by the detector element, an electron will be excited from the valence band and placed in the conduction band. The charge, which is proportional to the number of absorbed photons, is collected at each detector element and converted to voltage by a readout integrated circuit (ROIC) before the voltage signal is transferred to off-chip electronics. The measured signal from each detector element determine the intensity at the corresponding image pixel. The MCT detector material with the highest sensitivity is grown on lattice matched $Cd_{1-y}Zn_yTe$ (CZT) substrates (Benson et al., 2016).

1.1 Background

What makes the semiconducting material MCT suitable for IR detectors, is the fact that it has high absorption, excellent lattice match with CZT substrates, and a tunable band gap which covers the entire IR region from -0.26 eV to 1.61 eV at 77 K (Hansen et al., 1982). Hence, the material can be adapted to detect IR radiation in any of the IR atmospheric transmission windows. The atmospheric transmission windows refer to the wavelength regions in which there is little absorption in the atmosphere: long wavelength infrared (LWIR) from 8 µm to 13 µm, medium wavelength infrared (MWIR) from 3 µm

to 5 µm, and short wavelength infrared (SWIR) from 1 µm to 3 µm. An example of the atmospheric transmittance through 1 nautical mile, i.e. 1.9 km, following a path at sea level can be seen in Fig. 1.1. IR detection systems are usually designed to operate in these windows, so that radiation emitted from targets of interest can pass through the intermediate atmosphere and reach the detection system.

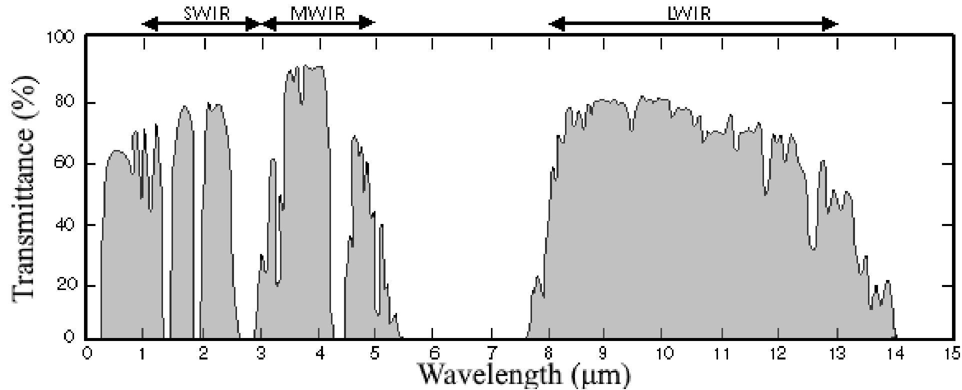

Figure 1.1: Atmospheric transmittance versus wavelength through 1 nautical mile (1.9 km) following a path at sea level. The transmittance is given in percent of total incoming radiation. A transmission window can be seen in the long wavelength infrared (LWIR) for wavelengths between 8 µm and 13 µm and a fragmented transmission window can be seen in the short wavelength infrared (SWIR) and medium wavelength infrared (MWIR) for wavelengths between 0.2 µm and 5 µm. The molecules mainly responsible for absorption are H_2O, CO_2 and O_2. Modified from Naval Air Warfare Center (2013).

The infrared detector applications of MCT and its consequential military role has made it a highly researched material, and it is used to make infrared detectors with high performance. In recent years, the technology has been increasingly utilised in many commercial products, e.g. medical diagnostics, drivers' enhanced vision, security applications and machine vision (Dhar et al., 2013).

1.1.1 The Epitek Laboratory

The Epitek laboratory at the Norwegian defence research establishment (FFI) is a laboratory for research on semiconducting materials. The main research focus is on growth of MCT, which is used in production of infrared detectors. This research consists of developing techniques and technologies for processing and characterising of both materials and components.

CZT is used as a substrate material for both molecular beam epitaxy (MBE) and liquid phase epitaxy (LPE) growth of MCT at the Epitek laboratory. Epitaxy refers to the growth of a crystalline layer with a well-defined orientation determined by the crystal structure of the substrate. Defects, dislocations, impurities, and particles in and on the substrate will affect the growth and quality of the thin film layer. In the worst-case scenario, the processed IR detector element will be defective due to the use of a poor MCT material.

The motivation for this study is the desire to obtain a better understanding of how impurities and defects on the CZT substrate surface affect the quality of the MCT films grown on the substrates. A long and tedious preparation process is required to get satisfying substrate surface quality for epitaxial growth (Triboulet and Siffert, 2009). Since the MCT detector material is grown directly on the CZT substrate, the as-received surface and the following pre-growth preparation of the surface are critical in the production of high quality detector material (Benson et al., 2015). It is important to grow films with high crystallinity, i.e. few grain boundaries and almost no dislocations, and few defects and impurities to ensure that the detector elements that are processed on the film function properly.

1.2 Literature Survey

Defects in MBE-grown MCT have been studied by many groups. Selvig et al. (2007, 2008a,b) at FFI have described these defects as microvoids, hillocks, high temperature voids, needles, and dislocations. Microvoids are formed at all substrate temperatures, but the density increases with lower substrate temperature, and they often originate from a defect or a particle at the substrate surface. High temperature voids appear at higher temperatures, when Hg evaporates from the film and leaves an excess of Te which then collects in high temperature voids along with some polycrystalline CdTe and MCT. The temperature where this occurs is called the tellurium phase limit.

A study of the impact of precipitates and contamination in CZT substrates on growth of MCT has been conducted by Benson et al. (2014, 2015, 2016). They studied state-of-the-art (211)B oriented CZT substrates for growth of MCT by MBE. They associated two categories of MCT defects with defects originating in the substrate surface. The first was high temperature voids and bumps on the surface of MCT that were a result of tellurium

precipitates in the underlying CZT substrate. The second was microvoid defects in the MCT film that originated in pits on the substrate surface. Their study of contamination on the as-received CZT substrates revealed polishing scratches, residual polishing grit, Te precipitates, Te inclusions, CZT particles, and mounting wax. They observed that the residual polishing grit and mounting wax was removed by etching, but that the surface contamination of CZT particles was not removed by a standard MBE preparation etch.

1.3 Problem Formulation

This study was a continuation of the Specialisation Project in Physics where two as-received CZT substrates were characterised with optical microscopy, scanning electron microscopy (SEM), and energy-dispersive X-ray spectroscopy (EDS). In this study, a third substrate was obtained and all three substrates were studied further.

A characterisation of the surface of the substrates, both as-received and after surface pre-growth preparation, was performed. The substrates were first studied with optical microscopy to get an overview of the samples. To obtain higher resolution and more details, SEM with EDS was used to identify the different types of particles and features, as well as the composition of the substrate matrix. Near-IR transmission microscopy was used to observe precipitates and inclusions throughout the bulk of the substrate. Atomic force microscopy (AFM) was used to get high resolution topographic mappings of the substrate surfaces, and Fourier transform infrared spectroscopy (FTIR) was used to measure transmission spectra in a grid of points on the substrate. Finally, an MCT film was grown on each substrate and the same characterisation was carried out to correlate the number of defects and type of defects in the grown MCT layer with the preparation of the substrate.

1.4 Structure of the Report

The ordering of the text is as follows: Chapter 2 describes the characterisation methods that were used in the study. In Chapter 3, the substrates, preparation methods, and experimental setup of the different characterisation methods are presented. Chapter 4 presents the results and each result is discussed subsequently. Chapter 5 presents a

summary and a conclusion. Lastly, recommendations for further work are proposed in Chapter 6. A summary of the results is presented in tables in Appendix A.

Chapter 2

Characterisation Methods

In order to describe the physical and chemical properties of a material, it is important to have methods that can characterise the surface layer.

2.1 Optical Microscopy

The optical microscope uses visible light and optical lenses to magnify images of small features. There are different illumination techniques that can be used to increase the contrast from the sample. One of these techniques is bright field microscopy, where the scattered beam is excluded from the image and the contrast in the image comes from the absorption of light in the sample. A complementary technique is dark field microscopy, in which the unscattered beam is excluded and it is the scattered light that forms the image. A third optical microscopy technique is Nomarski microscopy, which utilises the optical path length of the sample to enhance the contrast and see otherwise invisible features.

Even if all optical aberrations in the lens system are assumed to be negligible, i.e. a perfect lens, there will be a limit to how small details that can be resolved due to interference and diffraction of the light that passes through the system. Resolution is defined as the minimum distance between two points at which they can be distinguished. For two point sources surrounded by Airy discs of diffracted light, this minimum distance is at the distance where the principal maximum of one source coincides with the first minimum of the second source. If the sources have equal wavelength, then the Airy discs have the same radius and this minimum distance is equal to the radius of one Airy disc, measured

from the principal maximum to the first minimum intensity. This is called the Rayleigh criterion (Rayleigh, 1879, 1880). The corresponding angle of resolution θ is given by

$$\theta = 1.22\frac{\lambda}{D}, \tag{2.1}$$

where λ is the wavelength of the light and D is the diameter of the aperture. θ may be converted into spatial resolution d by multiplying Eq. (2.1) with the distance to the object. For a microscope this distance is approximately the focal length f of the objective. Then Eq. (2.1) becomes

$$d = 1.22\frac{\lambda f}{D}. \tag{2.2}$$

The term numerical aperture is used in microscopy to describe the acceptance cone of an objective. Numerical aperture is defined as

$$\mathrm{NA} = n \sin\theta_{\mathrm{cone}},$$

where n is the refractive index and θ_{cone} is the half-angle of the maximum cone of light that can enter or exit the lens. Using geometrical considerations and the small angle approximation, the numerical aperture can be expressed as

$$\mathrm{NA} = n\frac{D/2}{f}. \tag{2.3}$$

Inserting Eq. (2.3) into Eq. (2.2) gives

$$d = 0.61\frac{n\lambda}{\mathrm{NA}}. \tag{2.4}$$

Eq. (2.4) shows that there is a linear relation between resolution and the wavelength of the incoming light. If the wavelength is reduced, it becomes possible to resolve smaller details. For an optical microscope, NA is approximately 1 and the refractive index in air is approximately 1. Then, for visible light, i.e. wavelengths in the range 400 nm to 680 nm, it would be possible to achieve a resolution of 244 nm to 415 nm with an optical microscope. Since the spatial resolution is proportional to λ, blue light can be focused to a smaller spot than red light due to its shorter wavelength.

2.2 Near-Infrared Transmission Microscopy

Materials that are transparent to infrared radiation can be investigated using near-infrared transmission microscopy (NIRTS). This is a technique which images IR radiation that is transmitted through a sample. The contrast in the image is formed from the interaction of the beam through the sample. E.g. precipitates consist of another material with different optical properties than the sample matrix and may not be transparent to IR radiation, and hence, appear as dark spots in the resulting image.

The light bulb used to illuminate the sample can be considered a blackbody. The photon radiance from a perfect blackbody is given by Planck's law of blackbody radiation. The number of photons emitted per unit wavelength λ per second per steradian from one square meter of a perfect blackbody at temperature T is (Liboff, 2003)

$$L_\lambda(T) = \frac{2c}{\lambda^4}\left(\mathrm{e}^{\frac{hc}{kT\lambda}} - 1\right)^{-1}, \tag{2.5}$$

where $h = 6.63 \cdot 10^{-34}\,\mathrm{J\,s}$ is Planck's constant, $c = 3.00 \cdot 10^{8}\,\mathrm{ms^{-1}}$ is the speed of light and $k = 1.38 \cdot 10^{-23}\,\mathrm{JK^{-1}}$ is Boltzmann's constant.

The highest spatial resolution of an IR microscope is defined by the diffraction limit of the radiation, see Eq. (2.4). Over the near-infrared region the wavelengths vary between 750 nm and 1.4 µm. Hence, if a microscope with an ideal numerical aperture of 1 is used in air, where the refractive index is approximately 1, then the maximum spatial resolution will be between 550 nm and 850 nm.

2.3 Scanning Electron Microscopy

Scanning electron microscopy (SEM) is a technique that is used to study materials at greater magnification than with optical microscopy. A point resolution of less than 1 nm can be achieved using the SEM (Goldstein et al., 2012). The SEM utilises electrons and magnetic lenses in the place of photons and optical lenses in optical microscopy. Even though the image is created in a different way than in the optical microscope, the maximum resolution is still limited by the wavelength of the particle used, which in this case is the electron.

The wavelength of an electron is given by the de Broglie relationship (de Broglie, 1924)

$$\lambda = \frac{h}{p}, \tag{2.6}$$

where $h = 6.63 \cdot 10^{-34}\,\mathrm{m^2kgs^{-1}}$ is Planck's constant and p is the momentum of the electron. The momentum of the electron can be calculated using the energy-momentum relation

$$E^2 = (pc)^2 + (m_0c^2)^2, \tag{2.7}$$

where E is the total energy of the electron, c is the speed of light, and m_0 is the electron's rest mass. The total energy is the sum of the rest mass energy m_0c^2 and the kinetic energy E_k. When an electron at rest is accelerated through a potential difference U, its kinetic energy will become equal to the energy of the field $E_\mathrm{k} = eU$, where $e = 1.60 \cdot 10^{-19}\,\mathrm{C}$ is the elementary charge. This gives that the total energy of the electron is

$$E = m_0c^2 + eU. \tag{2.8}$$

An expression for the momentum of the electron is obtained by inserting Eq. (2.8) into Eq. (2.7)

$$pc = \sqrt{(eU)^2 + 2m_0eUc^2}. \tag{2.9}$$

When inserting Eq. 2.9 into Eq. 2.6, the de Broglie wavelength can be calculated from the known variables h, m_0, e, U and c

$$\lambda = \frac{h}{\sqrt{2m_0eU\left[1 + eU/(2m_0c^2)\right]}}. \tag{2.10}$$

For a 1.00 kV accelerating potential, the electron wavelength is $3.88 \cdot 10^{-2}\,\mathrm{nm}$, while for a 25.0 kV accelerating potential, the electron wavelength is $7.66 \cdot 10^{-3}\,\mathrm{nm}$, according to Eq. 2.10. These small wavelengths allow the SEM to achieve high resolution images. The electromagnetic lenses, which are needed to focus the electron beam, limit θ_cone to 10^{-2} rad. Therefore, the diffraction limit, as given by Eq. (2.4), is 2.37 nm and 0.469 nm for accelerating voltages of 1.00 kV and 25.0 kV respectively. This is the theoretical limit, but the real obtainable resolution is lower due to spherical aberration, chromatic aberration, astigmatism, and distortion (Brandon and Kaplan, 2013).

The SEM produces images by raster-scanning a focused beam of electrons across the

sample and plotting the intensity of different signals versus beam position. During the interaction with the sample, the incoming primary electrons (PEs) are the source to emitted secondary electrons (SEs), backscattered electrons (BSEs), Auger electrons (AEs), bremsstrahlung, and characteristic X-rays.

SEs are valence and conduction electrons emitted by atoms excited by the incident electron beam, see Fig. 2.1a. They have low energy (<50 eV) and emerge from very close to the sample surface, i.e. from a small interaction volume, which gives the possibility of high-resolution images. BSEs are incident electrons that scatter from the atomic nuclei and come back out of the sample, see Fig. 2.1b. Larger atoms deflect more electrons, resulting in a larger signal at the detector. BSEs can emerge from deeper into the sample due to their high energy, i.e. from a greater interaction volume, which can result in a poorer resolution than secondary electron images. SE is generally the preferred signal when imaging sample topography in SEM (Sealy et al., 2000). The brightness of the signal increases with the number of detected SEs.

When an electron from an inner shell is emitted and leaves a vacancy, an electron from a higher energy shell can fall down and fill the vacant energy level, resulting in excess energy. This energy can be released in the form of an emitted photon, i.e. an X-ray, see Fig. 2.1c, or it can be transferred to another electron in an outer shell, which is then emitted from the atom and takes the excess energy with it, see Fig. 2.1d. The emitted electron is called an Auger electron.

2.4 Energy Dispersive X-ray Spectroscopy

Energy-dispersive X-ray spectroscopy (EDS) is a technique used for the elemental analysis or chemical characterisation of a sample. Characteristic X-rays are produced during the interaction of the incident electron beam with the sample and can be detected using EDS. A characteristic X-ray is emitted when an incident electron kicks out an electron from an inner shell in an atom, and an electron from a higher-energy shell falls down to the lower-energy shell and releases the excess energy by emitting a photon. These excitations and de-excitations occur between discrete energy levels characteristic of the element. The characteristic X-rays form a spectrum that is unique for the elements involved, just like a fingerprint. Hence, EDS can be used to determine the elemental composition of the material by evaluating the characteristic energy lines.

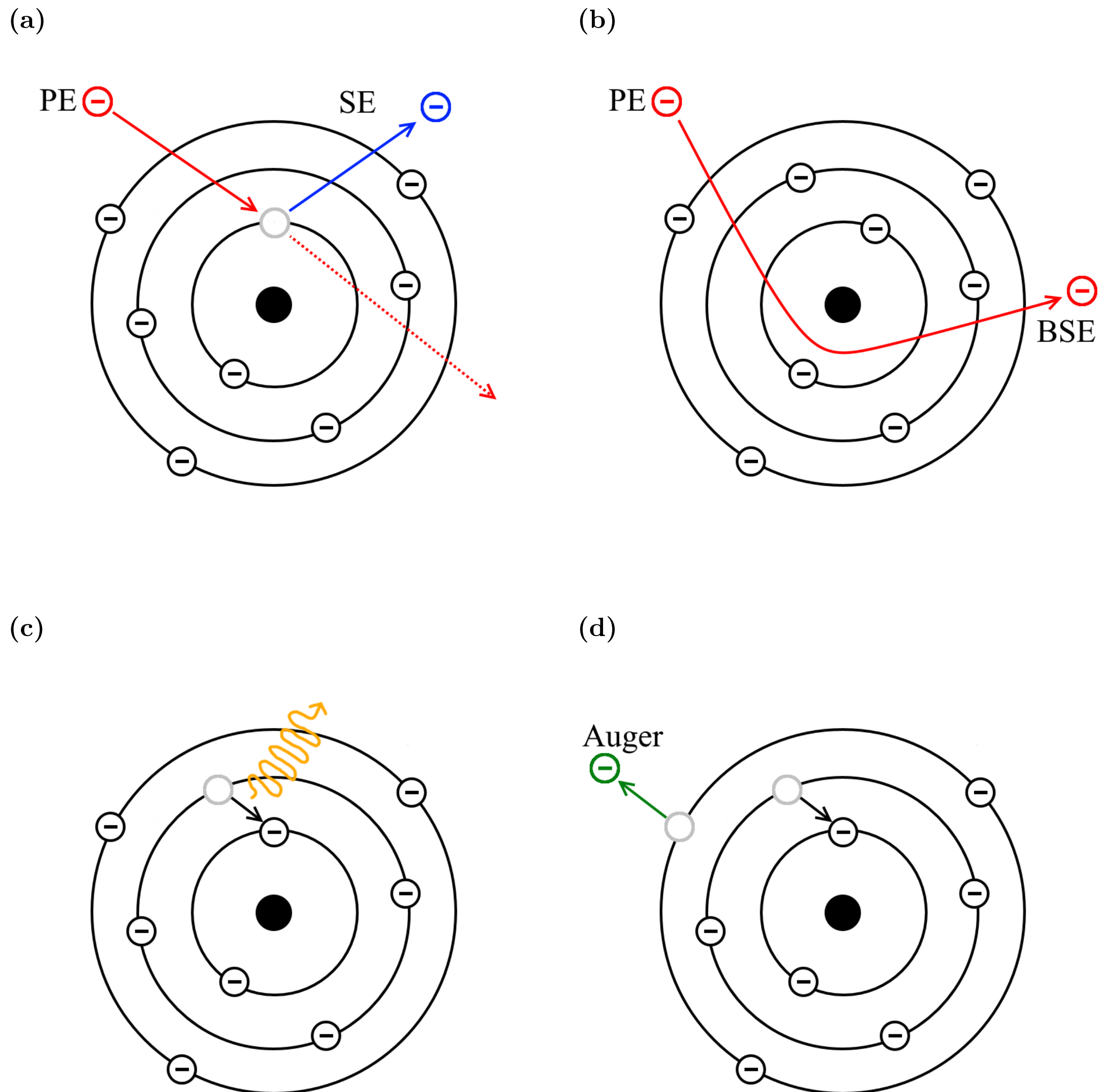

Figure 2.1: Illustration of the various modes of electron or X-ray emission from an incident primary electron (PE): (a) A secondary electron (SE) is emitted when the atom is excited by the incident electron beam; (b) a backscattered electron (BSE) is an incident electron that scatter from the atomic nuclei and come back out of the sample; and (c) and (d) are the emission of an X-ray and an electron, respectively, to release excess energy after an electron from a higher energy shell falls down and fills a vacant energy level. The vacancy is formed by the emission of a secondary electron, see Fig. (a). The filled black circle represents the atomic nucleus, the circle with a minus sign represents an electron, the grey circle represents a vacant energy level, and the curly orange arrow represents the emission of an X-ray (Adapted from Goldstein et al., 2012).

In addition to the characteristic X-rays, bremsstrahlung is produced. This is electromagnetic radiation produced by the deceleration of a charged particle when it is deflected by another charged particle, i.e. when the electron is deflected by the atomic nucleus. The particle looses kinetic energy and the excess energy is transferred away as a photon.

A summary of the interaction volumes of the various modes of electron or X-ray emission from an incident electron can be seen in Fig. 2.2. The interaction volume increases with increasing electron energy, i.e. increasing accelerating voltage, and decreases with increasing average atomic number of the sample (Goldstein et al., 2012). Therefore, it is necessary to work at as low an accelerating voltage as possible taking into account what elements are present and which X-ray lines are needed.

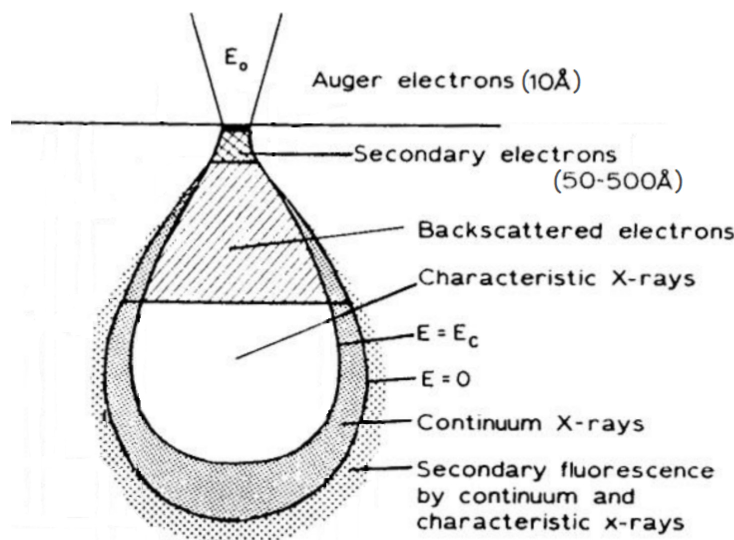

Figure 2.2: Range and spatial resolutions of backscattered electrons, secondary electron, X-rays, and Auger electrons produced from a scanning electron microscope. The outline of the volume of characteristic X-ray production is defined by the case where the electron energy E is just sufficient to produce X-rays requiring the critical energy E_c, which varies with the X-ray of interest. The outline of the volume of continuum X-ray (bremsstrahlung) production is where E is zero and cannot be decelerated any longer (Reprinted from Goldstein et al., 2012).

Absolute concentration values of the elements are obtained using P/B-ZAF analysis. The peak-to-background ratios (P/B) are input to a modified ZAF matrix correction, which relates the recorded spectrum to the primary rate of X-ray generation. This is done mainly based on analytical expressions to correct for atomic number depended X-ray yield (Z), self-absorption (A), and secondary fluorescence enhancement (F) (Bruker, 2008). Since P/B-ZAF do not use explicit or implicit standards in the calculation of concentrations, it is called a true standardless method.

2.5 X-ray Photoelectron Spectroscopy

X-ray photoelectron spectroscopy (XPS) is used to find the elemental composition of the outer surface of a solid (∼100 Å). In addition, XPS can be used to get information about the chemical binding state of the detected elements.

XPS is based on the emission and detection of photoelectrons. The sample is bombarded with a beam of X-ray photons of energy E_{photon}. If E_{photon} is sufficiently large, i.e. greater than the binding energy of an electron E_{binding}, it can kick out the electron from an inner shell in an atom. If the photoelectron is close to the surface, it can be emitted from the sample to the vacuum outside, with a kinetic energy given by

$$E_{\mathrm{kinetic}} = E_{\mathrm{photon}} - E_{\mathrm{binding}} - \phi, \tag{2.11}$$

where ϕ is the work function that accounts for the loss of energy as the electron leaves the sample and is absorbed by the detector. The detector measures the kinetic energy of the emitted photoelectron. Since the electron binding energies are at discrete energy levels, and these are element and chemical-bonding state dependent, a spectrum of the number of emitted electrons as a function of binding energy reveals which elements are present in the sample and their chemical-bonding state.

The mean free path of the photoelectrons in a material is on the order of 20 Å (Tanuma et al., 1991). Hence, only electrons emitted from atoms within a few mean free paths from the surface, i.e. 80 Å, are able to escape the material without loss of energy and be detected as peaks in the spectra. This makes XPS a surface sensitive technique that can tell us about the outermost layer of the sample. The electrons that are scattered inelastically before leaving the sample form the continuous background of the spectrum.

Quantification of the composition in the sample can be made by finding the ratios of the peak areas for the elements found in the sample. The atomic fraction of element A in a homogeneous solid is estimated to be (Moulder et al., 1995)

$$C_{\mathrm{A}} = \frac{I_{\mathrm{A}}/S_{\mathrm{A}}}{\sum_i I_i/S_i}, \tag{2.12}$$

where I_{A} is the measured peak area for element A, and analogously for I_i; and S_{A} is the sensitivity factor of element A, and analogously for S_i. The sensitivity factors take into account parameters that affect the intensity of the element, such as the distinctive

cross-sections and densities of the different elements, and normalise these to that of the most intense peak.

A simple model for an abrupt uniform layer L on a bulk material B is used to estimate the thickness d of a layer. The ratio between the signal from the layer and the signal from the bulk as a function of d is given by (Briggs and Seah, 1990)

$$R(d) = \left(\frac{a_{\mathrm{B}}}{a_{\mathrm{L}}}\right)^3 \frac{\lambda_{\mathrm{LL}}}{\lambda_{\mathrm{BB}}} \frac{1 - \exp\left(-\frac{d}{\lambda_{\mathrm{LL}}\cos\theta}\right)}{\exp\left(-\frac{d}{\lambda_{\mathrm{BL}}\cos\theta}\right)}, \tag{2.13}$$

where a_{B} is the atomic size of material B, and analogously for a_{L}; and λ_{BL} is the inelastic mean free paths of photoelectrons emitted from material B in layer L, and analogously for λ_{BB} and λ_{LL}. The atomic size is derived from $1000\rho_{\mathrm{M}}Na_{\mathrm{M}}^3 = A_{\mathrm{M}}$, where ρ_{M} is the density, N is Avogadro's number, and A_{M} is the mean atomic weight of the matrix atoms. The inelastic mean free path is predicted by the model of Tanuma et al. (1991).

2.6 Atomic Force Microscopy

Atomic force microscopy (AFM) is used to obtain high-resolution topographic images of a sample surface. While SEM provides two-dimensional images without information about depth or height of the defects, AFM can provide three-dimensional topographical images of the defects with the highest vertical resolution among all techniques (Smith, 2013). The AFM is a type of scanning probe microscopy (SPM) that measures the surface topography by raster scanning a cantilever with a sharp tip over the sample surface. As the tip approaches the sample surface, forces between the tip and the surface lead to a deflection of the cantilever according to Hooke's law (Bhushan, 1998)

$$F = -k\Delta x \tag{2.14}$$

where the force F is directly proportional to the cantilever spring constant k and the cantilever deflection Δx. The forces due to electrostatic repulsion dominate when the tip is close to the surface and cause the cantilever to deflect away from the surface, while the attractive van der Waals forces between the surface and the tip dominate when the tip is further away and cause the cantilever to deflect towards the surface.

Cantilever deflections towards or away from the surface are monitored with laser light

from a solid-state diode that is focused on the back of the cantilever and reflected onto a position sensitive photo detector (PSPD), as seen in Fig. 2.3. As the tip scans the sample, the raised and lowered features on the sample surface cause the cantilever to deflect, which in turn change the direction of the reflected laser beam that is detected by the PSPD. The resulting image is a topographic map of the sample surface features. The lateral resolution of the images is around 30 nm while the vertical resolution can be up to 0.1 nm (Birdi, 2003).

There are three basic AFM imaging modes: contact mode, non-contact mode, and tapping mode. Contact mode is, as the name implies, a technique where the tip is in contact with the surface during the scan. In the case of non-contact mode the tip is vibrating, with a constant frequency near the resonant frequency of the tip, above the surface. In tapping mode the tip is closer to the surface and vibrates with a higher amplitude than in non-contact mode. In the lowest point of the trajectory, the tip is briefly touching the surface.

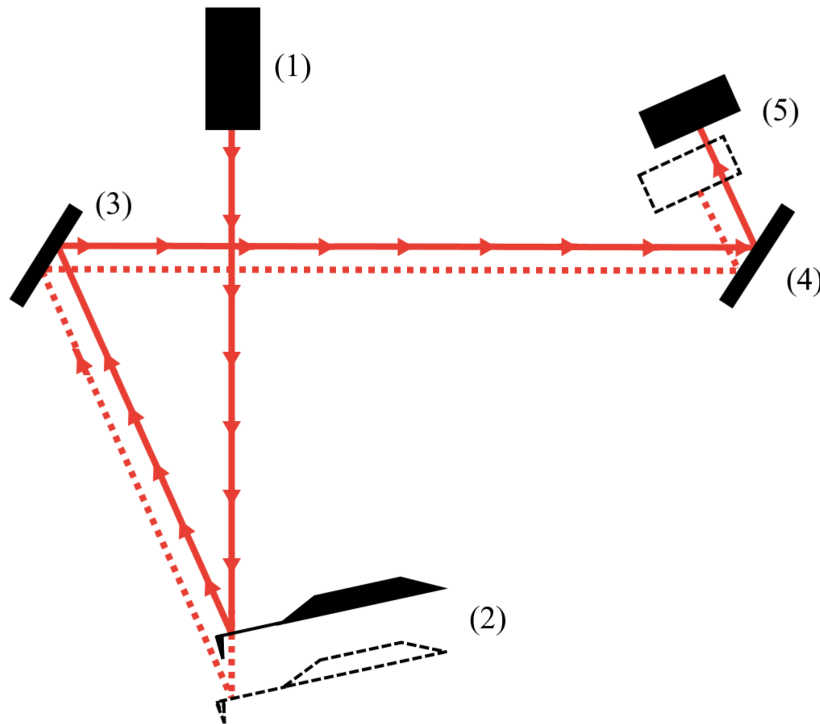

Figure 2.3: Illustration of the principles behind AFM. The setup consists of: (1) laser, (2) cantilever with a sharp tip, (3) steering mirror, (4) stationary mirror, and (5) position sensitive photo detector (PSPD). The red line represents the laser beam and the dotted red line show how the path is changed by the deflection of the cantilever (Adapted from PSIA, 2002).

An AFM image is a convolution between the tip and the sample which is to be visualised. Therefore, the tip radius limits the lateral resolution, and cause an image artefact which

is observable when using a tip with a similar or higher radius of curvature with respect to the feature. Holes can appear both narrower and less deep, and protruding features can appear wider than they really are, see Fig. 2.4. For the technique to provide information of the surface at the atomic level, the tip must be sharp, ideally terminating in just a single atom on the tip. Any changes to the tip that cause it to become broader, will decrease the lateral resolution of the image. These changes might be caused by contaminants on the tip or wearing of the tip due to collisions with the sample by either scanning too fast or having a rough surface (Birdi, 2003).

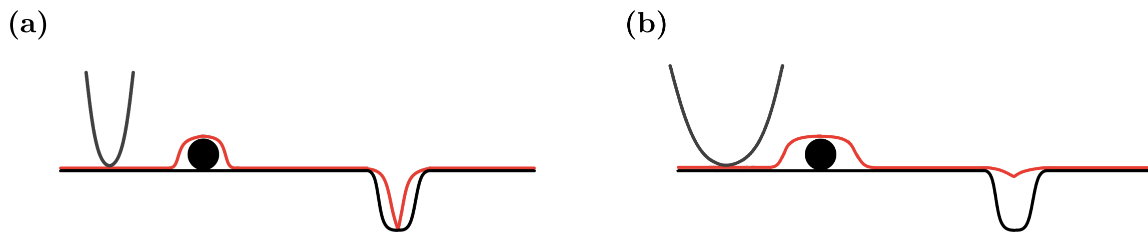

Figure 2.4: Illustration of an AFM image artefact that is caused by the convolution effect between the tip and the feature which is to be visualised, i.e. a broadening effect. This image artefact is observable when using a tip with (a) a similar or (b) higher radius of curvature with respect to the feature being imaged. In the images, grey represents the probe tip, black represents the real surface and surface features, and red represents the displayed surface (Adapted from PSIA, 2002).

2.6.1 Surface Roughness

Surface roughness is used as a quantitative measurement of surface changes. Surface roughness refers to height variations on the surface in the direction of the normal vector of a reference plane. There are many ways to characterise roughness, but one of the most commonly used for describing AFM images is the root mean squared (RMS) roughness (Eaton and West, 2010). RMS roughness is a statistical parameter given by (Thomas, 1999)

$$R_{\mathrm{q}} = \sqrt{\frac{1}{N}\sum_{i=1}^{N}[z_i - \bar{z}]^2}, \tag{2.15}$$

where N is the number of data points in the image, z_i is the height at point i, and $\bar{z}$ is the average elevation of the image profile.

2.7 Fourier Transform Infrared Spectroscopy

Fourier transform infrared spectroscopy (FTIR) is a technique that is used to obtain an IR transmission spectrum of a material. The spectrum indicates how much light that is transmitted through the sample at each wavelength. Patterns in the spectrum can help identify impurities and contaminants in the sample since molecules exhibit specific IR transmission fingerprints (Smith, 2011).

The transmittance spectrum, the percentage of incoming light that is transmitted through the sample as a function of wavenumber, is found by calculating the ratio of the sample spectrum and the background spectrum. The background spectrum is usually acquired immediately before the sample is placed in the sample compartment to get as identical conditions as possible.

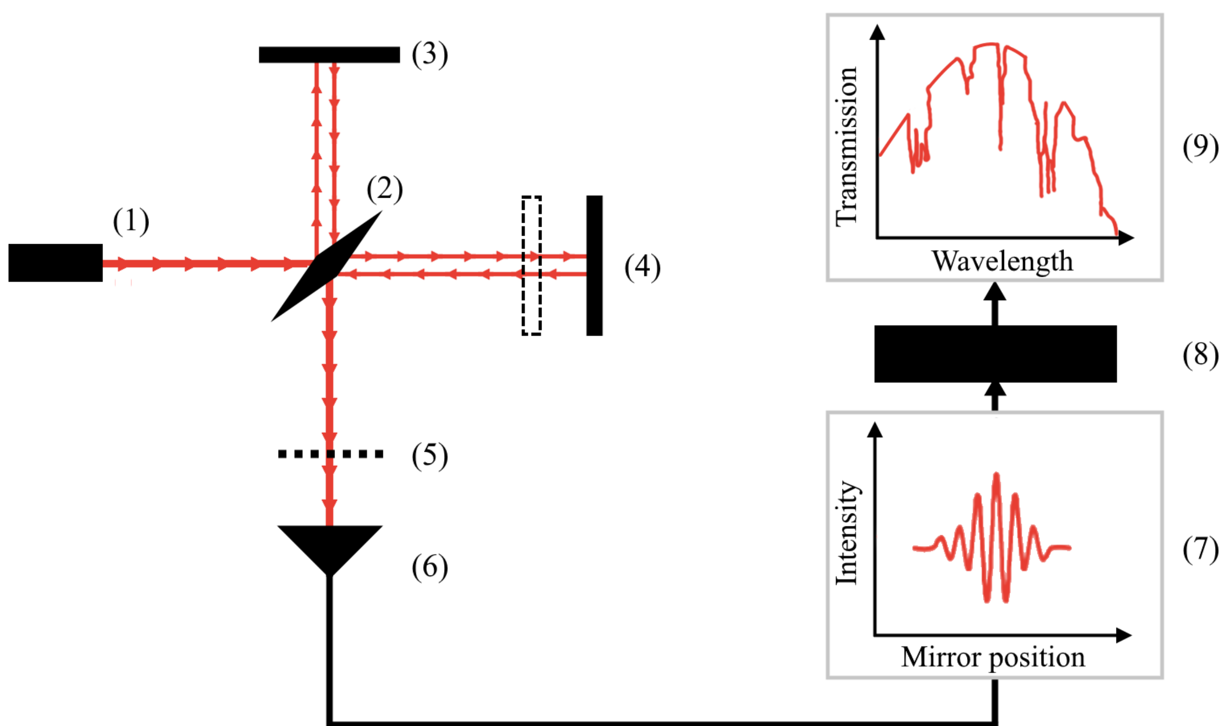

Figure 2.5: Illustration of the principles behind FTIR. The setup consists of: (1) light source, (2) beamsplitter, (3) fixed mirror, (4) movable mirror, (5) sample compartment, (6) detector, (7) interferogram, (8) Fourier transform, and (9) IR transmission spectrum (Adapted from Nicolet, 2001).

A beam of photons – containing a range of wavelengths – is first shone into a Michelson interferometer before it hits the sample. The Michelson interferometer contains a beamsplitter, which splits the light source into two. One beam is refracted towards a fixed

mirror and the other is transmitted towards a movable mirror. The beams are reflected back towards the beamsplitter where they recombine, see Fig. 2.5. The difference in optical path length between the two beam paths, known as the optical path difference (OPD), is adjusted by moving the movable mirror. The resulting interference pattern is directed to the sample, and the detector measures how much of the beam that is transmitted through the sample as a function of mirror position, known as an interferogram.

As the mirror moves continuously from an OPD of zero to a distance further away, the intensity pattern of one specific wavelength λ goes from constructive interference at OPD$=0$ to destructive interference where OPD$=(n+\frac{1}{2})\lambda$ and constructive interference where OPD$=n\lambda$ for $n \in \mathbb{N}$. Waves which are not completely in or out of phase will have an intermediate intensity pattern. The interferogram is the sum of the interference patterns from all the different wavelengths measured at many discrete mirror positions. A Fourier transform is used to find how much each wavelength contributes to the signal, and converts the interferogram to a spectrum that shows the intensity of the beam that is transmitted as a function of wavelength (Smith, 2011).

The band gap of a material can be determined from the FTIR spectrum as the wavelength where the transmission increases steeply with increasing wavelength. The increase in transmission occurs because the photons with energy greater than the band gap can be absorbed by the creation of an electron-hole pair, while photons with energy less than the band gap cannot and are transmitted.

The thickness of a thin layer on top of another material can be calculated from the FTIR spectrum. Both the surface of the layer and the interface between the layer and the underlying material reflect the incoming beam of photons. This difference in optical path length causes constructive and destructive interference of the light, which manifests as a fringing effect in the FTIR spectrum. The maxima are found where the optical path difference equals an even number of wavelengths. Hence, the fringes in the spectrum can be used to determine the thickness of the film

$$d = \frac{1}{2}\frac{1}{n\Delta k}, \tag{2.16}$$

where n is the refractive index and Δk is the average period for one fringe (Griffiths and De Haseth, 2007; Stuart et al., 2008).

Chapter 3

Experimental Details

In this chapter, a description of the substrates, the pre-growth surface preparation methods, and the experimental equipment is presented.

3.1 Epitaxy

Epitaxy refers to the growth of a crystalline layer with a well-defined orientation determined by the crystal structure of a substrate. One of the epitaxial growth techniques is liquid phase epitaxy (LPE) where a layer is grown from a supersaturated liquid solution on a substrate. The process starts with heating the solution, followed by a period where impurities are baked out. After this, the temperature is lowered to equilibrium, and then the growth is achieved by reducing the temperature so that the material deposit on the substrate. Another epitaxial growth technique is molecular beam epitaxy (MBE) where a source material is heated to produce an evaporated beam of particles. Then the constituent elements of the wanted material are transported through vacuum from the sources to the substrate where it condenses.

3.2 CdZnTe Substrates

$Cd_{1-y}Zn_yTe$ substrates with $y = 0.04$ are mainly CdTe with a small fraction of the Cd atoms replaced by Zn atoms in order to match the substrate lattice constant to that of

$Hg_{1-x}Cd_xTe$ (6.46-6.48 Å). CZT has a zincblende structure with two interpenetrating face-centered cubic lattices offset by $\left(\frac{1}{4}, \frac{1}{4}, \frac{1}{4}\right) a$, where a is the lattice constant in the primitive cell. Cadmium or zinc atoms form one of the sublattices while tellurium atoms form the other, as seen in Fig. 3.1a.

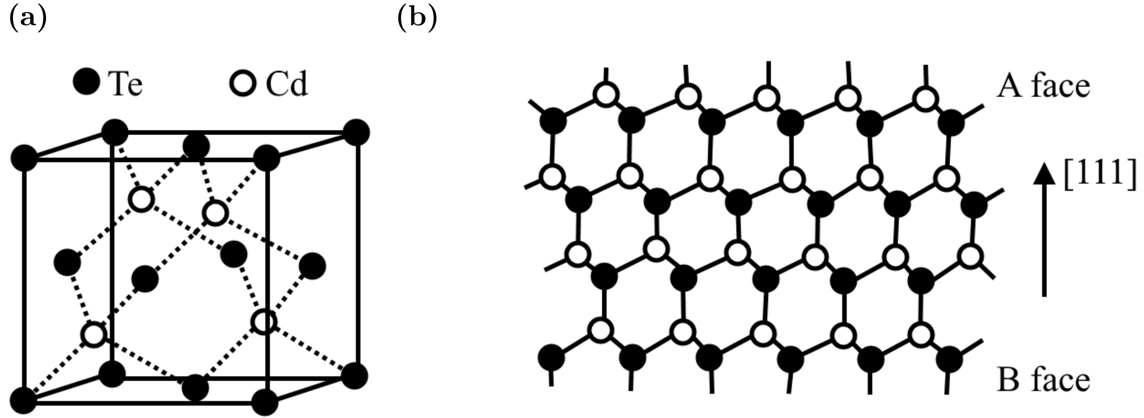

Figure 3.1: Illustration of (a) the zincblende crystal structure of CZT and (b) the difference between the two faces of a (111)-oriented CZT substrate (or the (111)-oriented steps in a (211)-oriented substrate). The plane will have top and bottom surfaces that are slightly different: the A face is terminated by triply bonded Cd (or Zn) or singly bonded Te, while the B face is terminated by triply bonded Te or singly bonded Cd (or Zn). Cd (or Zn) atoms form the white sublattice and Te atoms form the black sublattice (Adapted from Sivananthan et al., 1986).

The orientation of the substrate is given by the surface crystallographic plane, and for CZT substrates the crystal is cut to give surface plane (111) for LPE growth and (211) for MBE growth. The (211)-oriented substrate consists of steps that are (111)-oriented. A substrate cut along these planes will have top and bottom surfaces that are slightly different: one surface will be terminated by triply bonded Cd (or Zn) or singly bonded Te, and is called the *A* face, while the other side of the substrate will be terminated by triply bonded Te or singly bonded Cd (or Zn), and is called the *B* face (Sivananthan et al., 1986), see Fig. 3.1b. MCT films are always grown on the B face of the substrate since it is less sensitive to misorientation (Parker et al., 1988; Edwall et al., 1984).

In this study, two (111)B-oriented substrates from different manufacturers and one (211)B-oriented substrate have been studied. Substrate A is a 30 mm × 30 mm state-of-the-art (111)B-oriented CZT substrate from the Japanese firm JX Nippon Mining & Metals Corporation (vendor A). The y-value in substrate A is 2.8 %–3.6 %. Substrate A was compared to substrate B – a 30 mm × 30 mm (111)B-oriented CZT substrate – from an alternative source (vendor B). Substrate B has ∼4 % Zn and ∼96 % Cd. Substrate C is

a $15 \times 15\,\text{mm}^2$ state-of-the-art (211)B-oriented CZT substrate also from vendor A. The y-value in substrate C is 2.6 %–3.4 %.

Images of the substrates can be seen in Fig. 3.2. Relative terms, such as *upper*, *lower*, *left*, *right*, and *centre*, are used to describe the locations on the substrate surfaces throughout the thesis. These relative terms are related to the orientation depicted in Fig. 3.2. When coordinates are given, they are measured from the lower left corner of the substrate surfaces.

The substrates were characterised as-received and after surface pre-growth preparation. The latter was either polishing and etching or just etching if the substrate was already polished by the vendor. Then an MCT layer was grown on each substrate and characterised with emphasis on the correlation between defects in the MCT layer and particles, impurities, defects and roughness of the substrates.

Unfortunately, after being characterised both as-received and after polish and etch, substrate B broke in two pieces when mounting for the final FTIR mapping before MCT growth. One piece shattered further when it fell on the floor, as seen in Fig. 3.2e. These substrates are brittle, and all the handling of the substrate through two rounds of characterisation with various techniques had made it even more so. A new 30 mm × 30 mm (111)B-oriented CZT substrate from vendor B, substrate B2, was polished and characterised before growing an MCT layer on it.

Vendor A sells both (111)B-oriented substrates for LPE growth and (211)B-oriented substrates for MBE growth. The (211)B substrates are cut at an angle of 19° with the (111) planes. This gives a surface with (111)-oriented atomic steps, and the resulting step-flow growth improves the crystallinity of the MBE film because atoms land on the surface and diffuse to a step edge before they nucleate, and hence, reduce the change of dislocations.

High-quality substrate surfaces are crucial for growth of high-quality films. After cutting, the substrates must be polished to obtain the necessary smooth and planar surface. Finally, an etch is needed to remove polishing products that have been trapped in the substrate during polishing. In LPE growth, the outermost layers of the substrate are initially melting in the liquid growth material before the temperature falls and the film starts to grow on the surface. Therefore, some surface defects can be less important while others remain and affect the grown film.

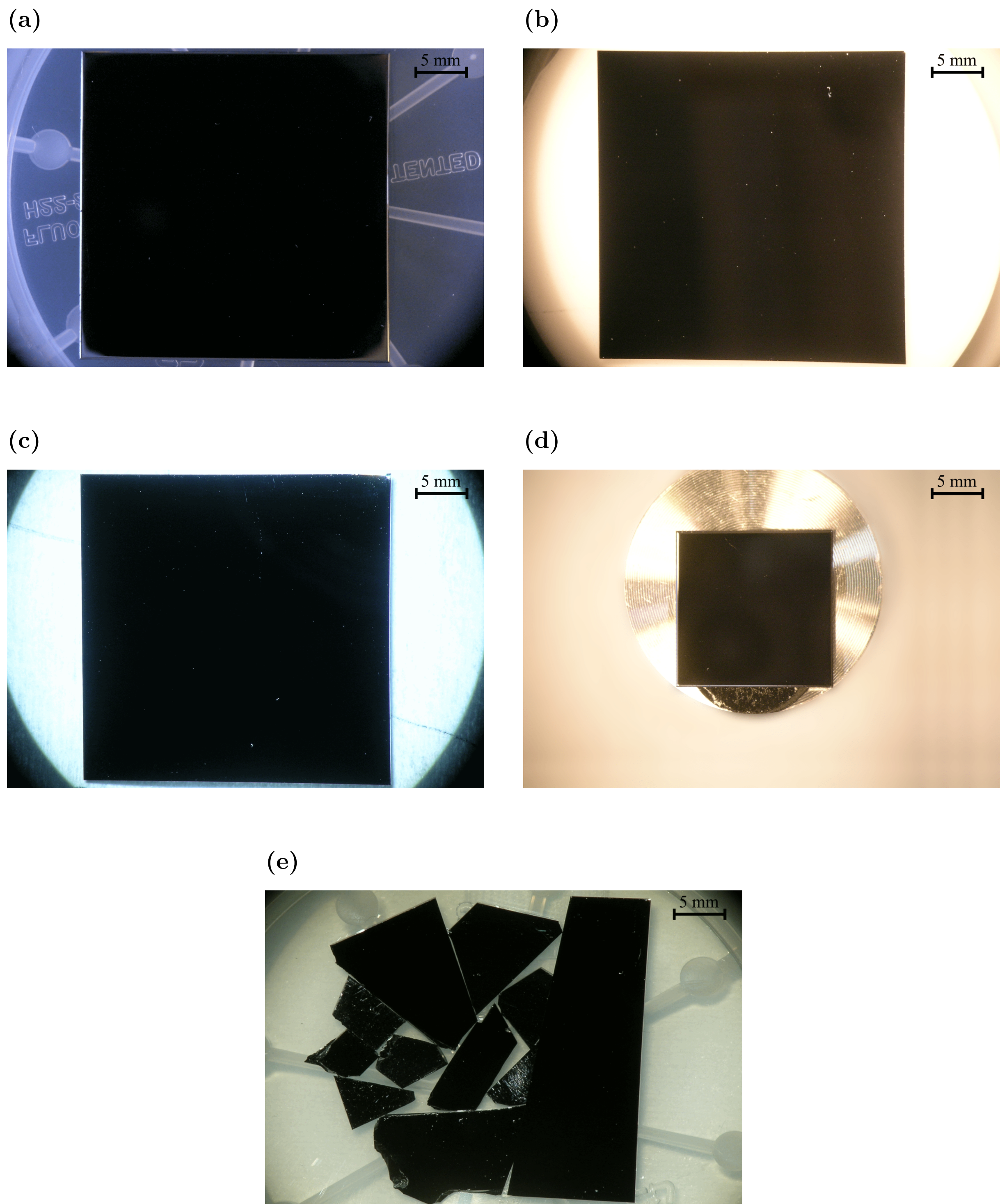

Figure 3.2: Optical microscopy images of the substrates. (a) Substrate A – as-received, 30 mm × 30 mm, (111)B-oriented from vendor A; (b) substrate B – after polish and etch, 30 mm × 30 mm, (111)B-oriented from vendor B; (c) substrate B2 – after polish and etch, 30 mm × 30 mm, (111)B-oriented from vendor B; (d) Substrate C – as-received, 15 mm × 15 mm, (211)B-oriented from vendor A; and (e) substrate B after it shattered during mounting for FTIR.

3.3 As-Received

The substrates were removed from the box they came in and directly mounted on carbon tape on a SEM holder before SEM was performed. To ensure that the removal process would be as easy as possible, the carbon tape was made almost non-sticky by touching the tape multiple times with a cleanroom glove. A magnetic plate was attached underneath the SEM holder with double-sided tape when AFM was performed.

To remove the substrate from the SEM holder, the holder with the substrate on top was placed in a beaker, and acetone was poured into the beaker up to right below the backside of the substrate. The acetone dissolved the carbon tape so that it was possible to get a scalpel under the substrate and push the substrate off.

3.4 Pre-Growth Surface Preparation

It is important to have the surface as smooth and planar as possible and without any particles to grow high-quality MCT film. Hence, substrate preparation is an important part before the deposition of a crystalline layer takes place. The three substrates were prepared in the following way: Substrate A and C needed only an etch before growth since they were already sufficiently polished by the vendor. Substrate B and B2 needed a final polish as part of their pre-growth preparation in addition to an etch since they only had been through a coarse polish by the vendor. The surface preparation procedures will be described in more detail in the following paragraphs.

3.4.1 Etching of Substrate A

After the characterisation of the as-received substrate A was completed, the substrate went through a standard LPE Br:methanol preparation etch procedure. First, the substrate was cleaned using a two-solvent method. The two-solvent cleaning procedure consists of placing the substrate for 2 min–3 min in each of four containers: two with boiling acetone, one with boiling methanol, and one with methanol at room temperature. Before further preparation, the substrate was blown dry with gaseous nitrogen. Then, the substrate was etched in an etch consisting of 0.25 ml bromine and 40 ml methanol for 30 s while stirring every 1 s–2 s. Finally, the substrate was rinsed with methanol to remove any etch residues.

This Br:methanol etch procedure was repeated before LPE growth with an etch time of 50 s to remove possible contaminants from the characterisation of the etched substrate.

3.4.2 Polishing and Etching of Substrate B

After the characterisation of the as-received substrates B and B2 was completed, the substrates were cleaned using soap, rinsed with purified water, and then blown dry with gaseous nitrogen. This is the standard LPE preparation procedure before polishing and etching take place, but due to the exposure during characterisation and the potential residue of carbon tape underneath substrate B, it had to go through an additional cleaning procedure with a two-solvent method, as explained in Section 3.4.1.

The as-received substrates B and B2 were polished with alumina powders with an abrasive size of 50 nm using a Struers LaboPol-5 polishing jig. First, the substrate was planarised by removing an average of 80 µm of material from the surface of the substrate with a hard polishing pad for 200 min. Then a smoother finish was achieved by removing another 30 µm of material from the surface using a soft polishing pad for 111 min. The soft polishing pad conforms to local topology variations on the nanoscopic scale, and thus, makes the surface smooth, while hard pads do not (Lee et al., 2000). The polishing slurry consisted of 50 nm colloidal alumina particles and soap dissolved in methanol. The use of soap as a lubricant is helpful in prolonging the life of the polishing jig.

During polishing the substrate was attached to a plate using Crystalbond mounting compound. The Crystalbond was melted underneath the substrate to form an adhesive bond between the substrate and the mounting plate when solidifying. After the polishing process was completed, the mounting plate was heated to melt the Crystalbond so that the substrate could be pushed off. Then the remaining Crystalbond was dissolved and removed through the same two-solvent cleaning procedure as before polishing. The cleaned substrate was soaked in a beaker with methanol at room temperature overnight before it was etched with a Br:methanol etch the following day, as described for substrate A in Section 3.4.1, and quickly inserted into the SEM.

3.4.3 Etching of Substrate C

After the characterisation of the as-received substrate C was completed, the substrate went through a standard MBE Br:methanol preparation etch procedure. First, the substrate was cleaned with methanol and acetone: A thin layer of methanol was left on the surface for 2 s–3 s before it was blown dry with gaseous nitrogen, and the equivalent was repeated with acetone and finally with methanol for the second time. Then, the substrate was etched in 1 % Br:methanol for 2 min while gently stirring every 30 s. Finally, the substrate was rinsed by soaking the substrate in multiple beakers filled with methanol.

3.5 Equipment

A Leica DM RXA2 optical microscope was used to capture dark field optical microscopy images. These images were used to locate irregularities in the substrate surface, known as morphological defects, characterise the surface topography, and count the density of large particles and defects (>0.5 µm).

Transmission IR microscopy was performed using the Leica DM RXA2 optical microscope with transmitted illumination from a halogen light lamp at 3450 K under the stage and a BU238M IR camera from Toshiba Teli for image recording. The band gap in CZT is 1.6 eV. Hence, photons with energy greater than the band gap, i.e. wavelengths smaller than 775 nm, are not transmitted through the substrate. The IR camera can detect photons with wavelengths between 200 nm and 1125 nm. This results in the detection of photons with wavelengths between 775 nm and 1125 nm, as seen in Fig. 3.3. The IR transmission images were used to study tellurium precipitates inside the substrate.

A Hitachi Model SU6600 Variable pressure Schottky field emission gun scanning electron microscope was used to find defects, damage, and particles on the substrate surfaces. The SEM is capable of much higher magnifications and has a greater resolving power than the optical microscope. Hence, it can see much smaller features in finer detail. The SEM is equipped with a Bruker XFlash 5010 detector for the energy-dispersive X-ray spectrometer. EDS was used to identify the composition of defects, damage, and particles on the substrate surfaces. A quantitative determination of the chemical composition of different areas and features was obtained using the Bruker Quantax Microanalysis System software.

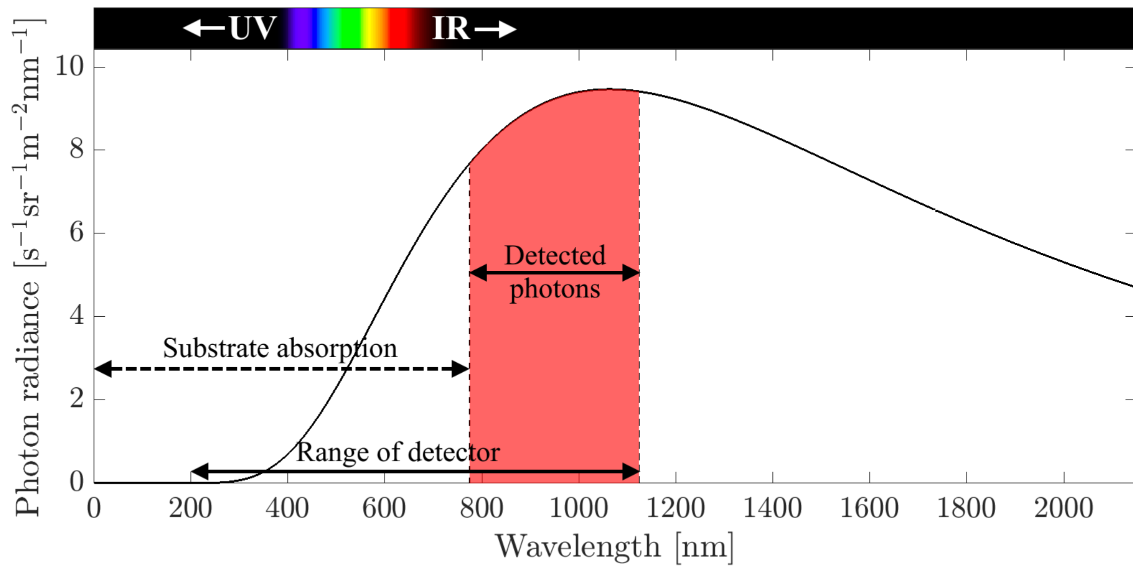

Figure 3.3: The wavelength range of the near-IR transmission microscopy setup used in this study. The black curve is the number of photons emitted per unit wavelength per second per steradian from one square meter of a perfect black-body at a temperature of 3450 K given by Planck's law of black-body radiation, see Eq. (2.5). The red area represents the photons that are transmitted through the sample and detected by the IR camera, i.e. have an energy smaller than the bandgap of CZT (>775 nm), and has an energy within the detector range of the IR-camera (200 nm–1125 nm). The coloured bar above the graph illustrates at which wavelengths ultraviolet (UV), visible, and infrared (IR) radiation are found.

XPS measurements were carried out with a SPECS system equipped with an Al/Mg twin anode XR50 X-ray source and a Riber MAC2 analyser. The Mg anode was operated at 300 W and the X-ray beam was incident at 45° with the sample normal, while emitted photoelectrons were collected in the analyser at 30°. The data was retrieved from the Riber MAC2 control unit by Cameca's Kernel 3 software, and surface composition was determined with standard methods described by Moulder et al. (1995) using intensity peak areas, obtained using Systat Software's PeakFit program, and elemental sensitivity factors measured experimentally on the XPS equipment at FFI by Hirsch et al. (1999).

Topographic mapping of the surfaces was performed with a Park Systems XE-100 atomic force microscope. The AFM images were recorded in non-contact mode using a Nanosensors PPP-NCHR probe with an aluminium coating on the detector side. The images were obtained using a scan rate of 0.2 Hz and a scan size of 5 µm. The AFM is capable of much higher depth and height resolution than the other techniques, and hence, it can be used to obtain greater detail of surface irregularities like scratches and voids.

A Perkin Elmer Spectrum GX FTIR system was used to obtain transmission spectra of the substrates. The spectra present the IR transmittance of the substrates in the wavenumber range of $370\,\mathrm{cm^{-1}}$–$5000\,\mathrm{cm^{-1}}$. They were used to get information about the density and size of tellurium precipitates, the free carrier concentration, and the resistivity of the substrates.

Chapter 4

Results and Discussion

In this chapter, experimental results are presented, analysed, and discussed. In total, one (111)B substrate from vendor A (substrate A), two (111)B substrates from vendor B (substrate B and substrate B2), and one (211)B substrate from vendor A (substrate C) were investigated using bright and dark field microscopy, SEM, EDS, AFM, near-IR transmission microscopy, and FTIR. The substrates were investigated both as-received and after surface pre-growth preparation, except substrate B2, which was not investigated as-received. As the final step, an MCT film was grown on each substrate, except the shattered substrate B, and the same characterisation as for the substrates was conducted to correlate the number of defects and the type of defects in the grown MCT layer with the preparation of the substrate. The results are summarised in tables in Appendix A.

4.1 Surface Analysis of As-Received Substrate A

In previous work (Lauten, 2017), the state-of-the-art as-received (111)B-oriented substrate A was characterised for polishing damage, defects, and residual particles using optical microscopy, SEM with EDS, and XPS. The results are reiterated in this section to better present the full scope of the study. In addition to the previously used methods, AFM, near-IR transmission microscopy, and FTIR were used to study the as-received substrate.

Dark field images from the surface of substrate A, see Fig. 4.1, show that the highly polished (111)B-oriented surface had very few particles or morphological defects that scattered the incoming light. This indicates that the surface is smooth and with few

defects. The particle and morphological defect density was estimated to be $4 \cdot 10^2\,\mathrm{cm}^{-2}$ at the centre and $1 \cdot 10^3\,\mathrm{cm}^{-2}$ at the edges and corners of the surface of substrate A. The density of particles and morphological defects is a measurement which here refers to the sum of all light-scattering objects with sizes $>0.5\,\mu\mathrm{m}$ since any features $<0.5\,\mu\mathrm{m}$ were invisible in the dark field images. Therefore, the true morphological defect density was higher than the one estimated from these images.

Figure 4.1: Dark field image of substrate A captured through the optical microscope Leica DM RXA2 at the centre of the substrate surface.

The substrates from vendor A were considered to be state-of-the-art CZT substrates. They were fine-polished by the vendor, and consequently, they had few surface features. This made it challenging to focus the SEM and find particles on the surface. At a magnification of 100×, no particles or defects could be seen, see Fig. 4.2a. As a result of a higher occurrence of particles towards the edges of the substrate, it was easier to find focus near the edges. An area from the left edge of the substrate with 12 bright spots and three dark vertical lines were observed in Fig. 4.2b. The dark, vertical lines were carbon

contamination from the SEM and were not studied further. The bright spots corresponded to an irregularity or particle on the surface. These features will be described in the following by, among other methods, high-resolution SEM images and EDS spectra.

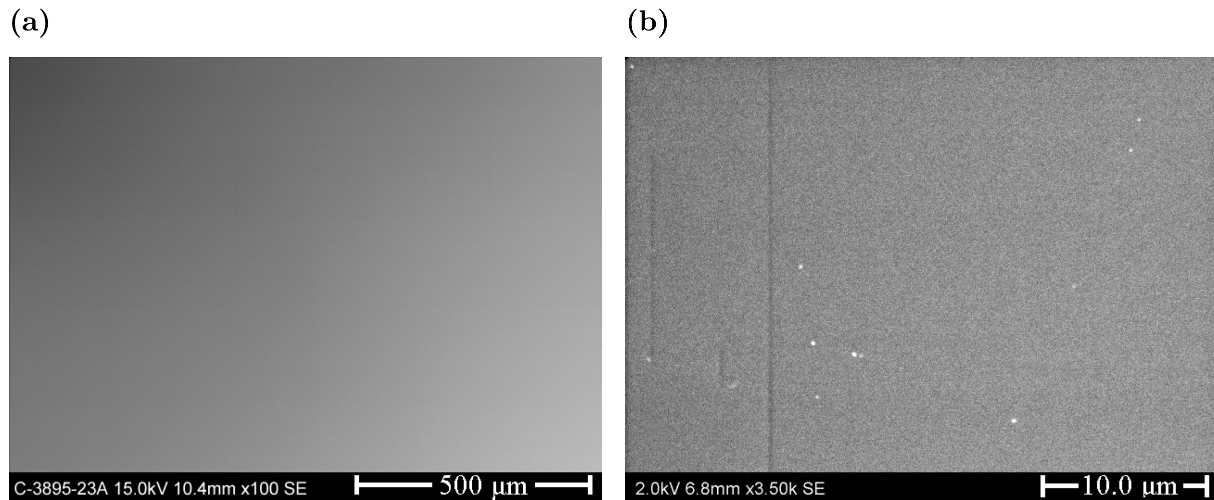

Figure 4.2: SEM images of the surface of substrate A taken near the left edge at (a) low (100×) and (b) high magnification (3500×).

4.1.1 Particles

There were so few particles on substrate A that it was difficult to determine a density of particles on this substrate. The surface was so uniform that it was difficult to keep in focus even at high magnification. However, three different types of particles were found and identified close to the edges of substrate A, as seen in Fig. 4.3.

Alumina (Al_2O_3) Polishing Grit

Small, round particles of size 50 nm were observed near the edges of substrate A, see Fig. 4.3a. The SEM image shows an agglomeration of particles and one single particle with a diameter of 50 nm. The large piece was an agglomeration of the smaller ones. The corresponding EDS spectrum of the large piece revealed that the particles consisted of Al_2O_3. The particles were most likely residual alumina polishing grit which are commonly used in polishing slurries (Benson et al., 2015).

The slurry polishes and flattens the substrate through mechanical action. The alumina

(a)

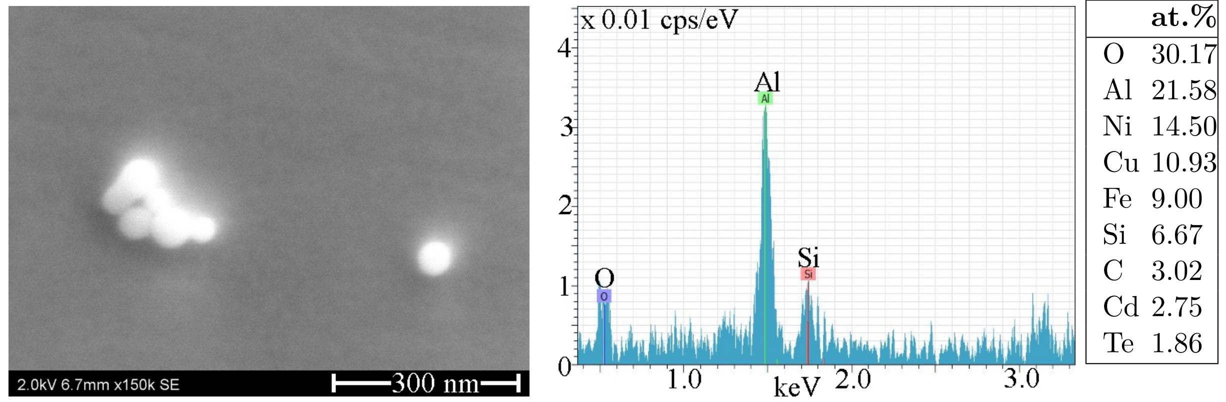

(b)

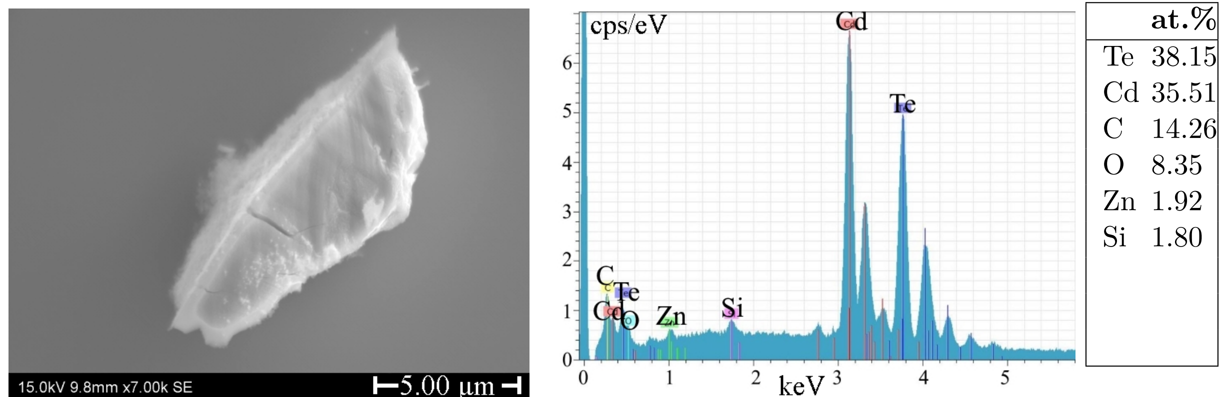

(c)

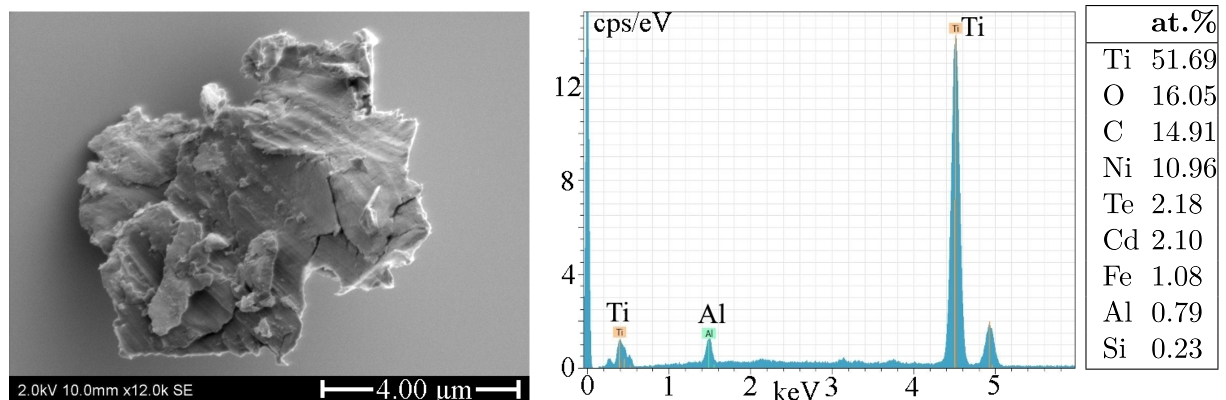

Figure 4.3: High resolution SEM images of three different types of particles found on the as-received substrate A and the corresponding EDS spectra and atomic compositions: (a) Alumina (Al_2O_3) polishing grit; (b) cadmium zinc telluride ($Cd_{0.96}Zn_{0.04}Te$) particle; and (c) titanium (T) particle.

particles in the slurry are suspended throughout the bulk of the medium because of the negative charges that are incorporated on the alumina particle surface and make the particles repel each other. The polishing grit appeared to be electrostatically bound to the top surface layer of the substrate.

It was easier to find polishing grit particles in close proximity to the edges of the substrate rather than in the middle. The density of the particles was therefore higher towards the edges than in the centre. Even though it was difficult to focus in the centre, the small particles would have been possible to focus on if any had been there.

The upper limit on the polishing grit density close to the edges of the substrate was estimated to be $2 \cdot 10^5\,\mathrm{cm}^2$. It was not possible to get any sharp SEM images to count the density of polishing grit further in on the substrate, but it could be assumed that the density further in was at least a factor of 10 less than close to the edge, as was the case for the other substrates, and hence, less than $2 \cdot 10^4\,\mathrm{cm}^2$.

CZT

Particles with size >5 µm were observed primarily near the edges of substrate A. Fig. 4.3b shows a particle that was 13 µm long and 5 µm wide. A comparison between the corresponding EDS spectrum of the particle and the substrate surface spectrum revealed that the particle consisted of the same material as the underlying substrate. It could be debris from the cutting and polishing of the substrate and the making of bevelled edges by the vendor.

Titanium

Particles with sharp edges and sizes of >5 µm were observed in the upper left corner of the substrate. The particles appeared darker than the CZT particles in SEM and with sharper edges. The corresponding EDS spectrum of the particle revealed that the particle mainly consisted of titanium. Fig. 4.3c shows a titanium particle that was 8 µm long and 4 µm wide. The sharp edges indicate that the particle had not not been used as polishing grit because the edges had been rounded in that case. Unfortunately, these particles probably had settled on the substrate during the study. A new substrate holder was made for XPS measurements out of titanium in the machine shop. When mounting the substrate in the holder with a screw, some titanium particles were made. However, they were confined to

a small area in the upper left corner of the substrate. SEM and EDS measurements of particles from the XPS holder, collected with an adhesive carbon tab, confirmed that the same type of titanium particles was found on the XPS holder.

4.1.2 Surface Scratches and Roughness

The as-received surface of substrate A was carefully polished by the vendor, as seen in Fig. 4.4. The surface scratches most likely had shallow depth since they could not be observed in the dark field images of substrate A, see Fig. 4.1.

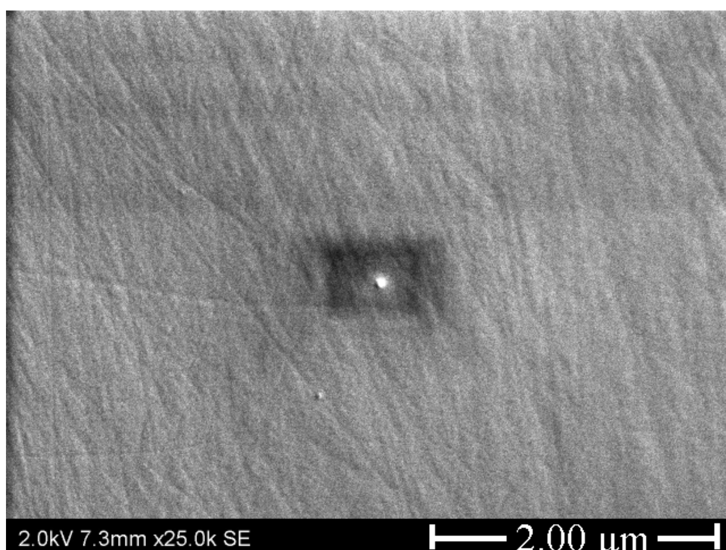

Figure 4.4: High resolution SEM image of the surface of substrate A. The dark square was carbon deposited on the surface while focusing the beam at a higher magnification.

The as-received substrate A was characterised for surface topography by AFM. Images of 5 µm × 5 µm areas were taken at three different locations on the substrate surface: near the centre, upper edge, and upper left corner, as seen in Fig. 4.5. The RMS roughness of substrate A was 0.30 nm–0.31 nm at both the centre and around the edges and 0.41 nm at the corner. The low RMS roughness indicates the absence of large scratches. The typical surface scratches were between 10 nm–20 nm wide and 1 nm deep. While the largest polishing scratches were 0.2 µm wide and 5 nm deep.

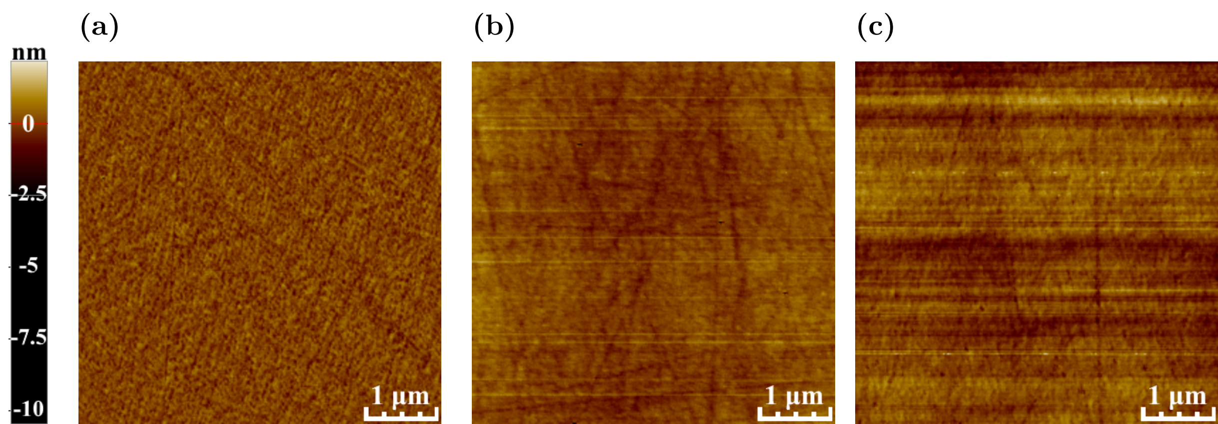

Figure 4.5: AFM measurements of the as-received substrate A. Images of 5 µm × 5 µm areas are taken at three different locations on the substrate surface: (a) near the centre, RMS roughness 0.31 nm; (b) near the upper edge, RMS roughness 0.30 nm; and (c) near the upper left corner, RMS roughness 0.41 nm.

4.1.3 Impurity Analysis – XPS

XPS analysis was performed on the as-received substrate A to determine the composition of the outermost layers of the substrate (∼80 Å). The centre of the 30 mm × 30 mm CZT wafer was analysed using XPS. With a large beam size of 1 cm, it should be possible to detect traces of impurity elements over a large area, but not locate them to specific particles or small areas. Unfortunately, something was broken on the old analyser, resulting in low signal intensity and no detection of impurities or small concentrations of elements. The ever-present oxide and carbon overlayers further decreased any small signals. Therefore, the XPS only provided information about the following elements: Te, Cd, O, and C, see Fig. 4.6. The reasoning behind not performing XPS analysis on any of the other substrates was that it would not be possible to detect the presence of impurities or small concentrations of elements with the XPS equipment at hand.

The atomic concentrations were calculated using Eq. (2.12) with intensity peak areas and the following experimentally measured atomic sensitivity factors, determined earlier at FFI (Hirsch et al., 1999): Cd $3d_{5/2}$ (0.56), Te $3d_{5/2}$ (1.00), O 1s (0.13), and C 1s (0.05). The results of the XPS analysis of substrate A can be seen in Table 4.1. $Cd_{0.96}Zn_{0.04}Te$ should consist of 48 at. % cadmium, 2 at. % zinc and 50 at. % tellurium, but zinc was not detected and the atomic concentration of Cd was only 75 % of that of Te, it should be 96 %. The higher than expected Te concentration can be explained by the formation of a Te oxide layer on the surface. By inserting the ratio between Te in $Cd_{1-y}Zn_yTe$ signal and Te in TeO signal of 1.3 into Eq. (2.13), the Te oxide layer thickness was calculated to be 0.96 nm. An atomic concentration of 23.5 at. % carbon was found, which can be explained by an overlayer of carbon.

Table 4.1: Results from the XPS analysis at the centre of the 30 × 30 mm as-received (111)B CdZnTe substrate A (atomic concentration %).

Cd (at.%)	**Te** (at.%)	**O** (at.%)	**C** (at.%)	**Te oxide thickness** (nm)
18.8	25.1	32.6	23.5	0.96

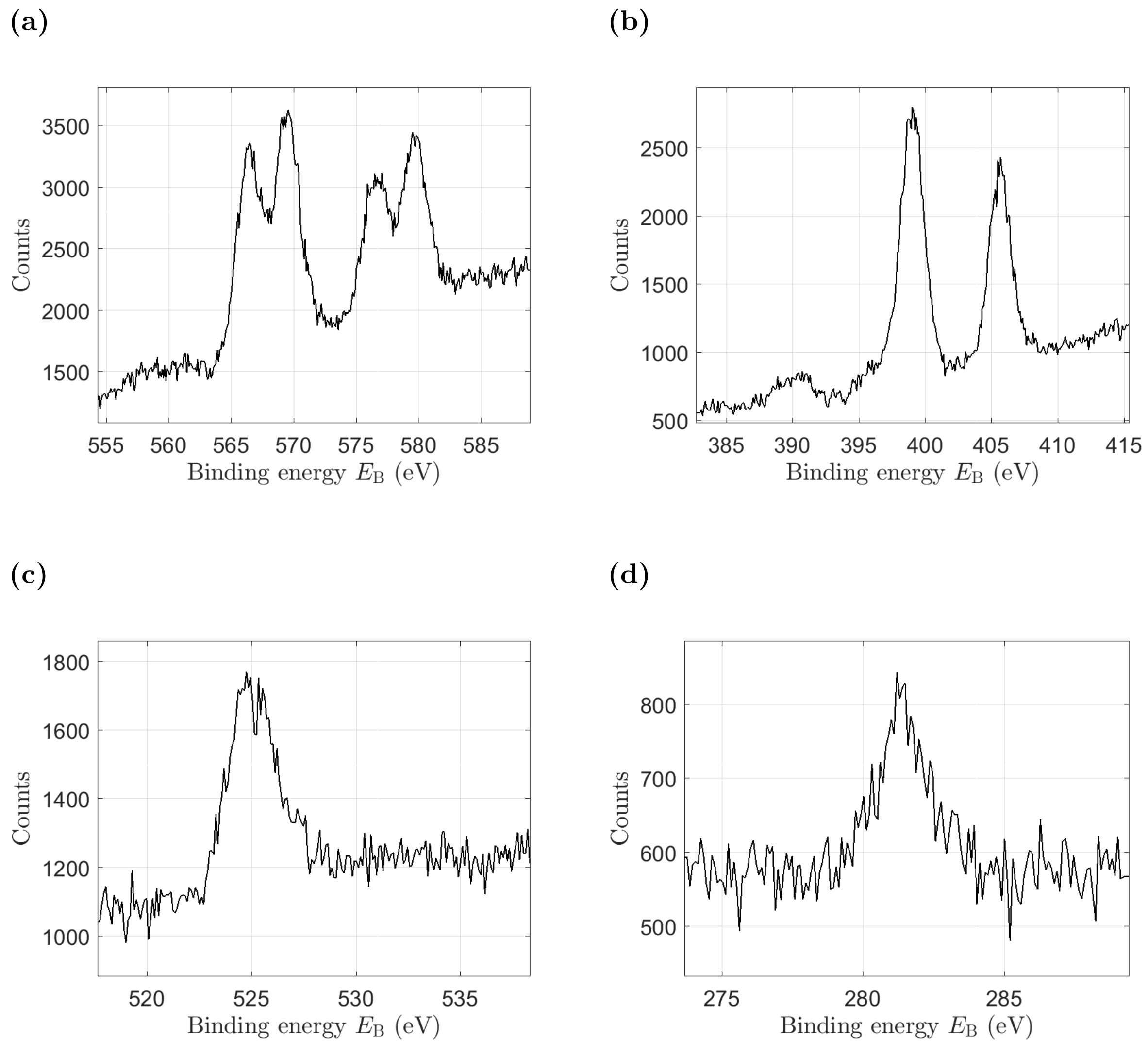

Figure 4.6: XPS spectra from substrate A that displays the number of detected electrons (counts) as a function of their corresponding binding energy, E_B (eV). The spectra were acquired using the Mg anode. The peaks in the spectrum were: (a) Te 3d with extra peaks due to tellurium oxide; (b) Cd 3d; (c) O 1s; and (d) C 1s.

4.1.4 Impurity Analysis – EDS

Since the XPS equipment did not detect small concentrations of elements, EDS was used to get a quantitative analysis of the chemical composition of the substrate. The spectra were taken using an accelerating voltage of 10.0 kV to ensure an electron energy larger than the peaks of interest, but still limited in order to not get too deep into the sample, a large probe current to maximise the throughput, and a live acquisition time of 1200 s to get reliable statistics and less noise. The resulting EDS spectrum from the centre of the substrate can be seen in Fig. 4.7.

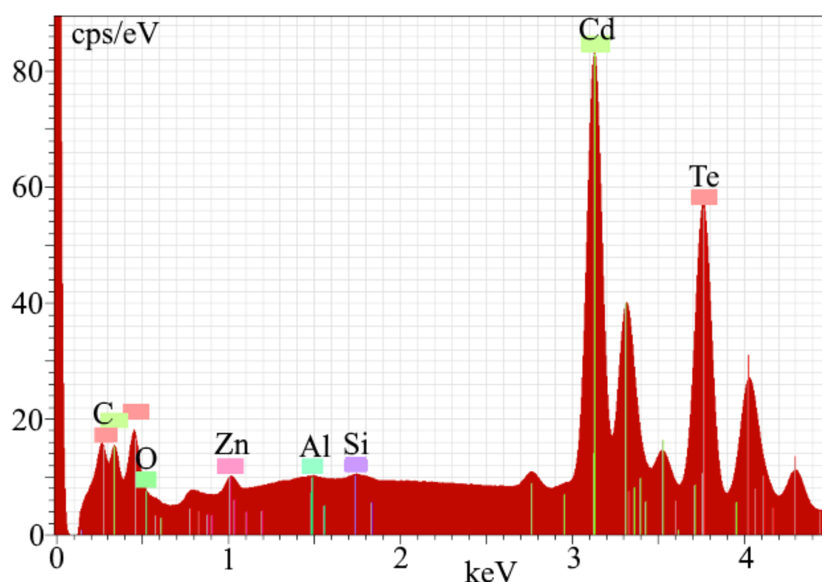

Figure 4.7: EDS spectrum from a 1270 µm × 890 µm area in the centre of the as-received substrate A.

The spectra were collected from surface areas of 1270 µm × 890 µm. The electron interaction depth was calculated by the Quantax software to be 0.4 µm. That meant that characteristic X-rays from elements as far in as 0.4 µm below the surface were detected. In comparison, the XPS detected the electrons that escaped from the outermost ∼10 nm. Hence, EDS was not as surface sensitive and more than just the top surface layer was probed. This is part of the reason for the difference in the atomic concentrations between the XPS and EDS results for substrate A. The observed silica and alumina particles had a diameter of about 50 nm. Hence, one monolayer of these would cover ∼12.5 % of the interaction volume, although a little more of the signal.

The EDS surface analysis identified the following elements: Cd, Te, Zn, Al, Si, C, and O, as seen in Table 4.2. The relative concentrations of Cd, Zn, and Te had an error of

less than one percentage point from the expected value of 48 at. % cadmium, 2 at. % zinc, and 50 at. % tellurium. The EDS spectrum shown in Fig. 4.3a demonstrates that some of the aluminium contamination came from the residual Al_2O_3 polishing grit. The silicon contamination could come from residual SiO_2 polishing grit, but future EDS measurements are required to confirm this hypothesis. Silicon and alumina were detected in close proximity to the centre as well as near the edges and corners. This indicates that the polishing grit was not exclusively near the edges and corners.

Table 4.2: Results of the EDS impurity analysis at three different locations on the 30 mm × 30 mm as-received (111)B CZT substrate A (atomic concentration %). The X-ray signal was acquired from a 1270 µm × 890 µm area near the centre, upper edge, and upper left corner.

	Te (at.%)	**Cd** (at.%)	**Zn** (at.%)	**Al** (at.%)	**Si** (at.%)	**C** (at.%)	**O** (at.%)
Near centre	46.14	45.60	1.90	0.21	0.51	4.97	0.68
Near edge	45.94	45.32	1.98	0.19	0.45	5.34	0.78
Near corner	46.05	45.46	1.89	0.40	0.51	4.95	0.73

4.1.5 IR Characterisation

FTIR transmission spectra were recorded from an 11×11 grid on the as-received substrate A. The grid points were placed 2.0 mm from the edge and had 2.6 mm between nearest neighbours. All but four measurements had an IR transmittance between 62 % and 67 % in the wavenumber range between 1000 cm^{-1} and 5000 cm^{-1}, see Fig. 4.8a. The spikes near $k = 4500\,\text{cm}^{-1}$ and $k = 5000\,\text{cm}^{-1}$ were an artefact of the FTIR instrument and should not be considered. A map of the transmission at $k = 500\,\text{cm}^{-1}$ can be seen in Fig. 4.8b.

The two factors that are primarily responsible for the reduction in IR transmittance of CZT are free carrier absorption and scattering from precipitates (Yadava et al., 1994). Yujie et al. (2004) used the transmittance at the wavenumbers 1000 cm^{-1} (T_{1000}) and 5000 cm^{-1} (T_{5000}), and the ratio of T_{1000} to T_{5000} to determine which of the two mechanisms that were most significant. Their analysis provided a qualitative determination of the density and size of Te precipitates, the free carrier concentration, and the resistivity for CZT substrates.

Almost all the spectra from substrate A had values of T_{5000} between 63 %–67 %, T_{1000} between 62 %–64 %, and T_{1000}/T_{5000} approached one from below. Following the analysis

of Yujie et al., a CZT substrate with these parameters is free from precipitates and has a low free carrier concentration. Combined with the extremely low particle density, it does indeed seem that the quality of this substrate, as-received, is very good.

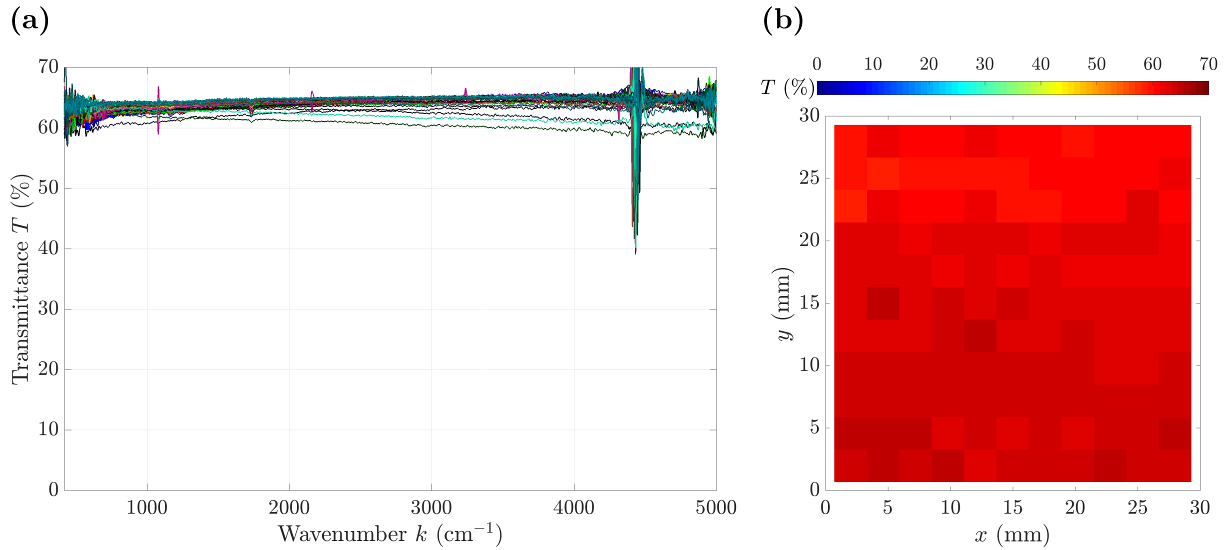

Figure 4.8: FTIR measurements recorded from a 11 × 11 grid on the as-received 30 mm × 30 mm (111)B-oriented substrate A: (a) Transmission spectra; (b) transmission map at wavenumber $k = 500\,\text{cm}^{-1}$ showing the transmittance T in percentage of incoming light at each grid point. The spikes near $k = 4500\,\text{cm}^{-1}$ and $k = 5000\,\text{cm}^{-1}$ were artefacts of the FTIR instrument.

Near-IR microscopy images of the tellurium precipitate distribution in the CZT substrate can be seen in Fig. 4.9. The observation of Te precipitates contradict the analysis of Yujie et al.. A series of 11 near-IR microscopy images focusing through the complete depth of the substrate was acquired, each image was ∼80 µm deeper into the substrate. The Te precipitate density was rather uniform throughout the bulk of the substrate. An average of 40 tellurium precipitates was in focus per near-IR image. Strings of Te precipitates were observed as well as single Te precipitates.

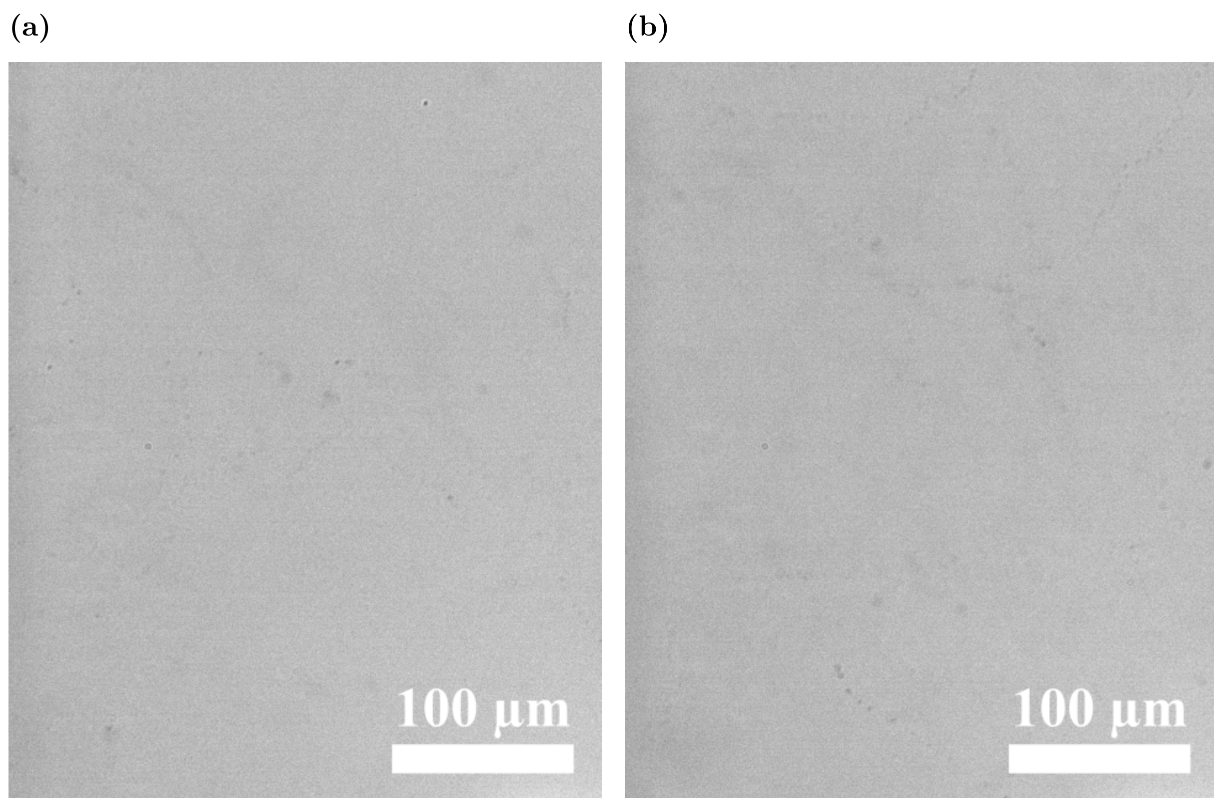

Figure 4.9: Near-IR microscopy images pf Te precipitate density and distribution near the centre of the 30 mm × 30 mm (111)B-oriented substrate A. Image area is 324 µm × 405 µm. (a) The (111)B surface; (b) ∼240 µm below the (111)B surface.

4.2 Surface Analysis of As-Received Substrate B

Substrate B was from an alternative source (vendor B) and had only been roughly polished after being sliced from a bulk crystal. In previous work (Lauten, 2017), the as-received (111)B-oriented substrate B was characterised for polishing damage, defects, and residual particles using optical microscopy and SEM with EDS. The results are reiterated in this section to better present the full scope of the study. In addition to the previously used methods, AFM, near-IR transmission microscopy, and FTIR were used to study the as-received substrate.

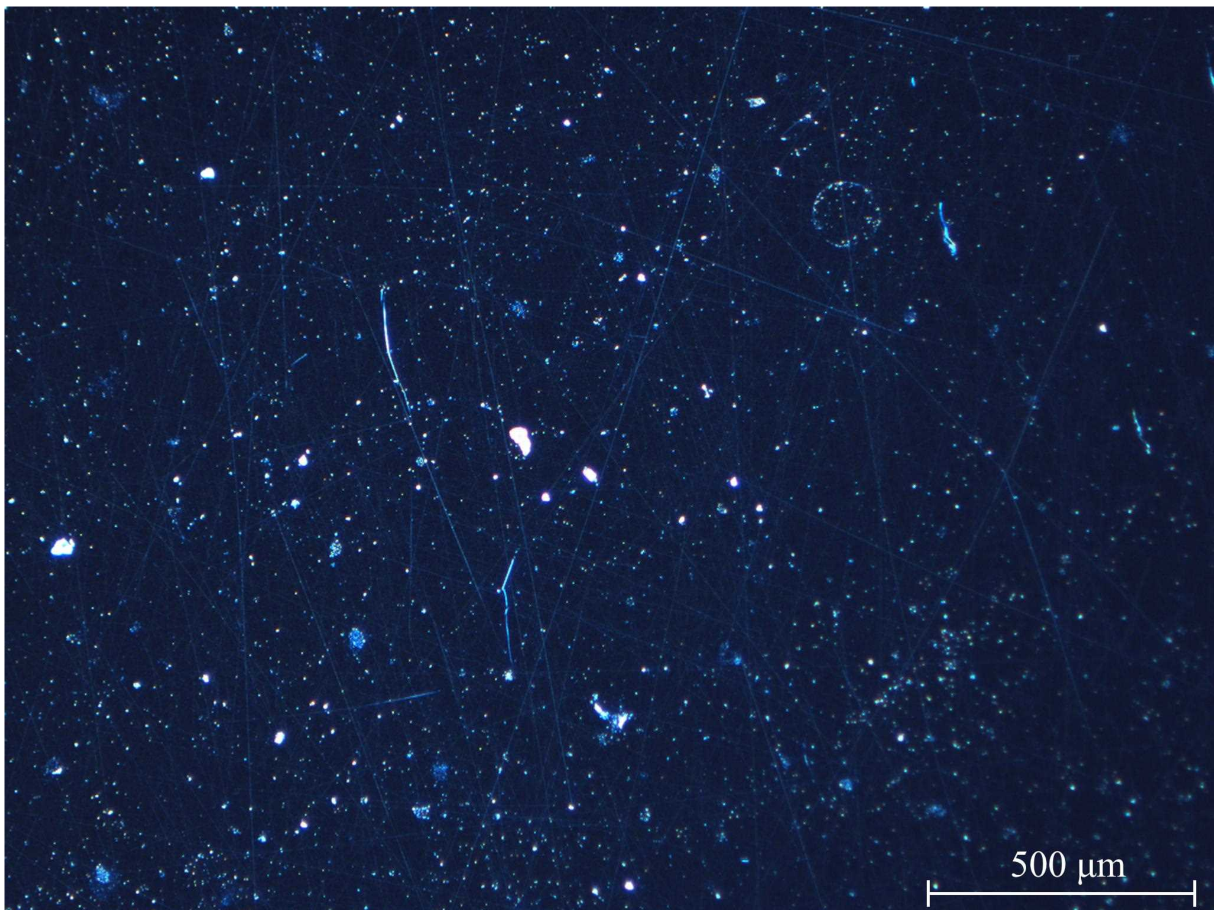

Figure 4.10: Dark field images of substrate B captured through the optical microscope Leica DM RXA2 at the centre of the substrate.

The surface of the as-received substrate B looked completely different from that of the as-received substrate A. Fig. 4.10 shows typical dark field images from the surface of substrate B at the corner, edge, and centre of the substrate. There were polishing scratches in all directions and with varying width covering the surface of substrate B. Particles

and morphological defects with both small (0.5 µm–5 µm) and large (5 µm–50 µm) diameter were present on the surface. By counting the number of bright spots in the dark field image, the density of particle and morphological defects with features >0.5 µm was estimated to be $1 \cdot 10^5\,\mathrm{cm}^{-2}$, both at the centre and edges of the surface of substrate B.

The difference between substrate A and substrate B was significant. Substrate B had a density of particles and morphological defects that was 100-1000 times larger than on substrate A. A large part of this can presumably be explained by the more thorough surface preparation that substrate A had been subjected to. Substrate A had a final polishing and an etch before it was delivered, while substrate B was roughly polished and particles on the surface had not been removed.

A comparison between the dark field image and a SEM image of the same area of substrate B, as seen in Fig. 4.11, reveals that the brightest spots in the dark field image are from cavities in the substrate surface and that particles as small as 0.5 µm can be seen in the dark field image. The dark stains, on the other hand, were not visible in the dark field image. This indicates that the dark stains do not have sharp edges or other pointy features.

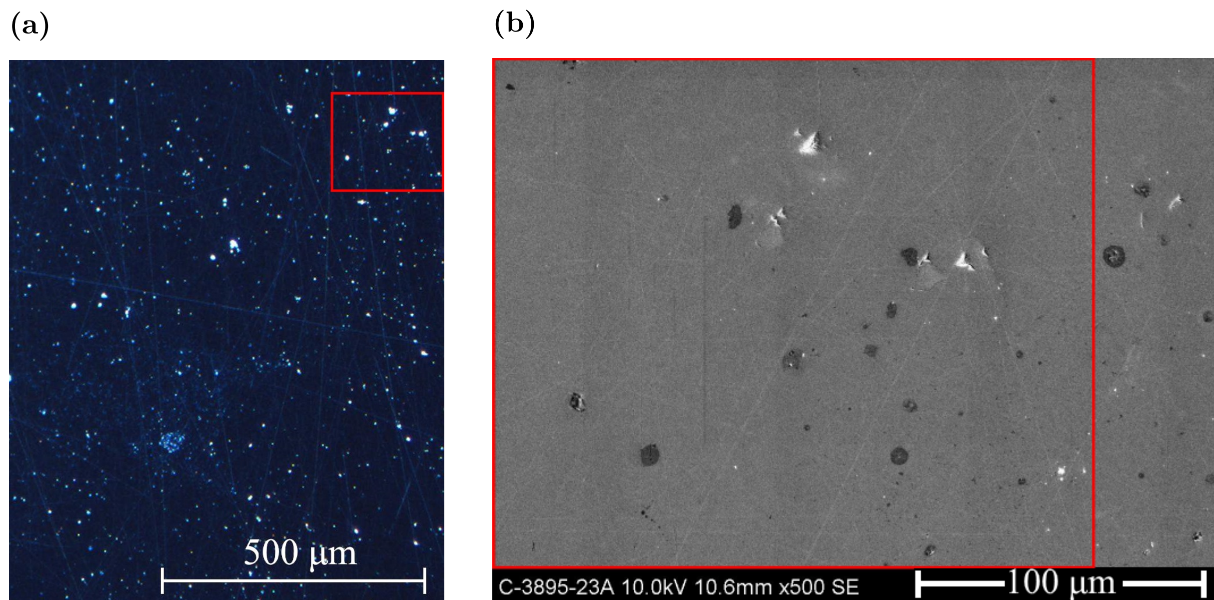

Figure 4.11: Comparison of (a) a dark field microscopy image captured through the optical microscope Leica DM RXA2 and (b) a scanning electron microscopy (SEM) image taken at the same location on the as-received substrate B as the dark field image.

Fig. 4.12a shows a SEM image from the centre of substrate B, taken at low magnification

(60×). There were some bright stains at the top of the image, a dark spot down in the right corner, and several bright spots distributed over the surface. A SEM image at the same position at magnification 500×, shown in Fig. 4.12b, revealed the existence of surface scratches, dark stains of different sizes, and some even smaller bright spots on the surface. These features will be described in the following paragraphs by, among other methods, SEM images at even higher magnification.

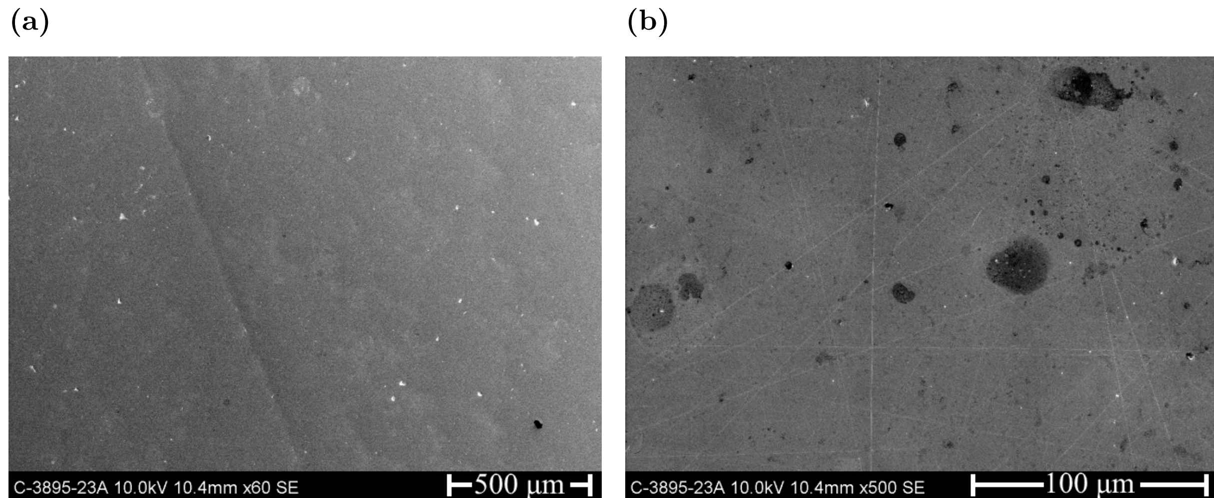

Figure 4.12: SEM images of a typical area in the middle of substrate B at (a) 60× magnification; and (b) 500× magnification.

4.2.1 Particles and Surface Features

Seven different types of particles and surface features were observed on the surface of substrate B. These seven can be seen in Fig. 4.13.

Residual Polishing Grit (alumina and silica)

Bright particles with varying sizes were observed on the substrate surface, see Fig. 4.14a. When looking at one of the accumulations at greater magnification, see Fig. 4.14b, it became evident that the large particles were agglomerations of smaller particles. The smaller particles were spherical and had a diameter between 50 nm and 100 nm. The typical width of the particle agglomerations was 0.5-3 µm. The attraction between the small particles can be explained by electrostatic attractive forces between the particles due to different surface charge (Allen et al., 2001).

(a)

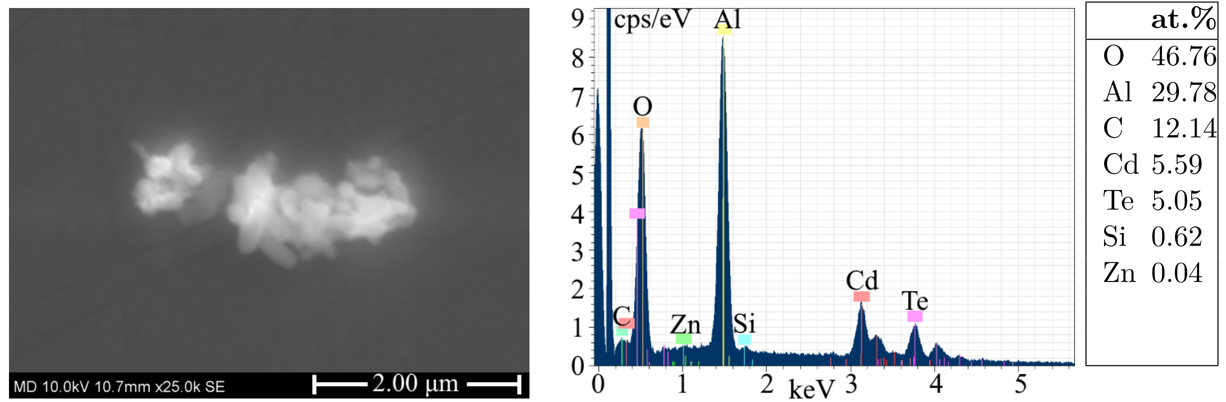

(b)

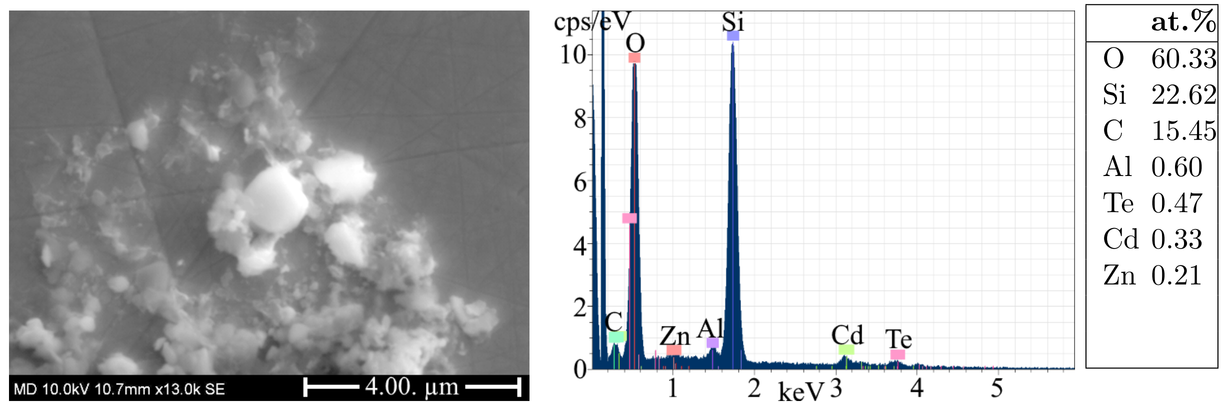

(c)

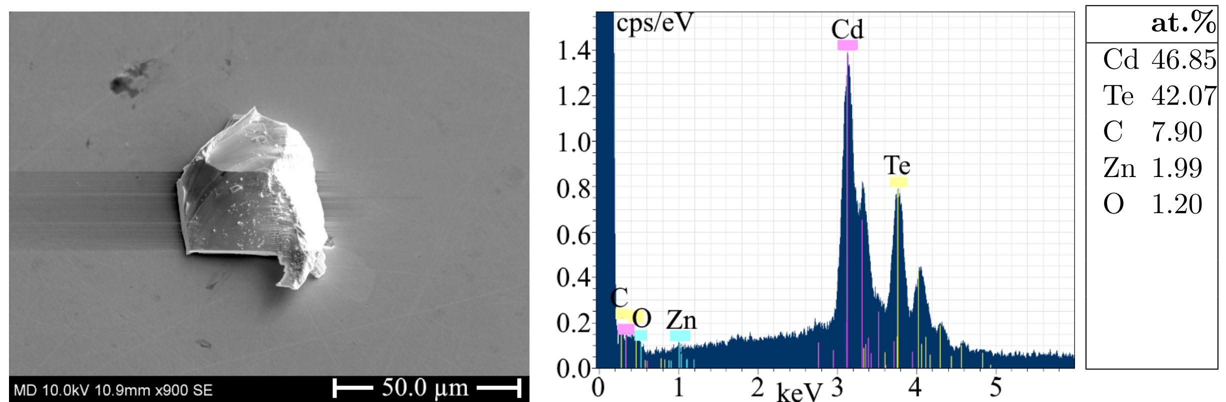

Figure 4.13: High resolution SEM images of one void and six different types of particles found on the as-received substrate B and the corresponding EDS spectra and atomic compositions: (a) alumina (Al_2O_3) polishing grit; (b) silica (SiO_2) polishing grit; (c) CZT paticle; (d) carbon-based particle; (e) NaClO; (f) iron (Fe); and (g) void.

(d)

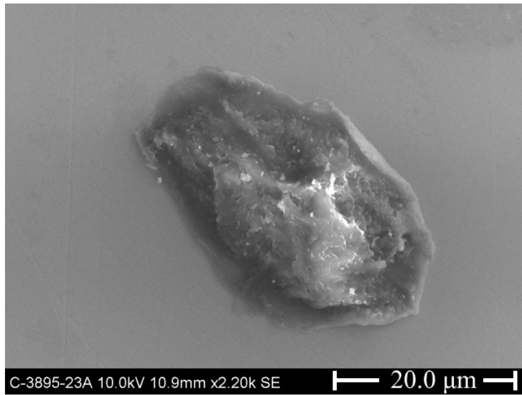

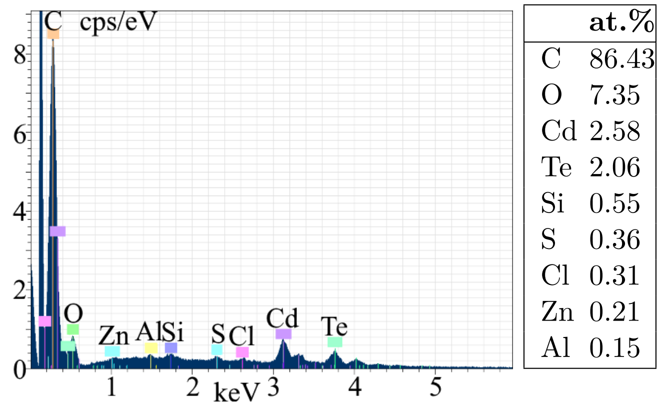

(e)

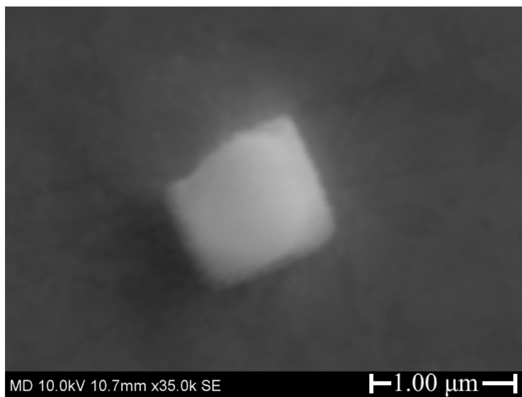

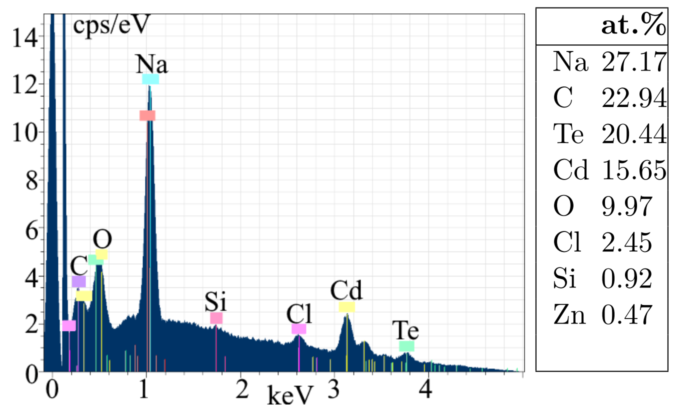

(f)

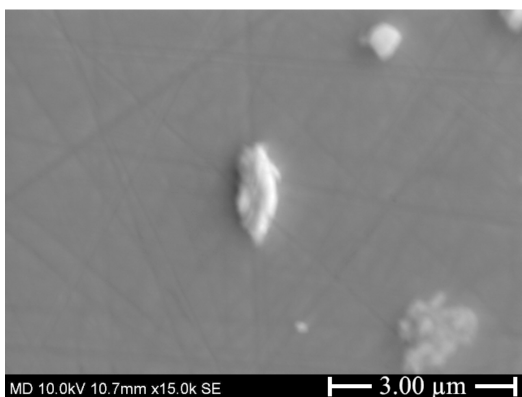

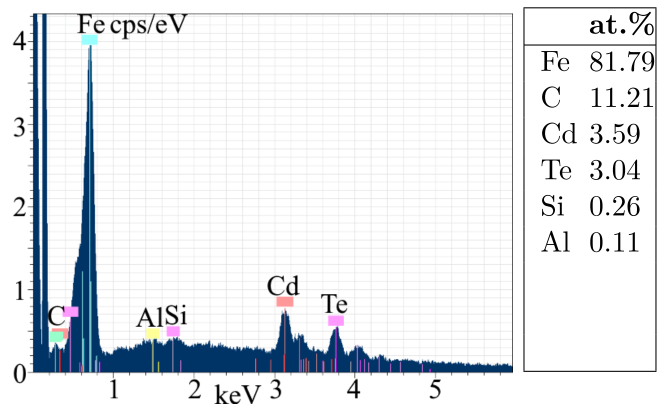

Figure 4.13: *(continued)*

(g)

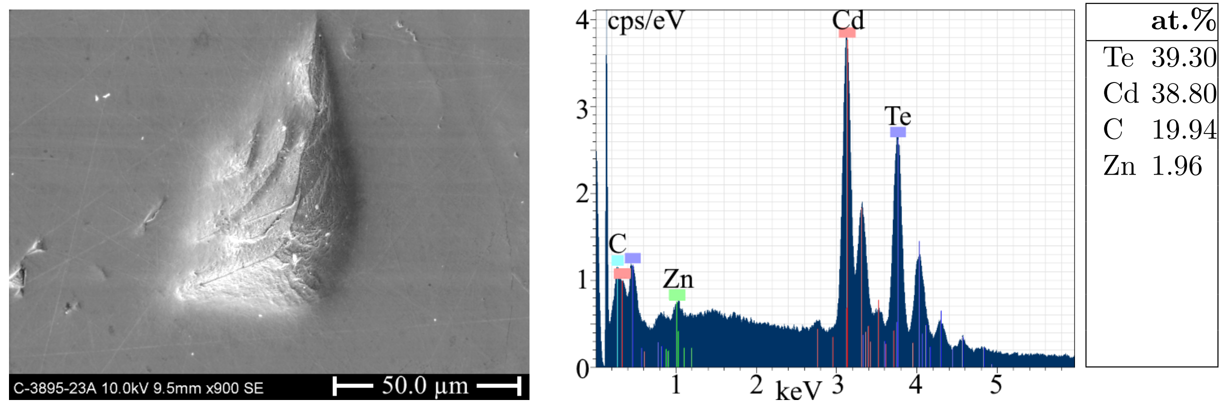

Figure 4.13: *(continued)*

(a)

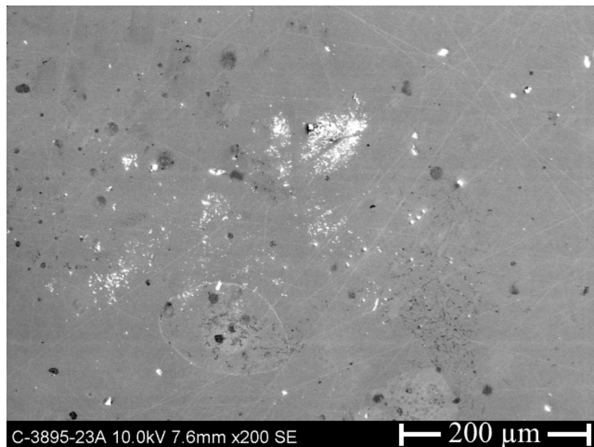

(b)

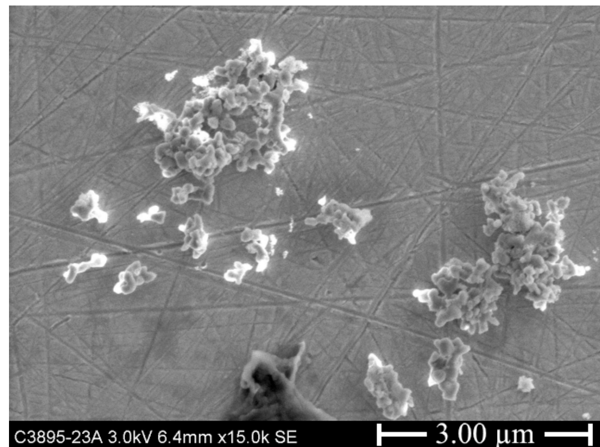

Figure 4.14: SEM images of an accumulation of polishing grit on the as-received substrate B at a magnification of (a) 200× and (b) 15000×.

An EDS spectrum of the particle revealed that the piece was composed of alumina oxide, Al_2O_3, also known as alumina, see Fig. 4.13a. The corresponding SEM image of residual polishing grit is shown next to the spectrum. The presence of alumina can be explained by the frequent use of alumina as an abrasive in polishing slurries for semiconducting material. The typical density of polishing grit was $6 \cdot 10^5\,\text{cm}^{-2}$, but the density was higher near voids, deep scratches, and at stains looking like the residue after the evaporation of a droplet.

Some of the accumulations were composed of larger particles with a diameter of 600 nm as well as the smaller ones, as seen in Fig. 4.13b. An EDS spectrum of the largest particle revealed that the piece was composed of silicon oxide, SiO_2, also known as silica. As mentioned earlier, silica is also a frequently used abrasive in polishing slurry.

CZT

Bright particles about 10 times as large as the typical polishing grit agglomerations were observed on the substrate surface, see Fig. 4.15. The size of the pieces was typically between 50 µm and 100 µm. By comparing the EDS spectrum of the particle with the spectrum of the substrate surface, see Fig. 4.13c, it became apparent that the particles had the same composition as the surrounding substrate. This indicates that the pieces could be debris from the polishing or cutting of the substrate.

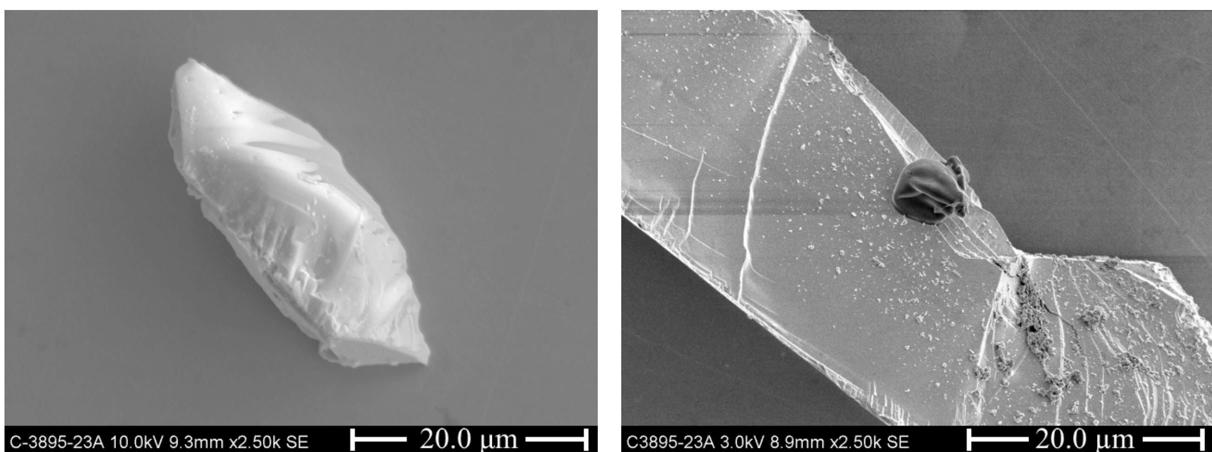

Figure 4.15: SEM images of CZT particles on the as-revceived substrate B.

Carbon-based particle

Dark particles, which typically had a size between 20 µm–30 µm, were observed on the substrate surface, as seen in Fig. 4.13d. The EDS spectrum of this particle showed a high intensity from the carbon signal. The particles could be residue from mounting wax, which was used to hold the substrate while it was being cut and polished. Some small peaks of silicon and aluminium were observed as well, but they probably stemmed from the residual polishing grit that can be seen in on the surface of the carbon-based particle.

NaClO

An area with lots of circular particles with a diameter between 100 nm–1 µm was observed near one of the edges of substrate B, see Fig. 4.16. The area was separated from the rest of the substrate by a dark borderline. An EDS spectrum of one particle with a diameter of 1 µm, see Fig. 4.13e, reveals that the particle consists of Na, Cl, and O. The particles could be NaClO which typically is used after polishing as a standard cleaner to remove polishing slurry particles (Benson et al., 2015). The dark borderline was not possible to get quantified with EDS, but it could be a residue of the cleaning solution.

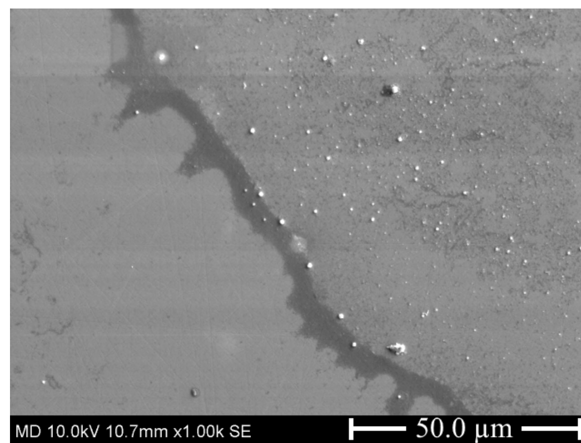

Figure 4.16: SEM image of NaClO particles on substrate B.

4.2.2 Iron Particle

A small particle that was 1.5 µm long and 0.6 µm wide can be seen in Fig. 4.13f with its corresponding EDS spectrum. The EDS spectrum of the particle revealed that the particle

consisted mainly of Fe. Iron is a potential contaminate in polishing grit slurry, but it could also originate in cross-contamination from the polishing of other semiconductors, i.e. InP (Benson et al., 2015).

Voids

Irregular shaped voids were observed all over the surface of substrate B, see Fig. 4.17. The width of the voids tended to be between 5 µm–100 µm and AFM measurements gave that the voids were between 1 µm–3 µm deep, see Fig. 4.18. EDS detected $Cd_{0.96}Zn_{0.04}Te$ both on the inside edges of the voids and around the voids, see Fig. 4.13g. This revealed that the voids had the same composition as the substrate surface.

(a)

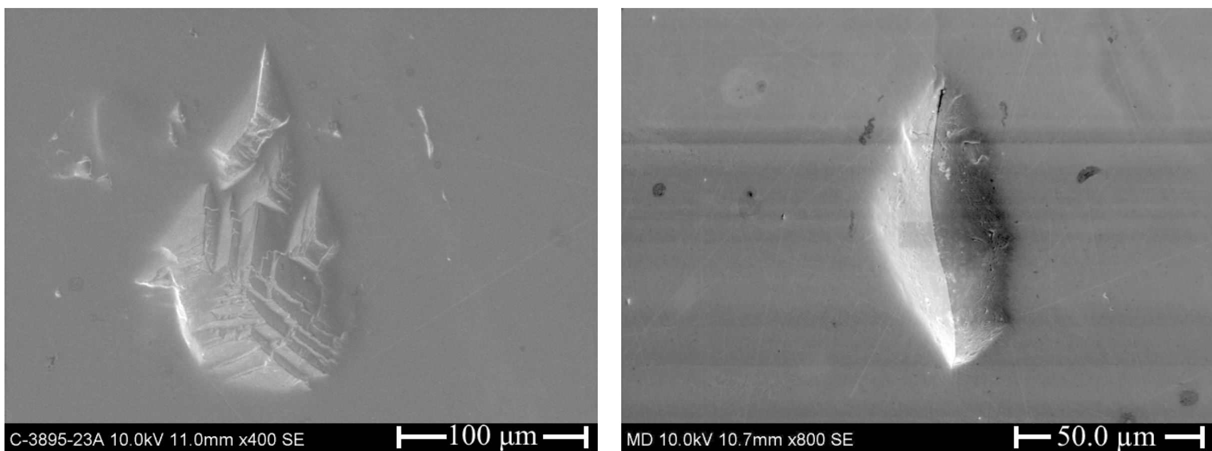

(b)

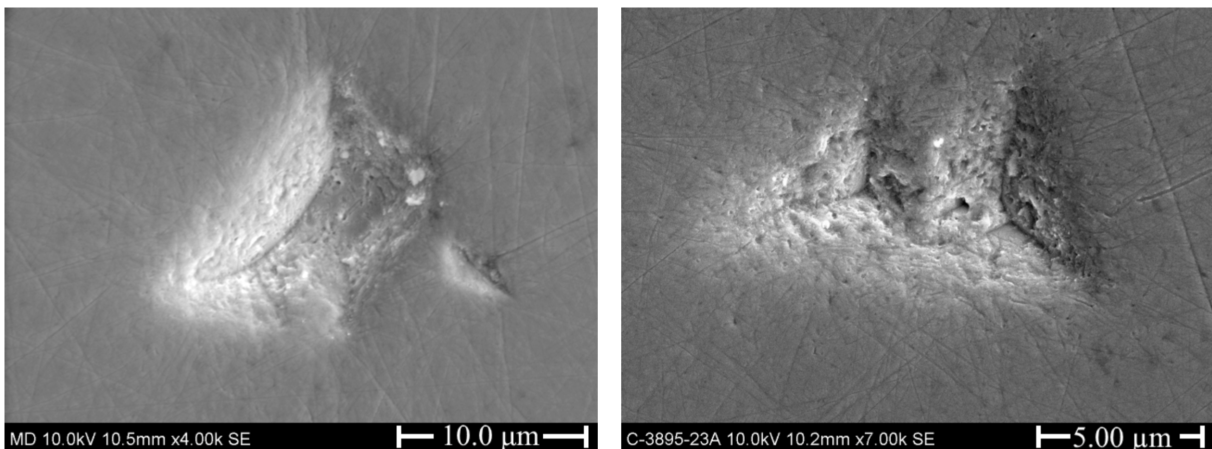

Figure 4.17: SEM images of (a) large voids >10 µm and (b) small voids <10 µm on the as-received substrate B.

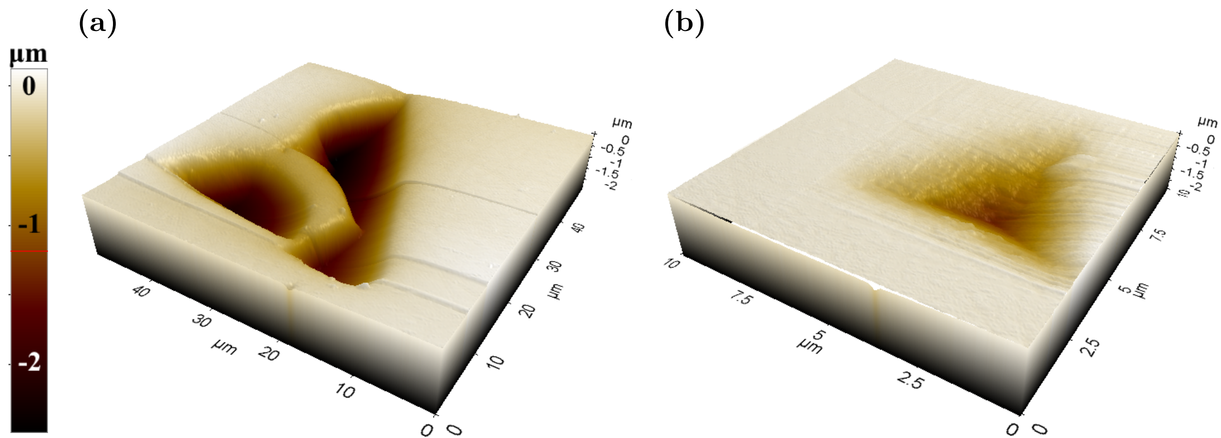

Figure 4.18: AFM measurements of (a) a 40 µm wide void and (b) a 7 µm wide void on the as-received substrate B displayed as images of 50 µm × 50 µm and 10 µm × 10 µm areas respectively.

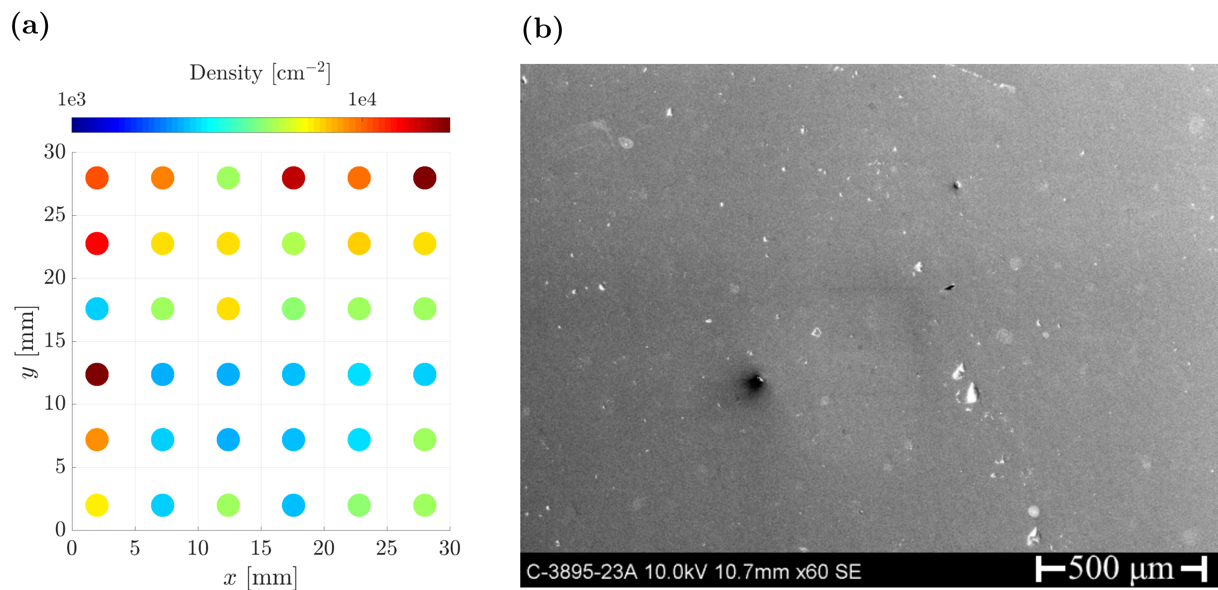

Figure 4.19: (a) A map of the void density at 36 different locations on the as-received 30 mm × 30 mm substrate B. The density measurements were obtained by counting the number of voids in SEM images covering 254 µm × 178 µm areas. In total, 0.2 % of the substrate surface was measured. The void density was observed to vary between $2 \cdot 10^3\,\mathrm{cm}^{-2}$–$2 \cdot 10^4\,\mathrm{cm}^{-2}$. (b) An image from the upper right corner of the grid where the void density is highest.

Some of the smaller voids have a threefold symmetry, as seen in Fig. 4.17b. The larger voids >10 µm tended to have multiple angular features, as seen in Fig. 4.17a. Reddy et al. (2013) speculate that these voids originally was occupied by a tellurium precipitate that was knocked loose during surface preparation, i.e. substrate polishing in this case, leaving a void on the surface. This theory is supported by the fact that tellurium precipitates often are crystalline and could be the source of the angular features of the voids (Wang et al., 2008).

The void density was found to be between $2 \cdot 10^3\,\mathrm{cm}^{-2}$–$2 \cdot 10^4\,\mathrm{cm}^{-2}$. The average void density was $7 \cdot 10^3\,\mathrm{cm}^{-2}$ with a standard deviation of $5 \cdot 10^3\,\mathrm{cm}^{-2}$. A graphical representation of the void density at different locations on substrate B can be seen in Fig. 4.19.

4.2.3 Circular stains

Four typical stains that were observed on the substrate surface with SEM is shown in Fig. 4.20. One type of stain had a bright background with a darker centre in one part of the stain, as seen in Fig. 4.20a–b. The size of the bright stains varies from 30 µm to 150 µm. The density of this type of stain was estimated from the SEM grid map to be $2 \cdot 10^2\,\mathrm{cm}^{-2}$. These stains could be residue from the evaporation of a droplet on the surface, with the centre consisting of the impurities that were carried by the surface tension of the droplet.

A second type of stain, as seen Fig. 4.20c, appeared dark in the SEM images and had sizes ranging between 8 µm–15 µm. The density of these stains was estimated from the SEM grid map to be $1 \cdot 10^3\,\mathrm{cm}^{-2}$. The third type of stain appeared as a dark shadow on the substrate surface when observed in SEM, see Fig. 4.20d. The typical size of these stains were 10 µm–50 µm and the density of these stains was estimated to be $1 \cdot 10^4\,\mathrm{cm}^{-2}$. The observed stains do not contribute any additional signal to the EDS spectrum due to their thin layer on the surface. Hence, it has not been possible to identify what the composition of the stains were.

4.2.4 Surface Scratches and Roughness

The surface of substrate B had been subjected to a coarse polish, and scratches stemming from the polishing could be seen on the surface. The scratches were typically between

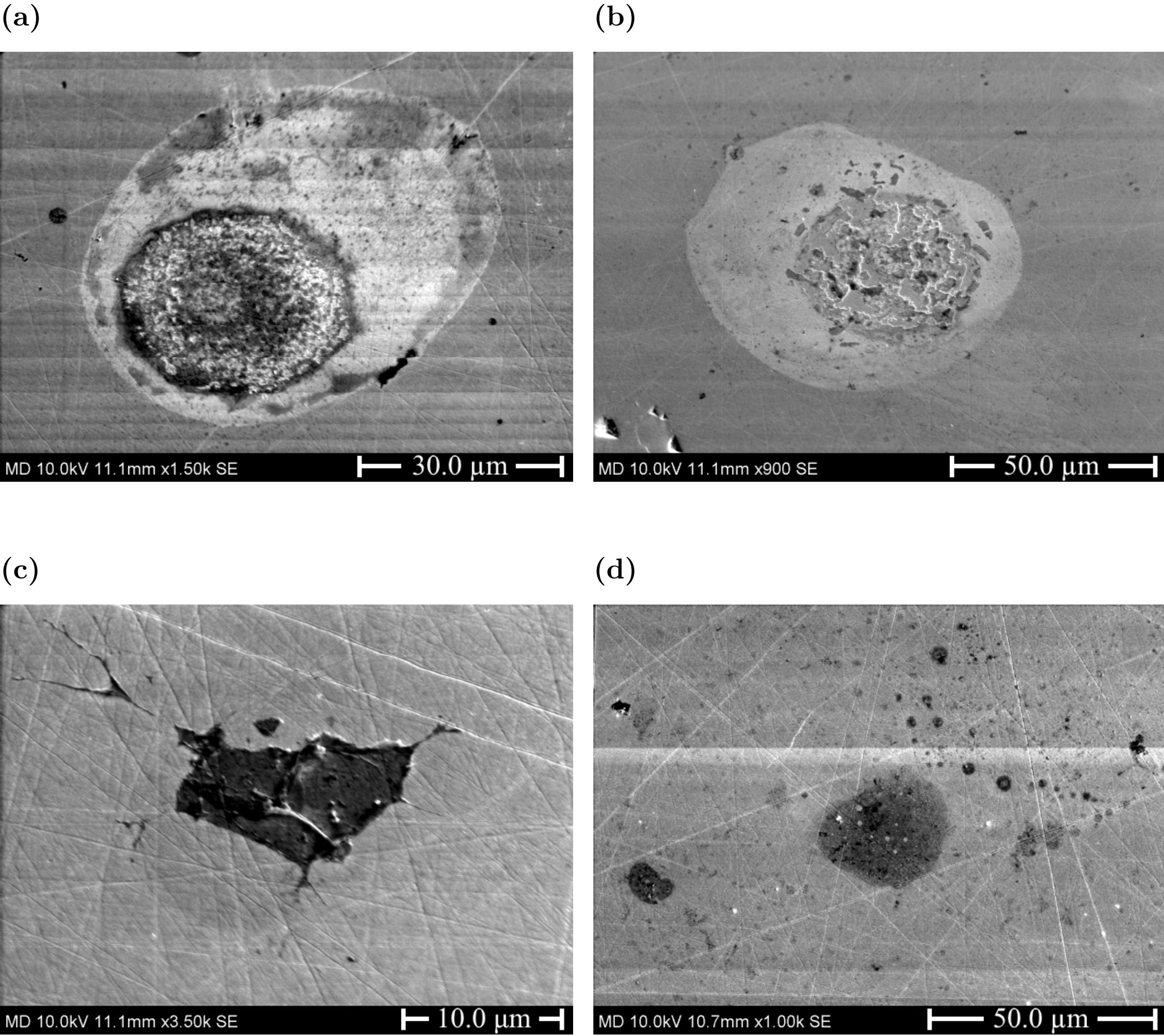

Figure 4.20: SEM images of (a)–(b) bright and (c)–(d) dark stains on substrate B.

10 nm–100 nm wide, as seen in Fig. 4.21a. Some large scratches were located close to the edges and were as wide as 1 µm, as seen in Fig. 4.21b. The latter were not as evenly distributed as the polishing scratches. These types of scratches are typical of handling tools, i.e. the teflon tweezers, and could be caused by the vendor or by the handling at FFI. The surface scratches on substrate B are most likely deeper than those on substrate A since they are visible on the dark field images of substrate B, see Fig. 4.10. Substrate B needs a fine polishing before growth to get rid of the scratches.

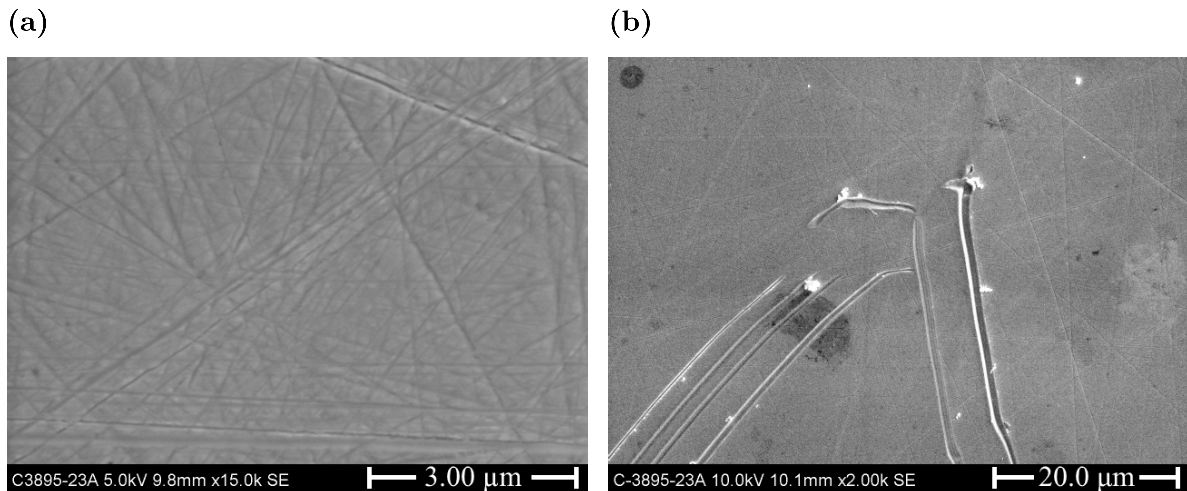

Figure 4.21: SEM images of (a) polishing scratches and (b) deep scratches on substrate B.

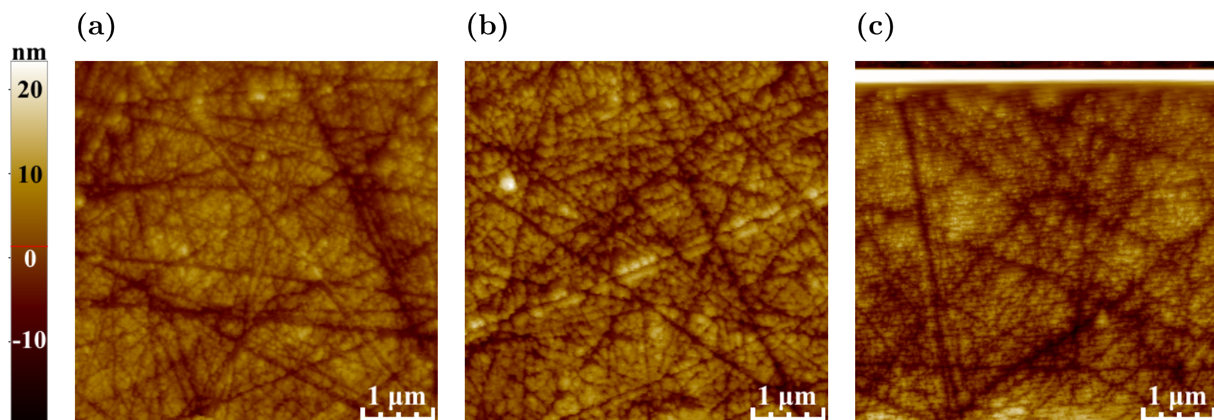

Figure 4.22: AFM measurements of the as-received substrate B. Images of 5 µm×5 µm areas are taken at three different locations on the substrate surface: (a) near the centre, RMS roughness 3.7 nm; (b) near the left edge, RMS roughness 4.8 nm; and (c) near the upper left corner, RMS roughness 4.8 nm. The bright line near the top of the image is due to the tip losing track of the surface.

Complementary AFM images are shown in Fig. 4.22 where 5 µm × 5 µm areas were measured at three different locations on the substrate surface: near the centre, upper edge, and upper left corner. The RMS roughness of substrate B was ∼3.7 nm at the centre and ∼4.8 nm around the edges and corners, which was larger than the RMS roughness measured on substrate A by a factor of 12–16. The large RMS roughness indicates that the substrate had large scratches and was inferior to substrate A. With too large RMS roughness, the surface appears 3-dimensional instead of 2-dimensional, resulting in poorer film growth (R. Haakenaasen, personal communication, May 29, 2017). The CZT substrate surfaces are easily damaged by surface scratches caused by mechanical lapping (Egan et al., 2009). The final polishing step performed by the vendor had left scratches on the surface, as can be observed in all the AFM images. The largest polishing scratches on substrate B were 0.3 µm wide and 15 nm deep.

4.2.5 Impurity Analysis – EDS

EDS impurity analysis was performed on the as-received substrate B. Three locations on the surface – the centre, the edge, and the corner – were analysed. The results of this analysis can be seen in Table 4.3. The only elements found above the EDS detection limit, in addition to Cd, Zn, and Te, were Al, Si, C, and O. The relative concentrations of Cd, Zn, and Te had an error of less than one percentage point from the expected value of 48 at. % cadmium, 2 at. % zinc, and 50 at. % tellurium. The atomic concentration of aluminium and silicon near the centre of the substrate is slightly lower compared to the concentrations near the edge and corner. The atomic concentration of silicon was twice as large as the atomic concentration of aluminium, which indicates that there was a higher occurrence of silica than alumina.

Table 4.3: Results of the EDS impurity analysis at three different locations on the 30 mm × 30 mm as-received (111)B CZT substrate B (atomic concentration %). The X-ray signal was acquired from 1270 µm × 890 µm areas near the centre, upper edge, and upper left corner.

	Te (at.%)	**Cd** (at.%)	**Zn** (at.%)	**Al** (at.%)	**Si** (at.%)	**C** (at.%)	**O** (at.%)
Near centre	45.88	45.35	2.13	0.18	0.47	4.59	1.40
Near edge	45.84	45.39	2.28	0.21	0.51	4.59	1.18
Near corner	45.86	45.45	2.28	0.36	0.49	4.23	1.33

4.2.6 IR Characterisation

FTIR transmission spectra were recorded from an 11×11 grid on the as-received substrate B2. The grid points were placed 2.0 mm from the edge and had 2.6 mm between nearest neighbours. The spectra measured in the upper half of substrate B2 had the same characteristics as substrate A, and hence, had the same properties regarding precipitates and carrier concentration as substrate A (Yujie et al., 2004). Some of the spectra measured in the lower half of the substrate deviated by having a downward slope for lower wavenumbers, see Fig. 4.23a. These spectra had a value of $T_{5000} < 60\,\%$ and $T_{1000} \ll 60\,\%$. According to Yujie et al. (2004), CZT substrates with these parameters have a higher free carrier concentration, on the order of $10^{17}\,\text{cm}^{-2}$, and a lower resistivity than the other spectra. The area of low-transmission form a semicircle in the lower part of substrate B2, as seen in Fig. 4.23b.

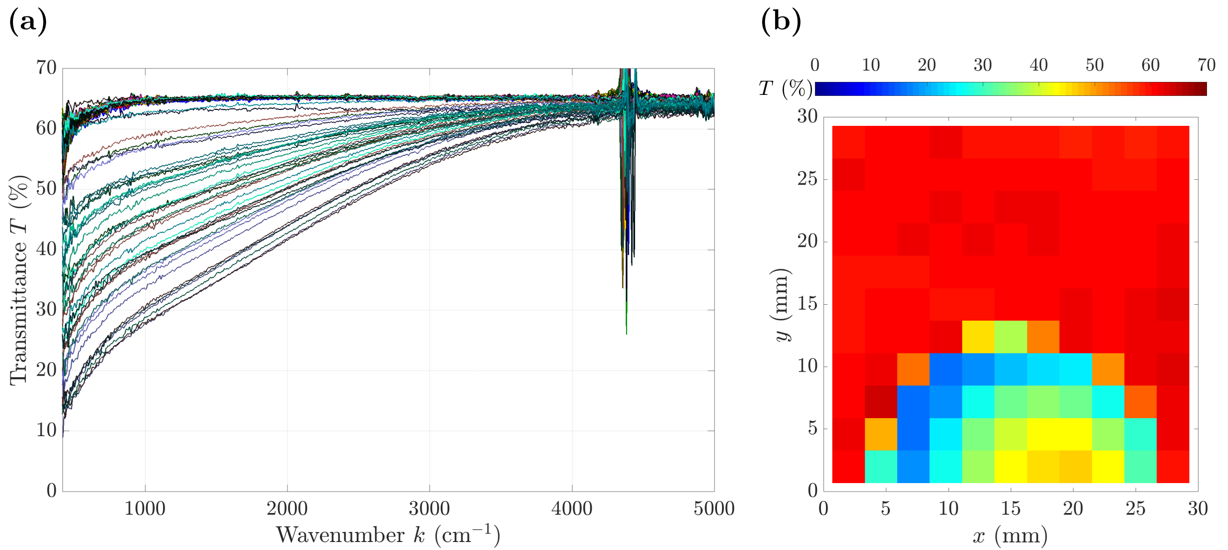

Figure 4.23: FTIR measurements recorded from a 11×11 grid on the as-received $30\,\text{mm}\times30\,\text{mm}$ (111)B-oriented substrate B2: (a) Transmission spectra; (b) transmission map at wavenumber $k = 500\,\text{cm}^{-1}$ showing the transmittance T in percentage of incoming light at each grid point. The spikes near $k = 4500\,\text{cm}^{-1}$ and $k = 5000\,\text{cm}^{-1}$ were artefacts of the FTIR instrument.

Surprisingly, the low-transmission semicircle was visible as a brighter area in the SEM images, see Fig. 4.24. The semicircle started 4.11 mm from the left edge, went around up to 13.11 mm before it went down, and ended 1.89 mm from the right edge. The major influence on SE generation is the topography of the surface, and generally, edges and other pointy parts that are facing the detector produce more SEs, and hence, these parts look brighter than the rest of the image (Goldstein et al., 2012). This was not the case for

the brighter area because AFM measurements affirmed that the surface was as uniform and planar as the surrounding substrate. Also, the average atomic number influences the contrast, but EDS spectra confirmed that the low-transmission area and the surrounding substrate had the same composition.

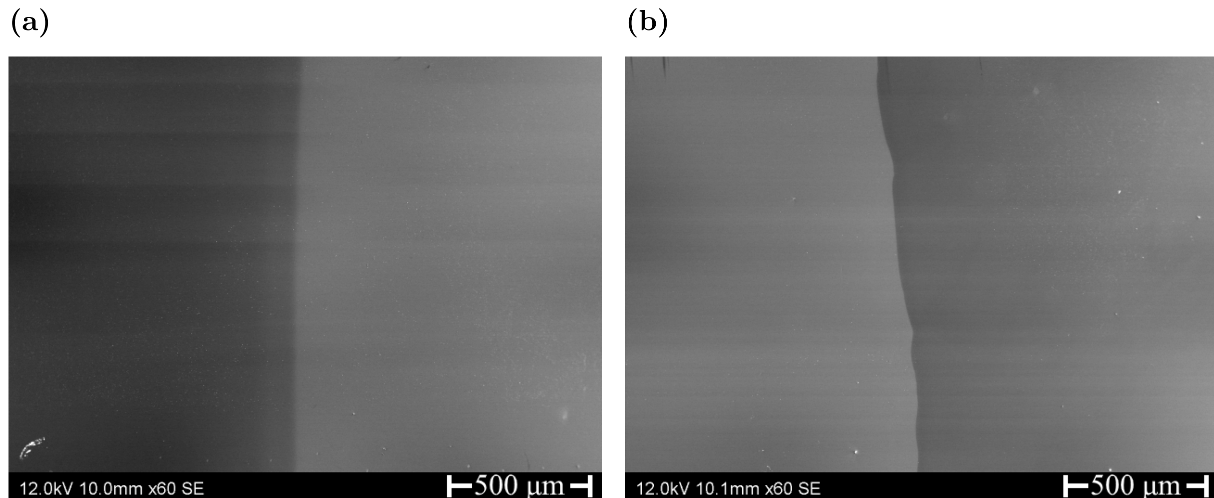

Figure 4.24: SEM image of the (a) left and (b) right edge of the semicircle with low IR transmission in the lower part of substrate B2. The semicircle appears brighter than the rest of the substrate surface.

It could be different crystal orientation that caused the contrast in the SEM images in Fig. 4.24. LPE growth is particularly sensitive for the crystal orientation of the substrate (E. Selvig, personal communication, May 24, 2017). However, the films which were grown on this kind of low-transmission areas were not affected, and hence, it had likely not a different crystal orientation.

Another explanation could be that there was an absorbing layer of some sort on the surface, but as the low-transmission area was present after polishing and an etch had been performed on substrate B2, an absorbing layer was likely not the case. However, this could be investigated further by using a low EDS voltage to get higher surface sensitivity.

Sealy et al. (2000) showed that p-type semiconductors in general appeared brighter and that n-type in general appeared darker than undoped material in SEM. The best contrast was achieved when using low voltage because then the number of electrons that escaped the sample had a stronger dependency on the doping in the sample. Doping contrast agreed with the expected concentration of free carriers for the sloping spectra, which was observed at the low-transmission semicircle.

Near-IR microscopy images of the tellurium precipitate distribution in the CZT substrate can be seen in Fig. 4.25. The images are taken outside the low-transmission area. The observation of Te precipitates contradict the analysis of Yujie et al.. A series of 11 near-IR microscopy images focusing through the complete depth of the substrate was acquired, each image was ∼80 µm deeper into the substrate. The Te precipitate density was rather uniform throughout the bulk of the substrate with an average of 55 Te precipitates in focus per near-IR image. Mainly single Te precipitates, but also some strings of Te precipitates, were observed.

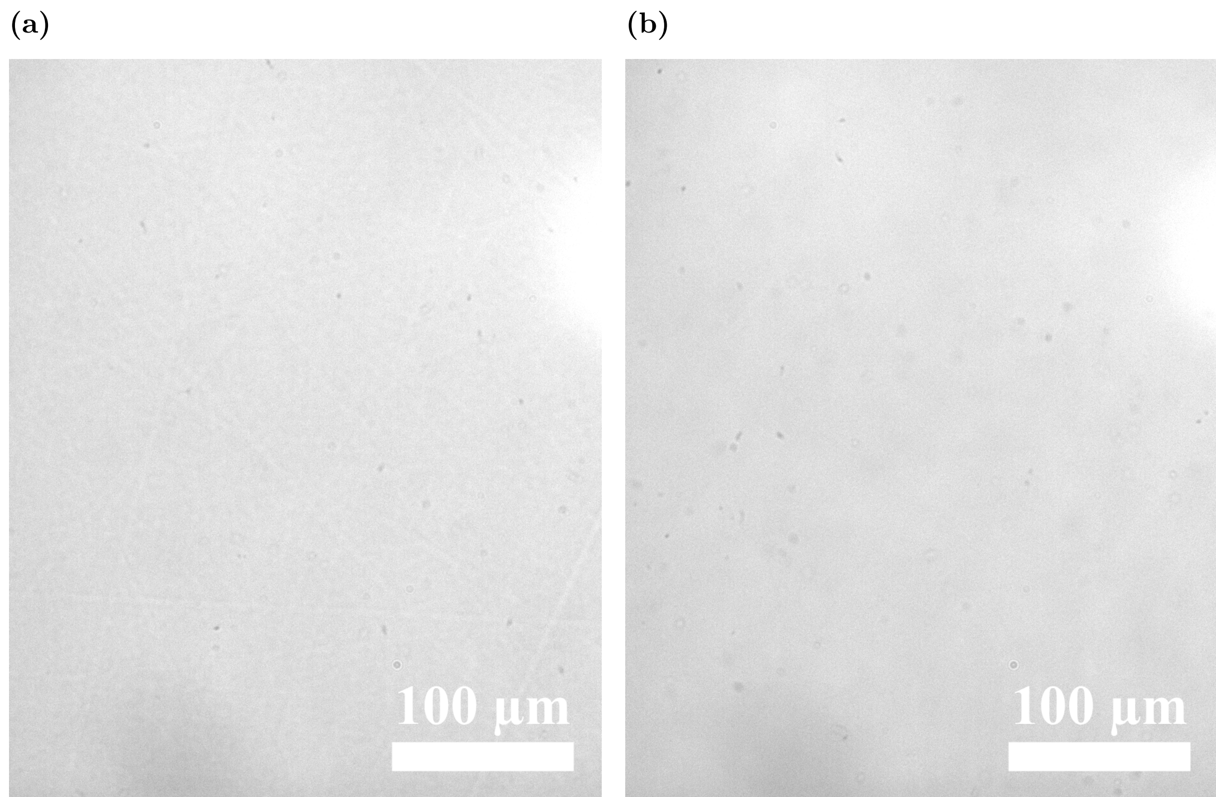

Figure 4.25: Near-IR microscopy images pf Te precipitate density and distribution near the centre of the 30 mm × 30 mm (111)B-oriented substrate B. Image area is 324 µm × 405 µm. (a) The (111)B surface; (b) ∼240 µm below the (111)B surface.

4.3 Surface Analysis of As-Received Substrate C

Substrate C was made by vendor A, but unlike substrate A, it was cut at an angle of 19° with the (111)B-oriented plane to give a (211)B-oriented surface. Interestingly, this substrate looked quite different from as-received substrate A regarding polishing grit particles on the surface.

4.3.1 Particles

Bright and dark field images of the as-received substrate C showed that there were some large particles of size ~300 µm and that there were smaller particles of size 1 µm–15 µm distributed sparsely over the substrate surface with a density of $\sim 3 \cdot 10^{1}\,\mathrm{cm}^{-2}$ close to the edges, see Fig. 4.26.

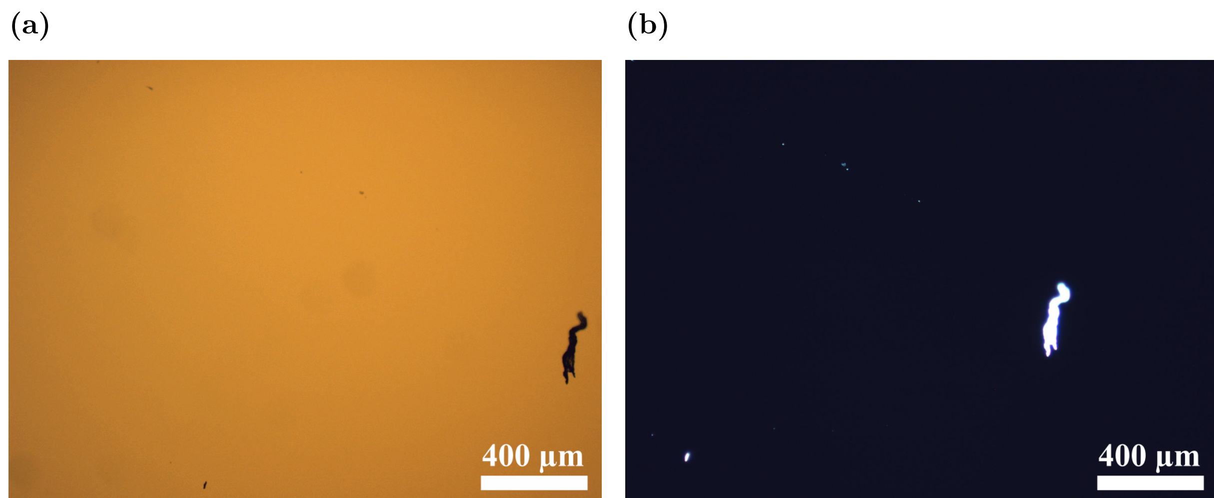

Figure 4.26: Optical microscopy images of as-received substrate C taken at the same location in the upper left corner of the substrate surface: (a) Bright field; and (b) dark field. The same particle configuration can be observed in both images.

4.3.2 Silica (SiO_2) Polishing Grit

SEM images revealed that there are smaller particles with lengths of 30 nm–100 nm on the substrate surface in addition to those observed in optical microscopy. The small particles were distributed over all of the surface. There were some larger agglomerations with size

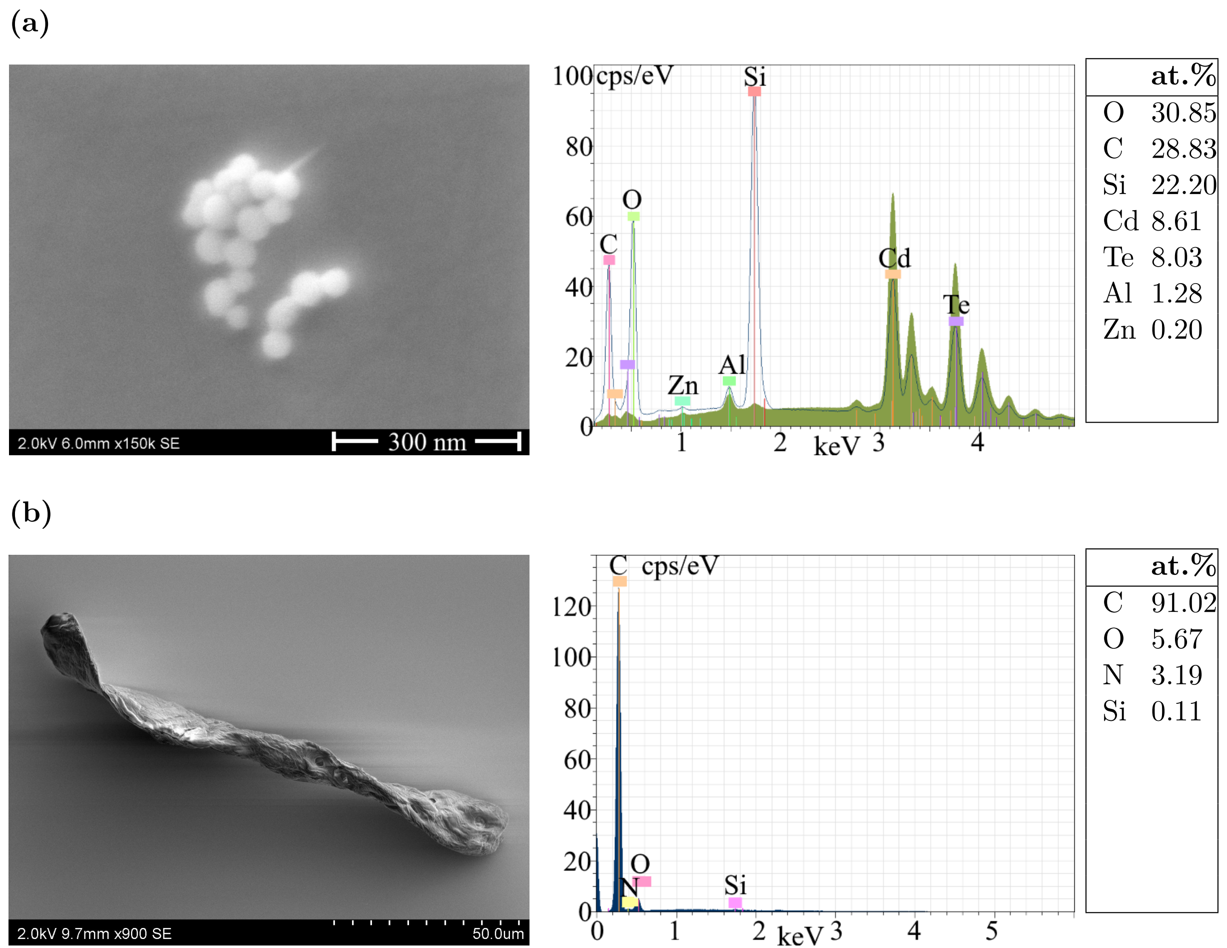

Figure 4.27: High resolution SEM images of two different types of particles found on the as-received substrate C and the corresponding EDS spectra and atomic compositions: (a) silica (SiO_2), the blue spectrum represents the measurements from the particles, while the green spectrum represents the substrate surface next to the particles; and (b) carbon-based particle.

>10 µm towards the edges and corners of the substrate, which was observed in the optical microscopy images as well. A typical area at the centre of substrate C can be seen in Fig. 4.28.

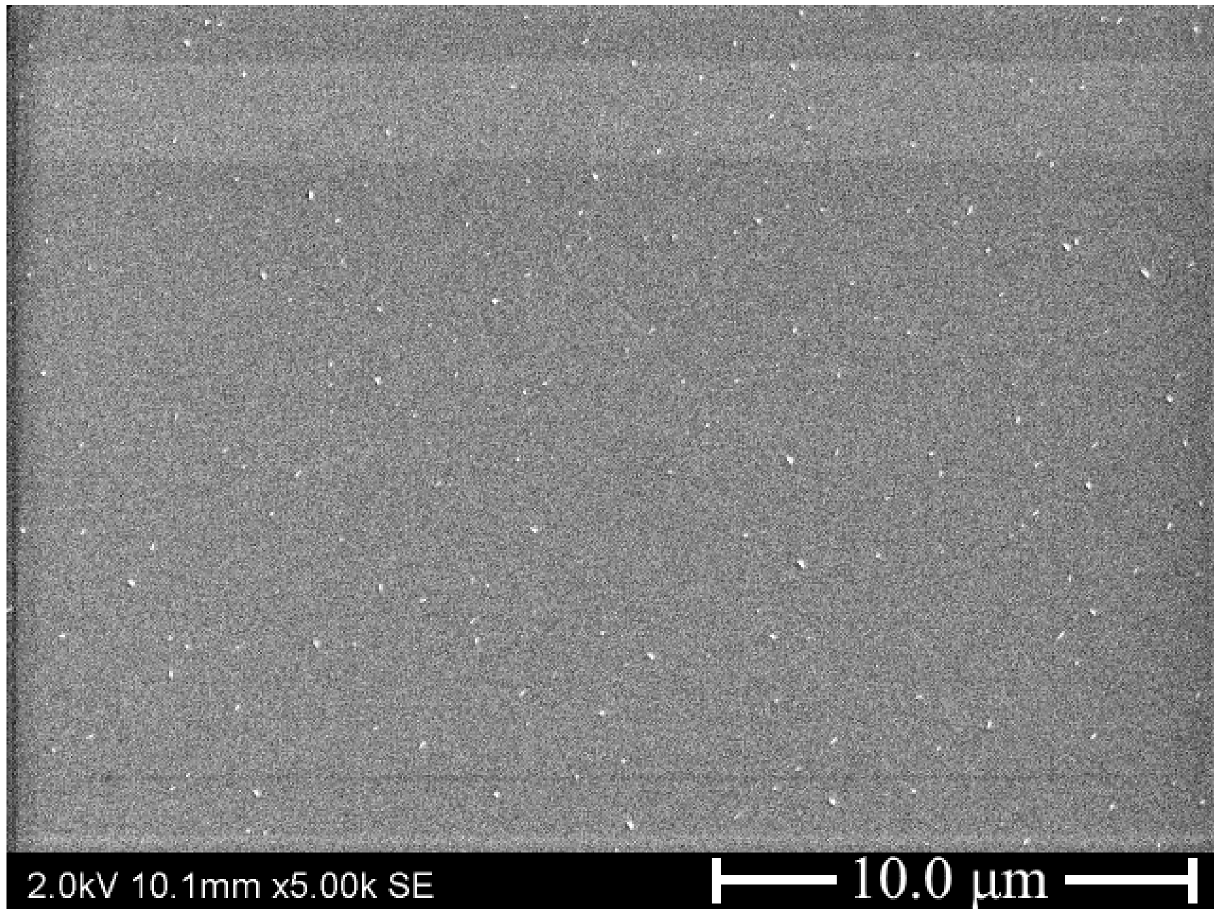

Figure 4.28: SEM image taken near the centre of the as-received substrate C.

An EDS spectrum of an agglomeration of particles with a diameter of 50 nm revealed that the piece was composed of silica oxide, SiO_2, also known as silica, see Fig. 4.27a. As mentioned earlier, the presence of silica can be explained by the frequent use of silica as an abrasive in polishing slurries for semiconducting material. The Al contamination that could be detected in the EDS spectrum obtained from a large area of the substrate can come from residual Al_2O_3 polishing grit, also known as alumina. Due to the small extent of the individual residual particles, it was not possible to get EDS spectra from the particles unless multiple particles formed a larger pile, which was rarely observed.

The polishing grit density was found to be between $1 \cdot 10^6\,\mathrm{cm}^{-2}$ and $5 \cdot 10^7\,\mathrm{cm}^{-2}$. The average particle density was $3 \cdot 10^7\,\mathrm{cm}^{-2}$ with a standard deviation of $1 \cdot 10^7\,\mathrm{cm}^{-2}$. A graphical representation of the particle density at different locations on substrate C can

be seen in Fig. 4.29. This is in agreement with the results of Benson et al. (2015) who found that the silica polishing grit density varied from wafer-to-wafer from $\sim 5 \cdot 10^6\,\mathrm{cm}^{-2}$–$2 \cdot 10^8\,\mathrm{cm}^{-2}$.

The density of polishing grit was at least 1000 times as high as the grit density on the as-received substrate A. It could be the fact that the (211)-oriented surface was not atomically flat, but consisted of (111)-oriented steps, that caused the polishing grit particles to be stuck on the surface.

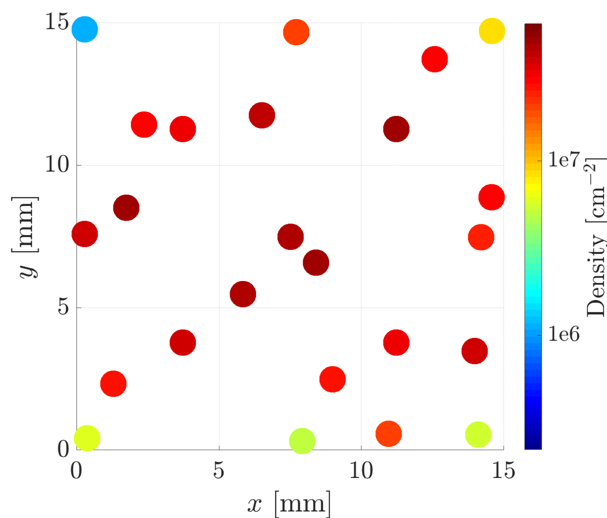

Figure 4.29: A map of the polishing grit density at 24 different locations on the as-received 15 mm × 15 mm substrate C. The density measurements were obtained by counting the number of polishing grits in SEM images covering 25.4 µm × 17.8 µm areas. In total, 0.005 % of the substrate surface was measured. The polishing grit density was observed to vary between $1 \cdot 10^6\,\mathrm{cm}^{-2}$ and $5 \cdot 10^7\,\mathrm{cm}^{-2}$.

4.3.3 Carbon-based Particles

The large particles observed in the dark field images were infrequent with respect to the polishing grit. Only six were observed in the upper half of the substrate, which gave a density of $\sim 3\,\mathrm{cm}^{-2}$. The particles were typically between 100 µm–500 µm long and 20 µm–50 µm wide. The particles appeared darker than the surrounding substrate in the SEM images and the EDS spectra revealed that they were carbon-based, as seen in Fig. 4.27b. As for the carbon-based particles on substrate B, these particles could be residue from mounting wax used during the polishing done by the vendor.

4.3.4 Surface Roughness

The as-received substrate C was characterised for surface topography by AFM. AFM images of the substrate surface are shown in Fig. 4.30. Polishing grit particles can be observed all over the surface of the substrate. The typical polishing grit density on the (211)B-oriented substrate is $\sim 6 \cdot 10^7\,\mathrm{cm}^{-2}$, which is in agreement with the density found from the SEM images. The typical polishing grit length was observed to be between 50 nm–200 nm and the typical height was measured to be about ∼10 nm above the (211)B surface. The small height above the surface compared to the diameter of the particles indicates that the polishing grit particles have penetrated the surface and are partly included in the surface.

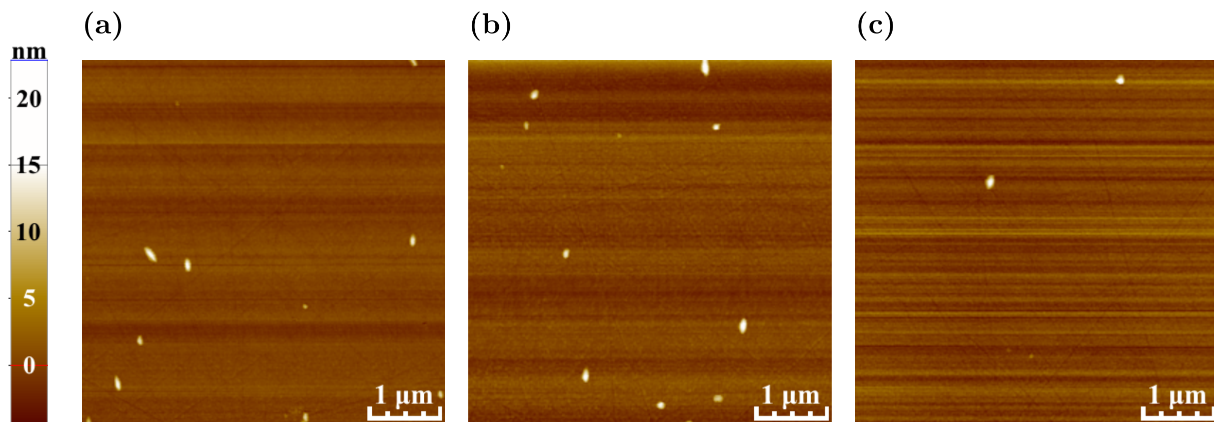

Figure 4.30: AFM measurements of the as-received substrate C. Images of 5 µm×5 µm areas are taken at three different locations on the substrate surface: (a) near the centre, RMS roughness 0.95 nm; (b) near the left edge, RMS roughness 1.4 nm; and (c) near the upper left corner, RMS roughness 1.4 nm.

The RMS roughness was calculated to be 0.95 nm near the centre, 1.4 nm near the edge, and 1.4 nm near the corner, using Eq. 2.15. The polishing grit particles contributed to a higher roughness. To obtain an RMS roughness of the substrate surface which was independent of the polishing grit density, measurements were performed on areas where there was no polishing grit. Several such measurements were performed within the same image. The average of the measurements resulted in an RMS roughness of ∼0.3 nm at the centre and ∼0.5 nm around the edges. Benson et al. (2015) measured a similar RMS roughness of ∼0.4 nm on all the as-received (211)B-oriented CZT substrates they studied. The low RMS roughness indicates an absence of deep scratches. The deepest observed polishing scratches on substrate C were 0.2 µm wide and only 1 nm deep.

Fig. 4.31 show a comparison of an AFM image with a SEM image taken at the same location on the as-received substrate C. The same particle configuration can be seen in both images, but the shape and size of the polishing grit particles observed in AFM were different compared to what were observed in the SEM images. This image artefact in the AFM image can be explained by the convolution effect between the tip and the polishing grit particles, as described in Section 2.6. In other words, due to a too-course tip, an image artefact appeared in the AFM image that made the particles look wider and longer than they really were.

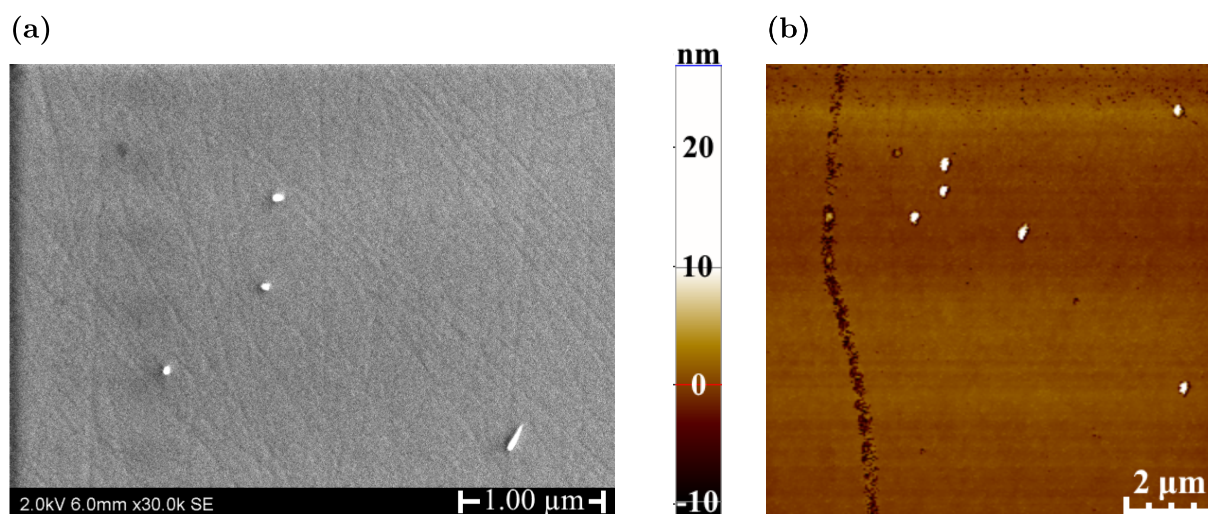

Figure 4.31: Comparison of (a) a SEM image with (b) an AFM image taken at the same location on the as-received substrate C. The height of the features in the AFM image is displayed as colour gradations. The same location with the same particles can be seen in both the AFM image and the SEM image, but due to a too-course tip, an image artefact occur in the AFM image that makes the particles look wider and longer than they are. The advantage of the AFM image is that it gives height information.

4.3.5 Impurity Analysis – EDS

EDS impurity analysis was performed on the as-received substrate C. Three locations on the surface were analysed: near the centre, edge, and corner. The results of this analysis can be seen in Table 4.4. The elements found above the EDS detection limit, in addition to Cd, Zn, and Te, were Al, Si, C, and O. Silicon and oxygen can be accounted for by silica polishing grit. Even though none of the polishing grit agglomerations contained alumina, it could be that some of the single grit that could not be measured using EDS, contained alumina and could account for the detection of aluminium.

Table 4.4: Results of the EDS impurity analysis at three different locations on the 15 mm × 15 mm as-received (211)B CZT substrate C (atomic concentration %). The X-ray signal was acquired from 1270 µm × 890 µm areas near the centre, upper edge, and upper left corner.

	Te (at.%)	**Cd** (at.%)	**Zn** (at.%)	**Al** (at.%)	**Si** (at.%)	**C** (at.%)	**O** (at.%)
Near centre	44.85	44.90	1.44	1.98	0.51	4.93	1.40
Near edge	45.09	45.09	1.49	1.70	0.46	4.93	1.23
Near corner	45.05	45.09	1.44	2.00	0.46	4.83	1.13

4.3.6 IR Characterisation

FTIR transmission spectra were recorded from a 5 × 5 grid on the as-received substrate C. The grid points were placed 2.3 mm from the edge and had 2.6 mm between the closest neighbours. All but five spectra had the same characteristics as substrate A, see Fig. 4.32a, and hence, had the same properties regarding precipitates, carrier concentration, and resistivity as substrate A (Yujie et al., 2004).

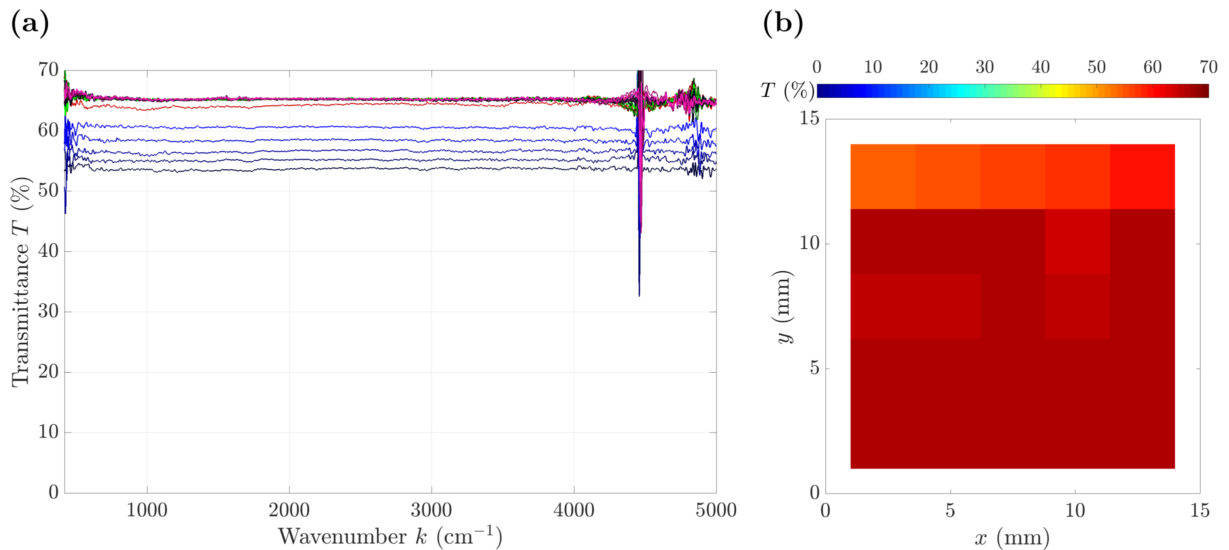

Figure 4.32: FTIR measurements recorded from a 5 × 5 grid on the as-received 15 mm × 15 mm (211)B-oriented substrate C: (a) Transmission spectra; and (b) transmission map at wavenumber $k = 500\,\text{cm}^{-1}$ showing the transmittance T in percentage of incoming light at each grid point. The spikes near $k = 4500\,\text{cm}^{-1}$ and $k = 5000\,\text{cm}^{-1}$ were artefacts of the FTIR instrument.

The five measurements obtained from the upper edge of substrate C had transmittance between 55 % and 61 % in the wavenumber region of interest, which were lower than the rest of the substrate, see Fig. 4.32b. Apart from having lower transmission, the spectra had the same shape and a similar T_{1000}/T_{5000} indicator as the other spectra. For this

reason, and the fact that the lower transmission only occurred at the upper edge, it was believed that the frame that holds the substrate obscure the light at the upper edge, and results in an overall lower transmission for the measurements at the upper edge (E. Selvig, personal communication, May 24, 2017). Taking this into account, the spectra from the upper edge had the same characteristics as the rest.

Near-IR microscopy images of the tellurium precipitate distribution in substrate C can be seen in Fig. 4.33. The observation of Te precipitates contradict the analysis of Yujie et al.. A series of 11 near-IR microscopy images focusing through the complete depth of the substrate was acquired, each image was ∼80 µm deeper into the substrate. The Te precipitate density was rather uniform throughout the bulk of the substrate with an average of 36 Te precipitates in focus per near-IR image. Both single and strings of tellurium precipitates were observed.

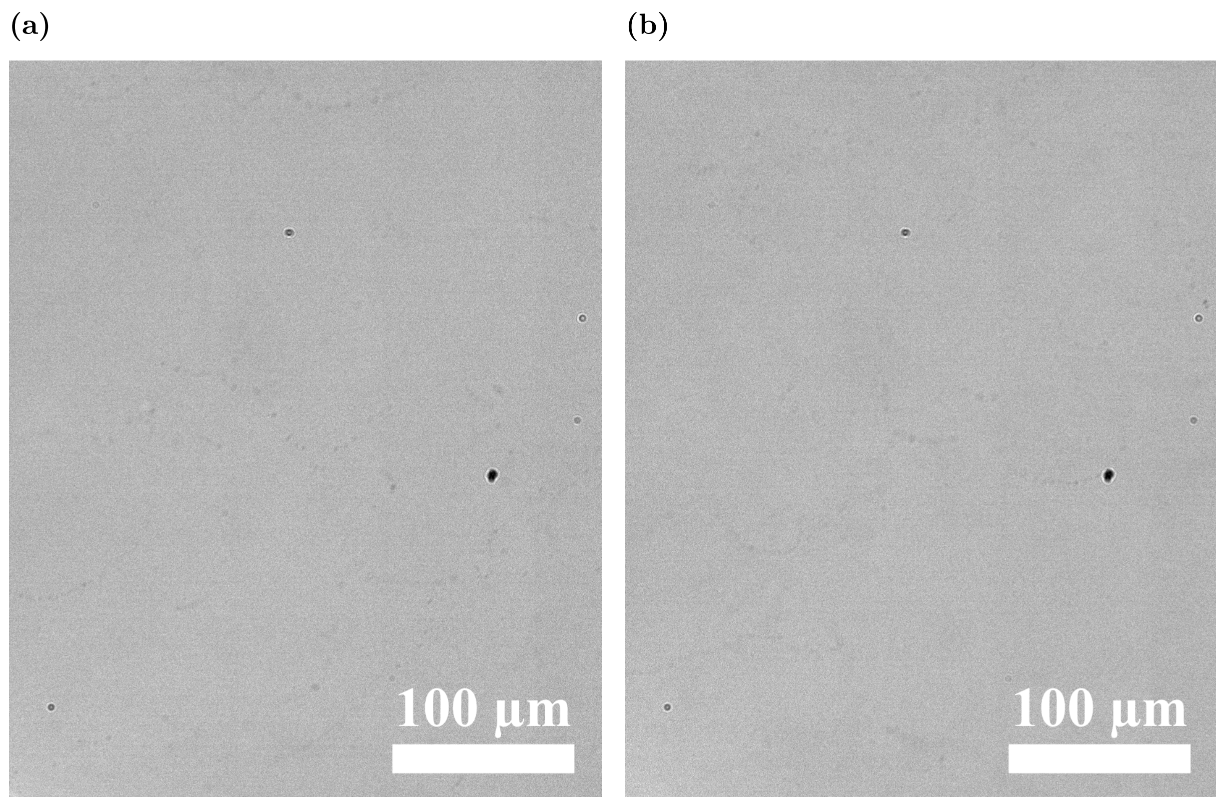

Figure 4.33: Near-IR microscopy images pf Te precipitate density and distribution near the centre of the 15 mm × 15 mm (211)B-oriented substrate C. Image area is 324 µm × 405 µm. (a) The (111)B surface; (b) ∼240 µm below the (111)B surface.

4.4 Surface Analysis of Substrate A after Etching

As substrate A was already polished by the vendor, the surface pre-growth preparation simply consisted of a Br:methanol etch. The dark field images taken of substrate A after etching showed that the etch had left more particles on the surface than before, compare Fig. 4.1 and Fig. 4.34. The density of particles and features larger than 0.5 µm had increased from $\sim 4 \cdot 10^2\,\mathrm{cm}^{-2}$ to $\sim 1 \cdot 10^3\,\mathrm{cm}^{-2}$ close to the centre of the substrate.

Figure 4.34: Dark field optical microscopy image of substrate A after a Br:methanol etch taken near the centre of the substrate.

SEM shows the surface at a higher magnification and it revealed that there were much smaller particles distributed over the surface as well. Whereas it was difficult to focus the SEM beam at the surface of the as-received substrate, after etch this was not a problem due to the higher density of particles. There were a higher density of particles near the edges and corners of the substrate than in the centre, as can be seen in Fig. 4.35a and Fig. 4.35b respectively.

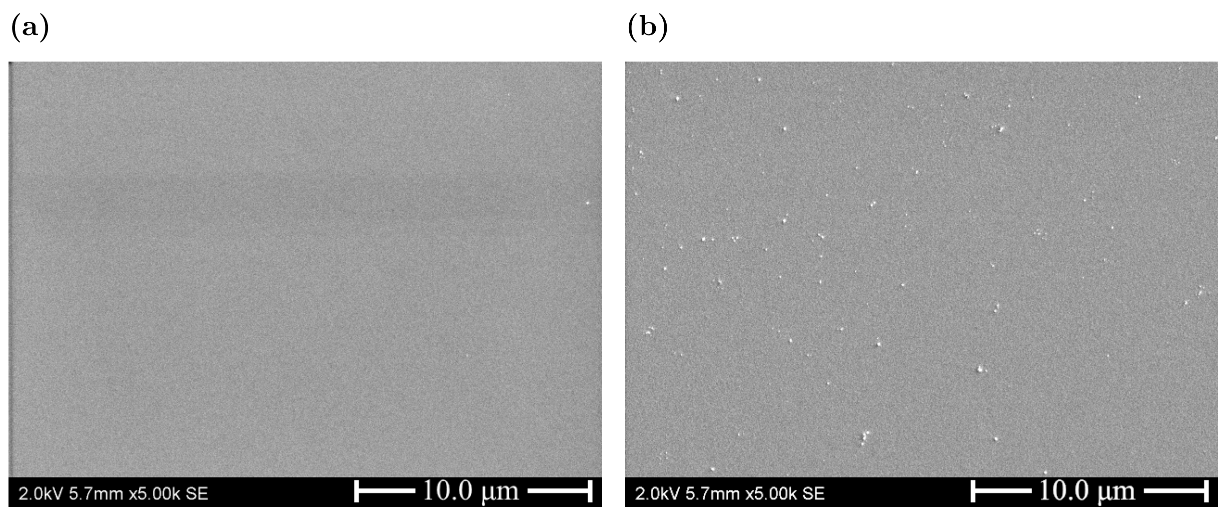

Figure 4.35: SEM images of (a) a typical area near the centre and (b) an area with a high density of particles near the edge of substrate A after a Br:methanol etch.

4.4.1 Particles

Four different types of particles were found on the surface of substrate A after a Br:methanol etch, see Fig. 4.36.

Silica (SiO_2) polishing grit and agglomeration

Silica polishing grit were found on the surface of the substrate after Br:methanol etch, see Fig. 4.36a. The grit density was higher and there were larger agglomerations of grit than before the etch. Silica grit particles are not used at the Epitek laboratory, and hence, it is believed that the source of the particles must be the substrate itself. SEM images of the edge of the as-received substrate A showed that there were a layer of something brighter than the substrate on the bevelled edges, possibly a lot of grit particles, see Fig. 4.37. The polishing grit may have originated from the bevelled edges or from underneath the as-received substrate, and had been distributed over the surface during the preparation etch procedure. There is a slight possibility that the particles came from the beaker where the substrate was etched because the same beaker was used for the polished substrate B, but that is not very likely. The reason the increase in particles after etch has not been detected earlier is that LPE is somewhat forgiving of impurities on the surface as there is a period of surface melting before the film starts to grow. Nevertheless, it will most likely influence the film quality and the bevelled edges and the backside of the substrate have to be studied further in future studies.

The silica polishing grit observed in SEM were found all over the surface. The particle density was found to be between $2 \cdot 10^5\,\mathrm{cm}^{-2}$ and $1 \cdot 10^7\,\mathrm{cm}^{-2}$. The average particle density was $2 \cdot 10^6\,\mathrm{cm}^{-2}$ with a standard deviation of $3 \cdot 10^6\,\mathrm{cm}^{-2}$. This was higher than the grit density before etch by at least a factor of 1000. A graphical representation of the particle density at different locations on substrate A can be seen in Fig. 4.38. There was a tendency of higher density towards the edges and corners.

Fig. 4.36b shows four particles ranging from 4 µm to 15 µm in size. These particles consist of SiO_2. When looking at the particles at higher magnification, see Fig. 4.39, they appeared to be made up of smaller, circular particles with a diameter of 50 nm–100 nm. Clearly, silica polishing grit had accumulated to a larger structure. These structures were mainly observed close to the edges of the substrate and could be originating from the suspected layer of polishing grit on the bevelled edges.

(a)

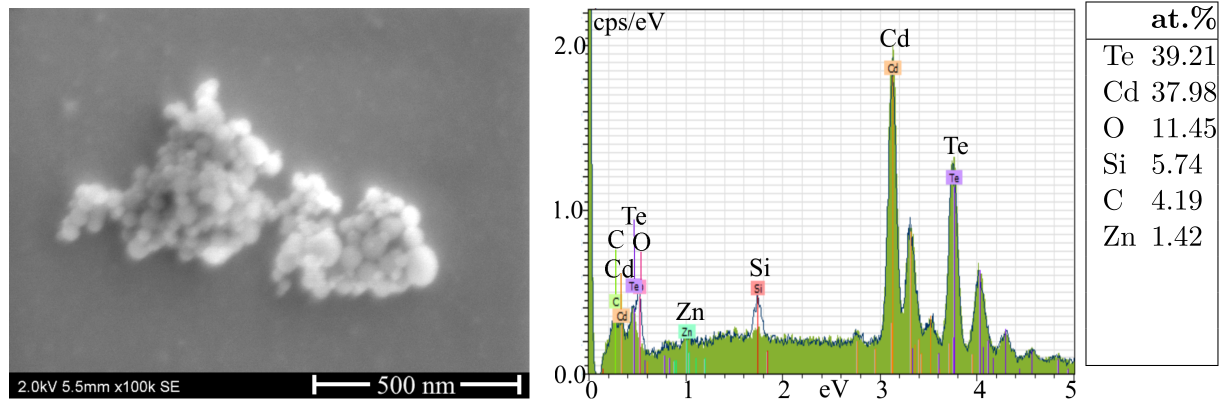

(b)

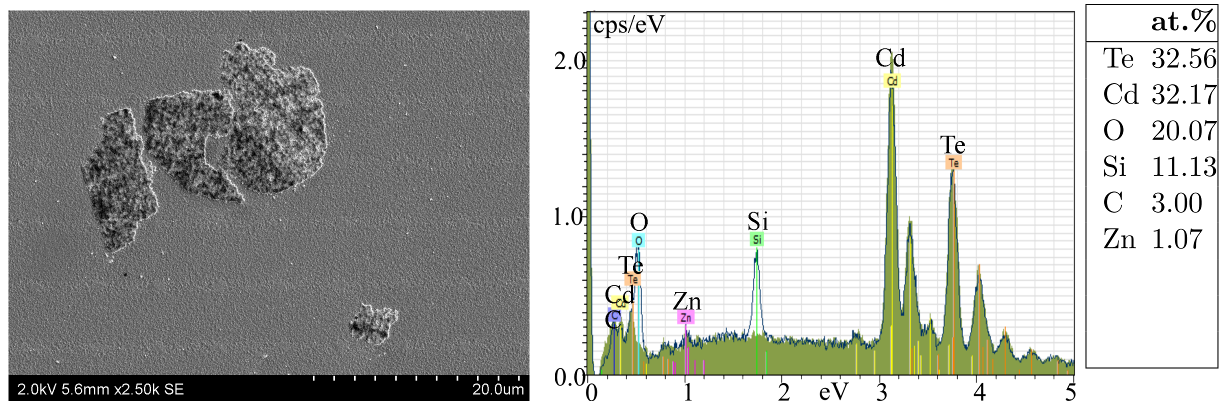

(c)

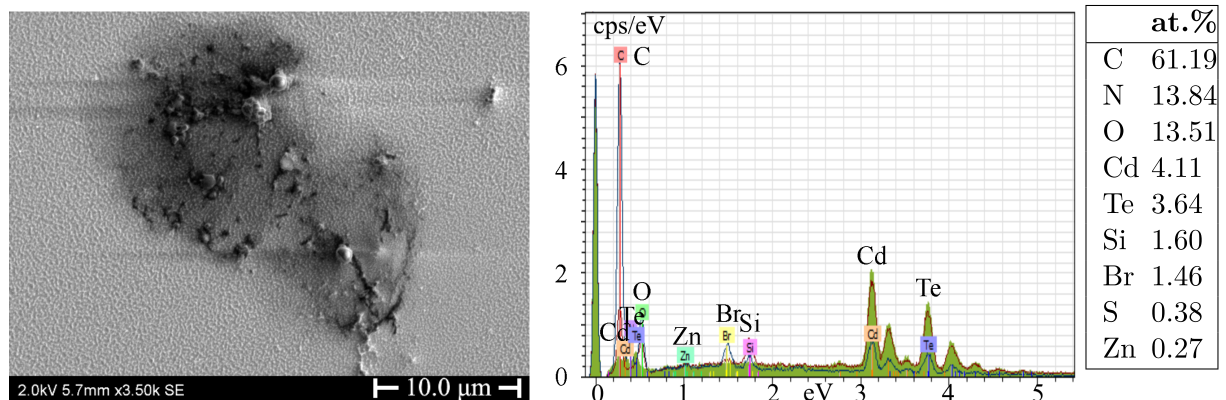

Figure 4.36: High resolution SEM images of four different types of particles and one stain found on substrate A after a Br:methanol etch and the corresponding EDS spectra and atomic compositions: (a) Silica (SiO_2) polishing grit agglomeration; (b) silica (SiO_2) particles; (c) stain consisting of bromine, carbon, and oxygen; and (d) particle consisting of bromine, carbon, and oxygen. The blue line represents the EDS spectrum of the particle, while the filled green represents the EDS spectrum of the underlying substrate.

(d)

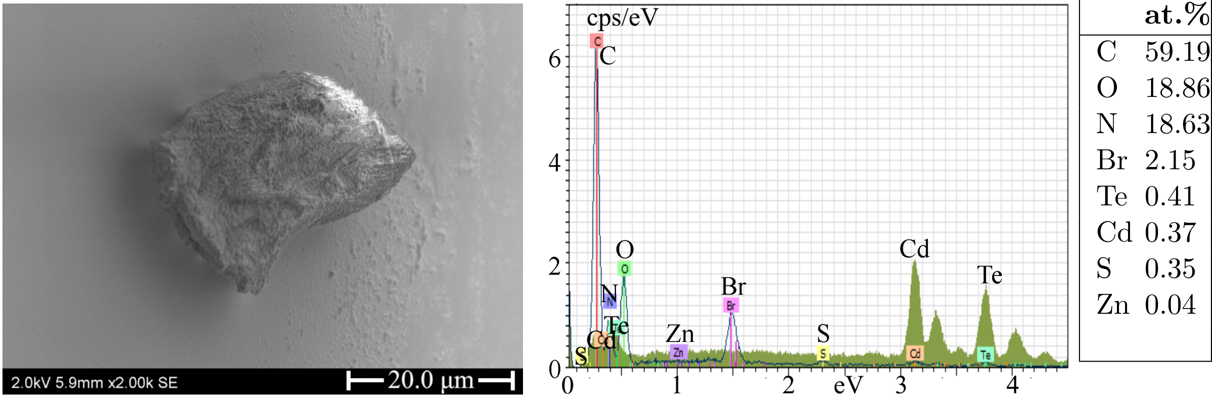

	at.%
C	59.19
O	18.86
N	18.63
Br	2.15
Te	0.41
Cd	0.37
S	0.35
Zn	0.04

Figure 4.36: *(continued)*

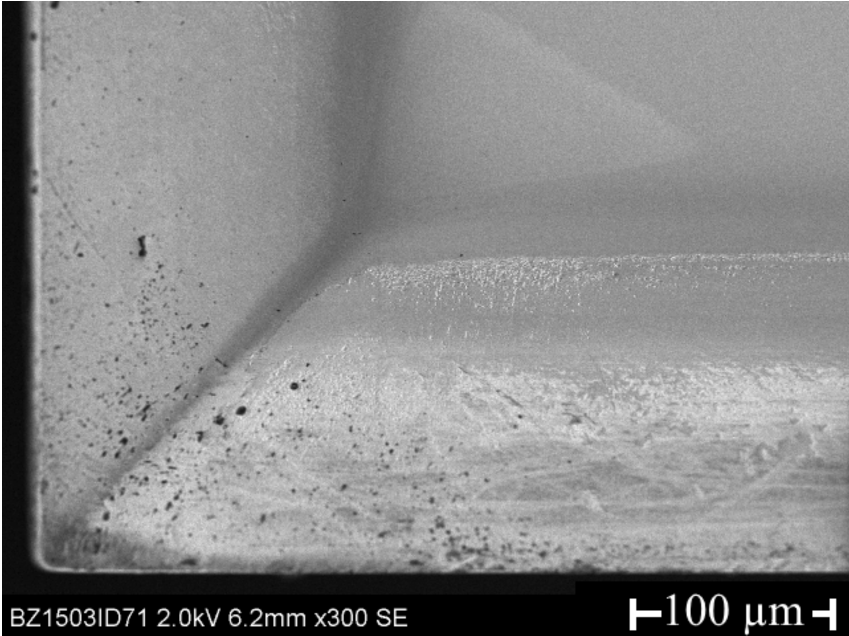

Figure 4.37: SEM image of the corner of the as-received substrate A.

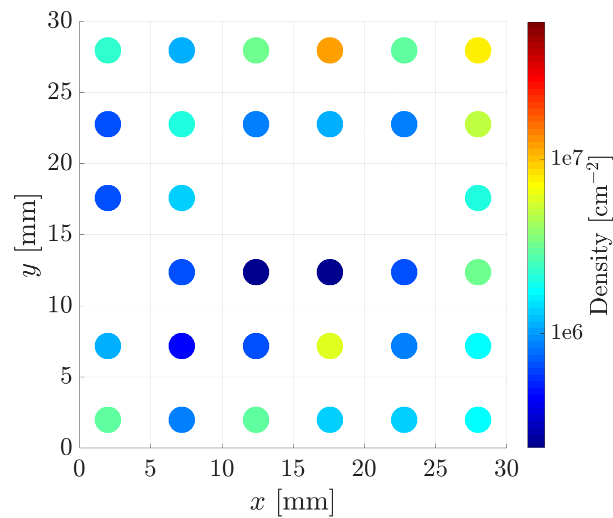

Figure 4.38: A map of the polishing grit density at 36 different locations on the 30 mm × 30 mm substrate A after a Br:methanol etch. The density measurements were obtained by counting the number of polishing grits in SEM images covering 25.4 µm × 17.8 µm areas. In total, 0.002 % of the substrate surface was measured. The polishing grit density was observed to vary between $2 \cdot 10^5\,\mathrm{cm}^{-2}$ and $1 \cdot 10^7\,\mathrm{cm}^{-2}$. The empty grid points represent where the density was less than the detection limit of $2 \cdot 10^5\,\mathrm{cm}^{-2}$.

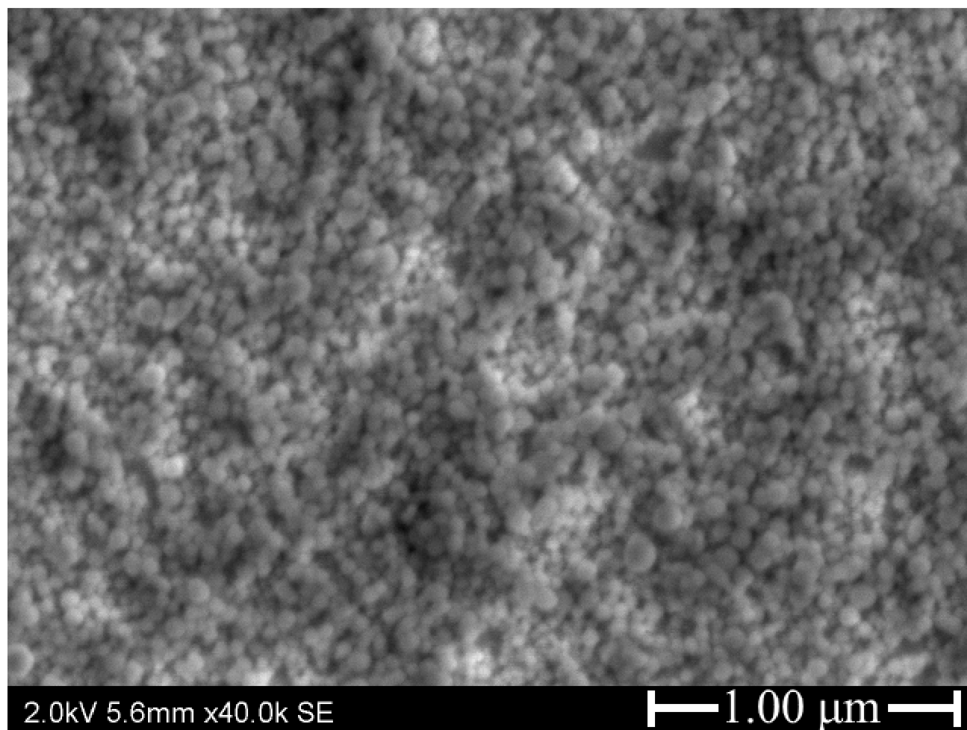

Figure 4.39: SEM image of large agglomeration of particles consisting of silica (SiO_2).

Stain and particle based on bromine, oxygen and carbon

Fig. 4.36c shows a stain that consists of bromine, carbon, and oxygen. This type of stain was mainly observed near the edges of substrate A. The stains were typically ∼10 µm long. Another type of particle showing the same composition in the EDS spectrum as the stain was found around the edges as well, see Fig. 4.36d. This particle was typically 20 µm–30 µm long. The detected carbon could originate from the carbon tab, which were used to mount the substrate to the SEM holder, and the detected bromine was probably residue from the Br:methanol etch.

4.4.2 Surface Roughness

The Br:methanol etched substrate A was characterised for surface topography by AFM. Images of 5 µm × 5 µm areas were taken at three different locations on the surface of the substrate: near the centre, upper edge, and upper left corner, as seen in Fig. 4.40. The RMS roughness was calculated to be 0.51 nm, 1.3 nm, and 1.9 nm, respectively, using Eq. 2.15. This was an increase in roughness by 2 close to the centre, 4 near the edge, and 6 near the corner.

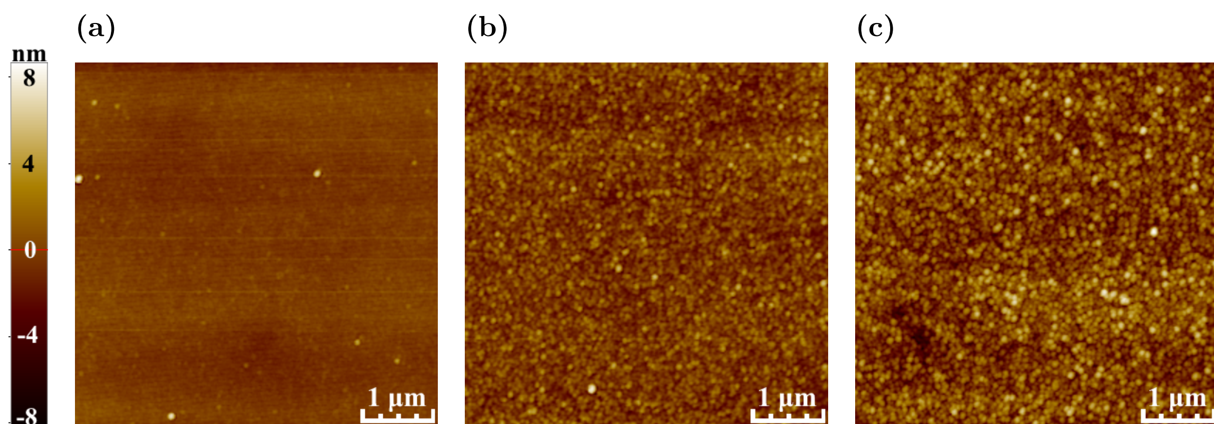

Figure 4.40: AFM measurements of substrate A after a Br:methanol etch. Images of 5 µm × 5 µm areas are taken at three different locations on the substrate surface: (a) near the centre, RMS roughness 0.51 nm; (b) near the upper edge, RMS roughness 1.3 nm; and (c) near the upper left corner, RMS roughness 1.9 nm.

The centre had a flat surface with particles with size between 10 nm–50 nm on top, while the edge and corner had a pebbled surface, which made it difficult to see the presence of particles, as seen in Fig. 4.40b–c. The surface scratches from before the etch had

disappeared, but the presence of polishing particles had increased the roughness of the surface.

4.4.3 Impurity Analysis – EDS

EDS was used to get a quantitative analysis of the chemical composition of substrate A after a Br:methanol etch. The results can be seen in Table 4.5. The same elements as before the etch were identified. The relative concentrations of Cd, Zn, and Te had an error of less than one percentage point from the expected value of 48 at. % cadmium, 2 at. % zinc, and 50 at. % tellurium.

Table 4.5: Results of the EDS impurity analysis at three different locations on the 30 mm × 30 mm (111)B CZT substrate A after a Br:methanol etch (atomic concentration %). The X-ray signal was acquired from 1270 µm × 890 µm areas near the centre, upper edge, and upper left corner.

	Te (at.%)	**Cd** (at.%)	**Zn** (at.%)	**Al** (at.%)	**Si** (at.%)	**C** (at.%)	**O** (at.%)
Near centre	45.42	44.95	1.84	0.22	0.54	6.05	0.97
Near edge	45.41	45.08	1.72	0.25	0.60	6.01	0.95
Near corner	45.18	44.79	1.70	0.56	0.63	6.45	0.70

The atomic concentration of alumina was two times as large close to the corner as it was near the edge and centre of the substrate, which was the case even before etch. In addition, the atomic concentration of oxygen was not high enough to be contributing to Al_2O_3 and SiO_2 for all the detected aluminium and silicon. This could be due to the overlapping peak of the O-Kα and Te-M lines increasing the uncertainty of the elemental quantification. Secondary ion mass spectroscopy (SIMS) measurements, performed on an MCT film grown by LPE on another (111)B-oriented substrate from vendor A, confirmed the presence of silicon and aluminium at the interface between the substrate and the film with peak concentrations of $1 \cdot 10^{19}\,\mathrm{cm}^{-3}$ and $1 \cdot 10^{15}\,\mathrm{cm}^{-3}$ respectively.

4.5 Surface Analysis of Substrate B after fine Polishing and Etching

As substrate B was roughly polished by the vendor, the surface pre-growth preparation consisted of both polishing and a Br:methanol etch. The dark field images of the surface of substrate B after polishing and etching showed that the surface pre-growth preparation had improved the surface considerably, compare Fig. 4.10 and Fig. 4.41a. The previously observed deep surface scratches were removed and there were far less particles and other features on the substrate surface. The density of particle and morphological defects with features >0.5 µm was estimated to be $5 \cdot 10^3\,\mathrm{cm}^{-2}$. In comparison to substrate B, substrate B2 had about the same density of particles larger than 0.5 µm on the surface. The deep surface scratches and large features were removed from substrate B2 as well, see Fig. 4.41b.

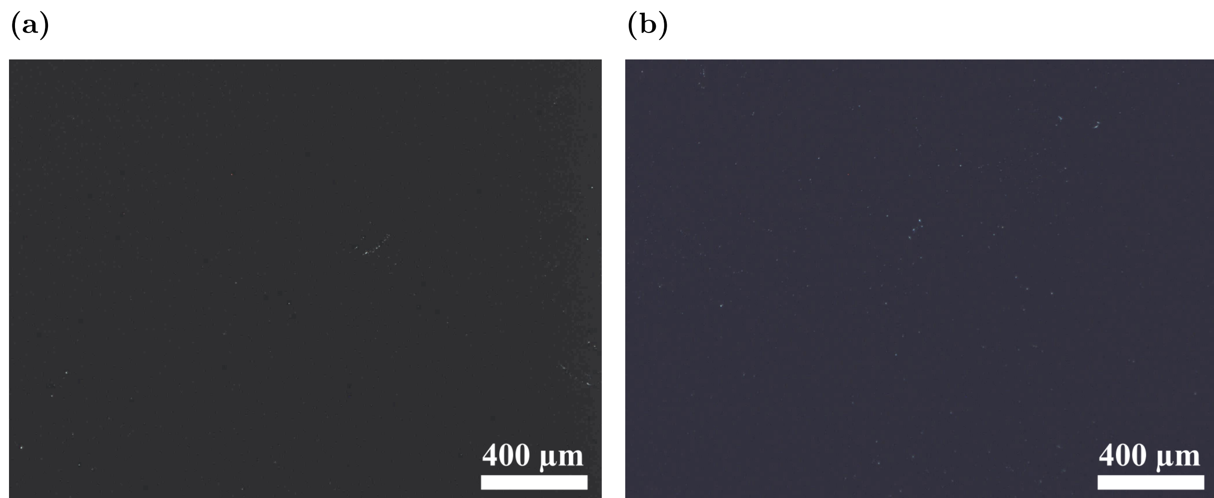

Figure 4.41: Dark field optical microscopy image of (a) the upper left corner of substrate B with surface pre-growth preparation and (b) the centre of substrate B2 with surface pre-growth preparation.

SEM shows the surface at a higher magnification and revealed that there were smaller particles distributed over the surface as well. A typical area in the centre of substrate B and substrate B2 can be seen in Fig. 4.42a and Fig. 4.42b respectively. The particles on both substrates had a length of 20 nm–50 nm.

Four twin boundaries were visible to the naked eye after polish and etch of substrate B. Two in the upper left corner and two that spanned from the lower right corner to the middle of the upper edge, see Fig. 4.43a. An Everson etch was performed, which

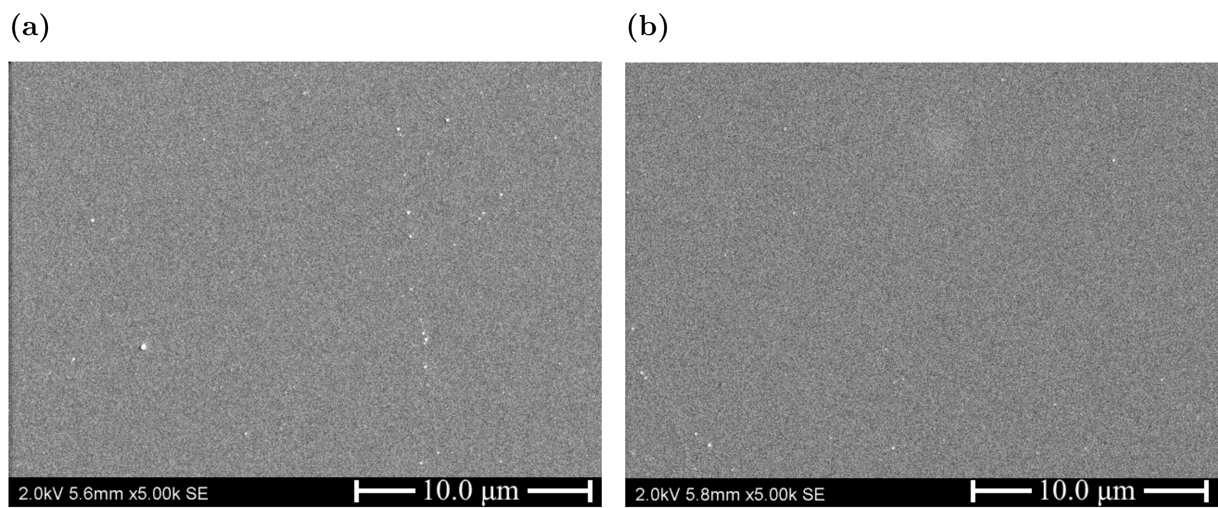

Figure 4.42: SEM images of a typical area near the centre of (a) substrate B and (b) substrate B2 after surface pre-growth preparation.

established that the area between the lines in the upper left corner and between the two other lines were (111)B-oriented, while the surrounding area were twins (Everson et al., 1995). A part of the twin boundary near the upper left corner can be seen in Fig. 4.43b. It formed a piecewise straight line with steps that changed the direction by ±45° every 10 µm–200 µm.

Ashida et al. (2015) studied the dependence of SEM contrast on crystallographic orientation in SiC polytypes. They found that features looked brighter when the direction of the incident electron beam was almost parallel to the topmost stacking sequence direction. However, the formation mechanism of the SEM contrast is still under discussion. This could explain why there was a visible contrast in SEM at the twin boundaries.

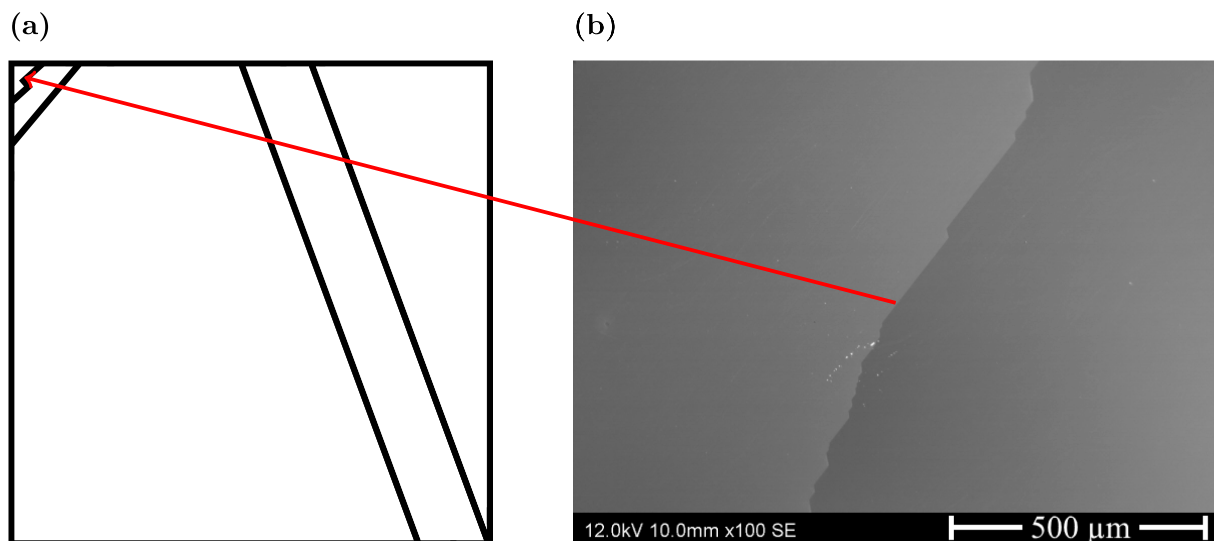

Figure 4.43: (a) Illustration of the location of twin boundaries on substrate B and (b) a SEM image of the twin boundary near the upper left corner.

4.5.1 Particles

Four different types of particles were observed on the surface of substrate B and substrate B2 after surface pre-growth preparation, see Fig. 4.44. They will be described and identified in the following paragraphs.

(a)

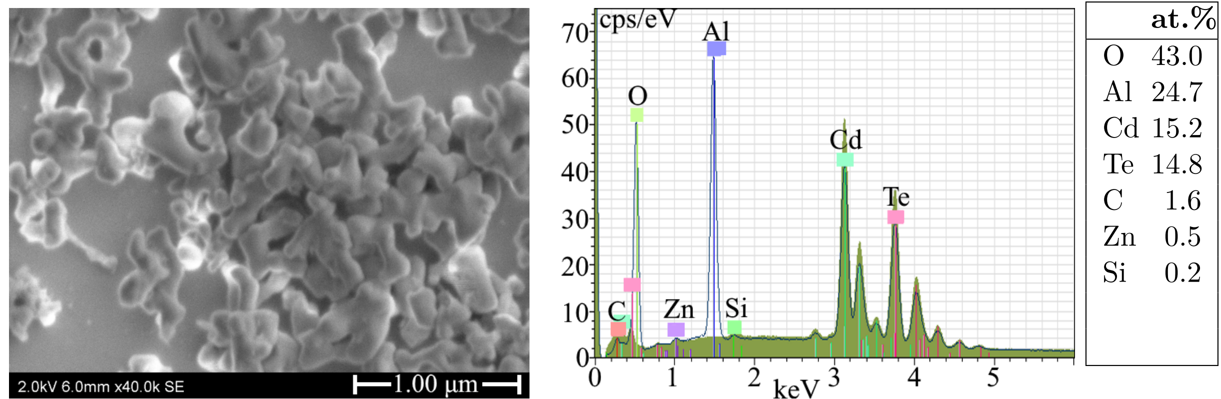

(b)

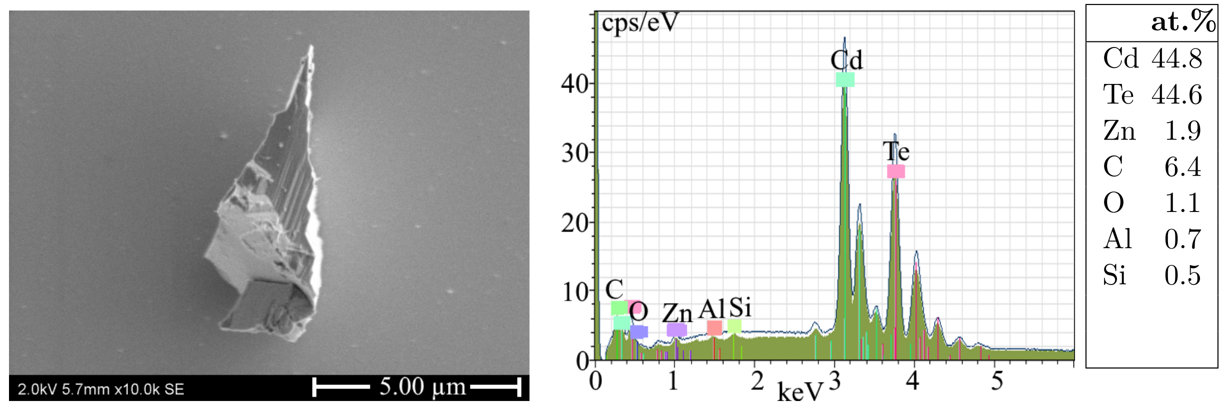

(c)

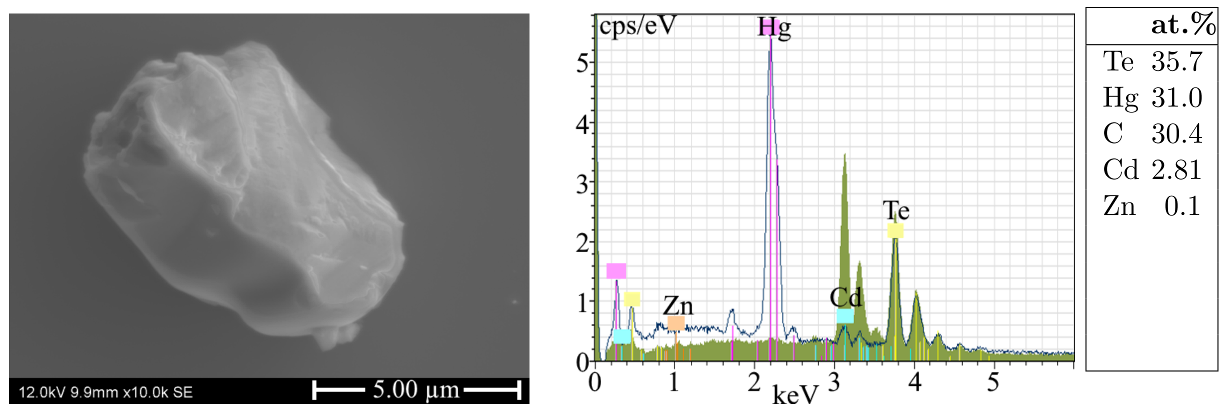

Figure 4.44: High resolution SEM images of four different types of particles found on substrate B and substrate B2 after surface pre-growth preparation and the corresponding EDS spectra and atomic compositions: (a) Alumina (Al_2O_3) polishing grit agglomeration; (b) cadmium zinc telluride ($Cd_{0.96}Zn_{0.04}Te$) particle; (c) mercury telluride (HgTe) particle; and (d) particle based on flouride (F) and carbon (C). The blue spectra represent the particle and the green spectra represent the surrounding substrate.

(d)

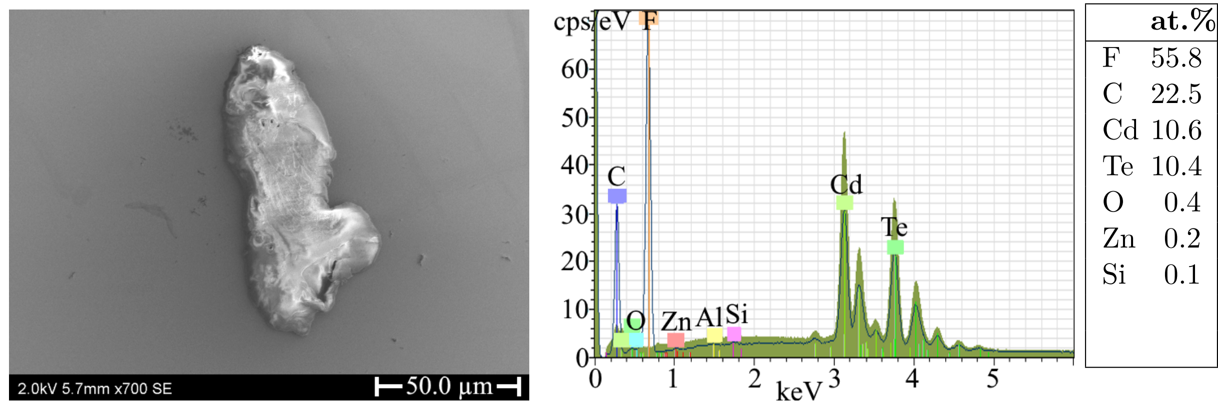

Figure 4.44: *(continued)*

Alumina (Al_2O_3) polishing grit

The small particles observed in SEM were ∼100 nm wide and looked similar to the polishing grit seen on the as-received substrate. EDS confirmed that they too consisted of alumina. The grit was distributed over the surface with a tendency of higher density towards the upper right, lower right, and lower left corners.

The particle density on substrate B was found to be between $2 \cdot 10^6\,\mathrm{cm}^{-2}$ and $2 \cdot 10^7\,\mathrm{cm}^{-2}$. The average particle density was $7 \cdot 10^6\,\mathrm{cm}^{-2}$, with a standard deviation of $4 \cdot 10^6\,\mathrm{cm}^{-2}$. Substrate B2 had a similar distribution of polishing grit. There were higher densities of particles near the left and upper edges. The particle density was found to be between $2 \cdot 10^6\,\mathrm{cm}^{-2}$ and $6 \cdot 10^7\,\mathrm{cm}^{-2}$. The average particle density was $1 \cdot 10^7\,\mathrm{cm}^{-2}$, with a standard deviation of $1 \cdot 10^7\,\mathrm{cm}^{-2}$. A graphical representation of the particle density at different locations on substrate B and substrate B2 can be seen in Fig. 4.45a and Fig. 4.45b respectively.

CdZnTe, HgTe, and C_2F_5 particles

Some larger particles 5 µm–50 µm long were observed near the edges of the etched substrate. The particles with sharp edges consisted of $Cd_{0.96}Zn_{0.04}Te$, see Fig. 4.44b. These were likely residual polishing debris from the surface preparation. Also some HgTe particles were observed, see Fig. 4.44c. These could have settled on the surface during etching of the substrate due to contamination in the beaker. The largest particles with size of to 50 µm consisted of C_2F_5 and looked similar to the previously observed carbon-based par-

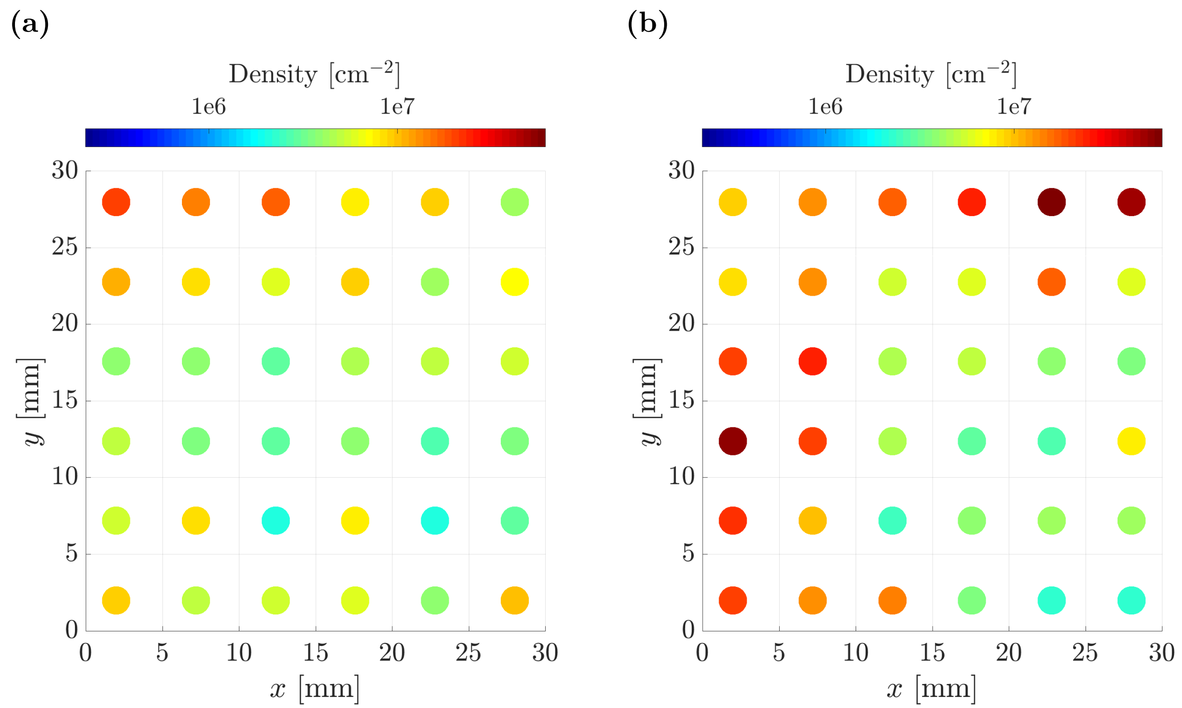

Figure 4.45: Maps of the polishing grit density on the 30 mm × 30 mm substrates B and B2 after surface pre-growth preparation: (a) 36 different locations on substrate B where the polishing grit density varied between $2 \cdot 10^6\,\text{cm}^{-2}$ and $2 \cdot 10^7\,\text{cm}^{-2}$; and (b) 36 different locations on substrate B2 where the polishing grit density varied between $2 \cdot 10^6\,\text{cm}^{-2}$ and $6 \cdot 10^7\,\text{cm}^{-2}$. The density measurements were obtained by counting the number of polishing grits in SEM images covering 25.4 µm × 17.8 µm areas. In total, 0.002 % of the substrate surfaces were measured.

ticles on the as-received substrate, see Fig. 4.44d. It was a mystery where these particles came from.

4.5.2 Surface Roughness

The polished and Br:methanol etched substrates B and B2 were characterised for surface topography by AFM. Images of 5 µm × 5 µm areas were taken at three different locations on the surface of the substrate: near the centre, upper edge, and upper left corner, as seen in Fig. 4.46. The RMS roughness was calculated to be 0.85 nm, 0.76 nm, and 0.92 nm, respectively for substrate B. While substrate B2 had RMS roughness of 0.91 nm, 0.96 nm, and 1.3 nm, respectively. This was a decrease in roughness by 4. The surface scratches from before the etch had disappeared.

4.5.3 Impurity Analysis – EDS

EDS was used to get a quantitative analysis of the chemical composition of substrates B and B2 after polishing and a Br:methanol etch. The results can be seen in Table 4.6. The same elements as before the etch were identified. The relative concentrations of Cd, Zn, and Te had an error of less than one percentage point from the expected value of 48 at. % cadmium, 2 at. % zinc, and 50 at. % tellurium. The about twice as large concentration of oxygen in substrate B2 in comparison to substrate B was probably due to substrate B2 being in air for a longer time than substrate B before being inserted into the SEM chamber.

Table 4.6: Results of the EDS impurity analysis at three different locations on the 30 mm × 30 mm (111)B CZT substrates B and B2 after polishing and a Br:methanol etch (atomic concentration %). The X-ray signal was acquired from 1270 µm × 890 µm areas near the centre, upper edge, and upper left corner.

		Te (at.%)	**Cd** (at.%)	**Zn** (at.%)	**Al** (at.%)	**Si** (at.%)	**C** (at.%)	**O** (at.%)
B	Near centre	46.10	45.35	1.92	0.23	0.52	5.49	0.40
	Near edge	45.49	45.12	2.02	0.26	0.49	5.99	0.64
	Near corner	45.83	45.34	1.92	0.60	0.50	5.34	0.47
B2	Near centre	45.23	45.11	1.88	0.31	0.53	6.01	0.94
	Near edge	45.41	45.20	1.71	0.25	0.51	6.09	0.82
	Near corner	44.93	44.88	1.68	0.68	0.51	6.31	1.02

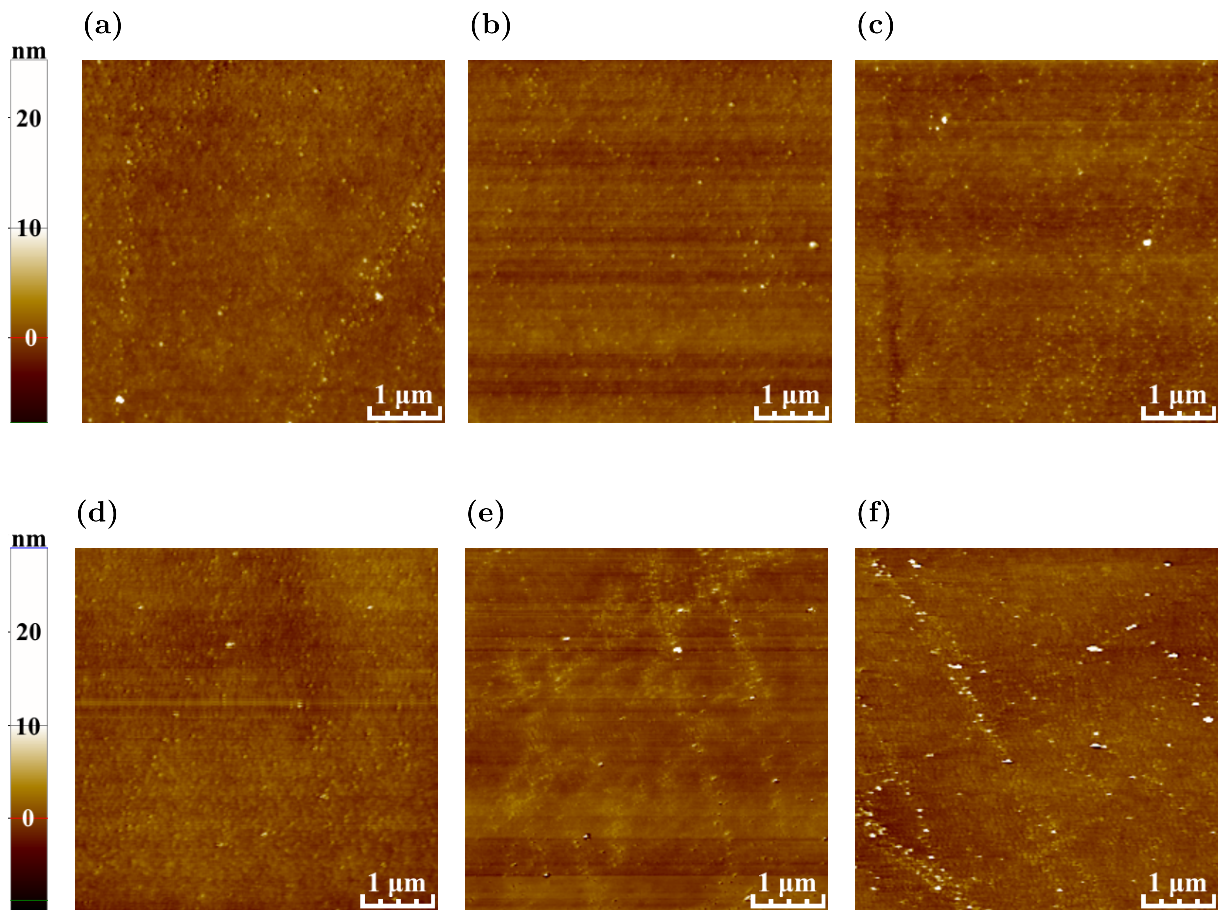

Figure 4.46: AFM measurements of substrate B and substrate B2 after polishing and a Br:methanol etch. Images of 5 µm × 5 µm areas are taken at three different locations on the substrate surfaces. For substrate B: (a) near the centre, RMS roughness 0.85 nm; (b) near the left edge, RMS roughness 0.76 nm; and (c) near the upper left corner, RMS roughness 0.92 nm. For substrate B2: (d) near the centre, RMS roughness 0.91 nm; (e) near the upper edge, RMS roughness 0.96 nm; and (f) near the upper left corner, RMS roughness 1.3 nm.

The atomic concentration of aluminium and silicon was about the same before and after polishing and etching of the substrate. SIMS measurements, performed on an MCT film grown by LPE on another (111)B-oriented substrate from vendor A, confirmed the presence of silicon and aluminium at the interface between the substrate and the film with peak concentrations of $7 \cdot 10^{16}\,\mathrm{cm}^{-3}$ and $5 \cdot 10^{16}\,\mathrm{cm}^{-3}$ respectively.

4.6 Surface Analysis of Substrate C after Etching

As substrate C was already polished by the vendor, the surface pre-growth preparation simply consisted of a Br:methanol etch. The ultimate goal for the MBE preparation etch was to provide a clean, smooth, and well-ordered surface to minimise growth defects. As can be seen in Fig. 4.47, there were many features larger than 0.5 µm on the surface after the etch. The density of those features was $\sim 8 \cdot 10^3\,\mathrm{cm}^{-1}$.

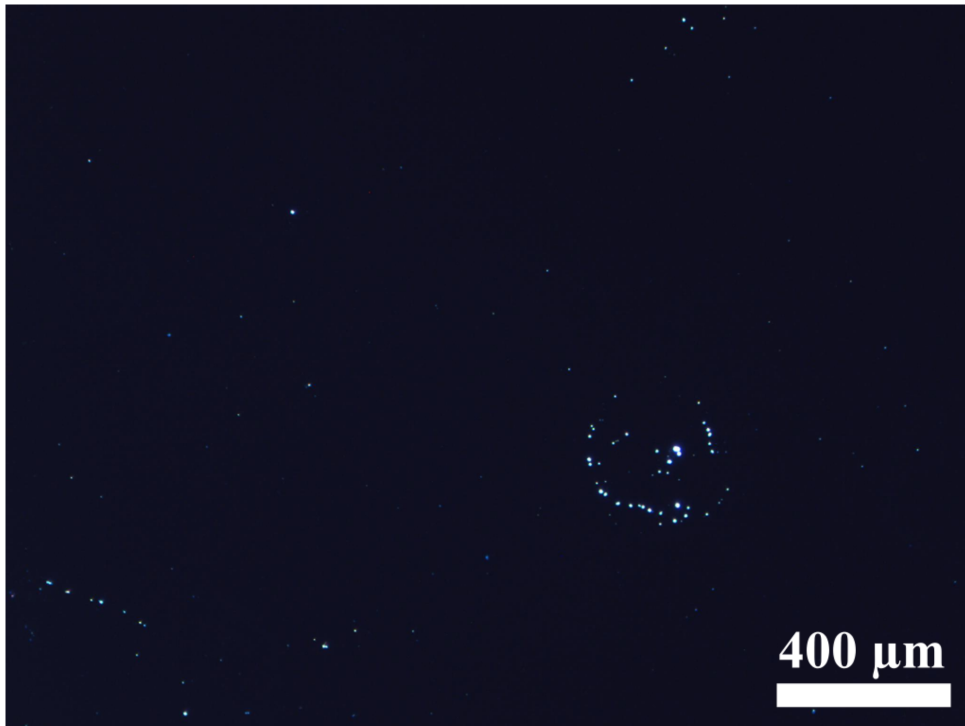

Figure 4.47: Dark field optical microscopy image of substrate C after Br:methanol etch taken near the centre of the substrate.

SEM displayed the surface at a higher magnification and it revealed that there were smaller particles distributed over the surface as well. A typical area near the centre of the substrate can be seen in Fig. 4.48a. There were observed more particles close to the edge of the substrate, as seen in Fig. 4.48b.

4.6.1 Particles

Four different types of particles were found and identified on the surface of the Br:methanol etched substrate C, as seen in Fig. 4.49.

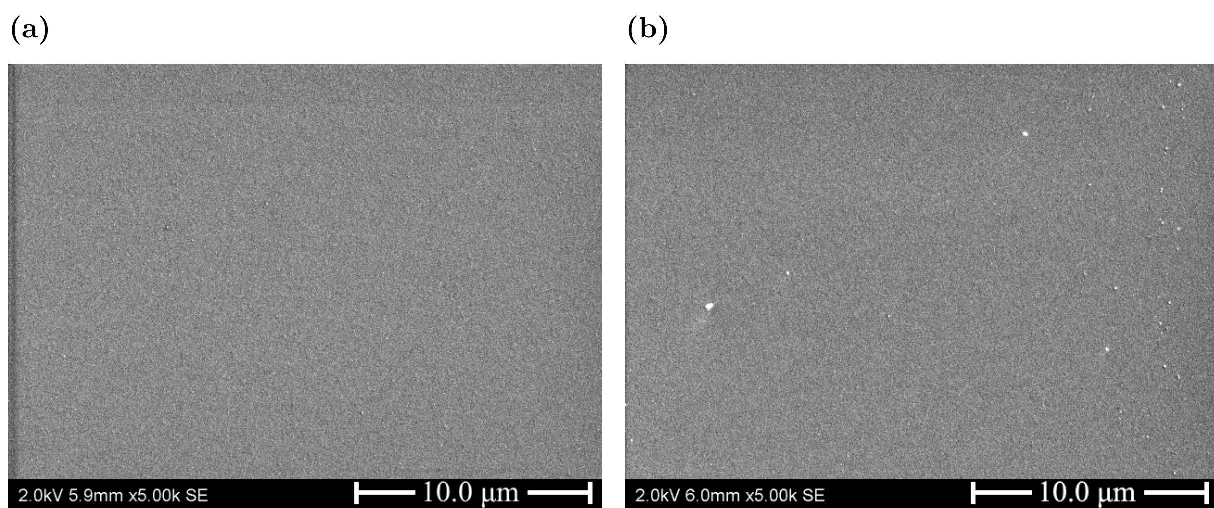

Figure 4.48: SEM images of (a) a typical area near the centre and (b) an area with a high density of particles near the edge of substrate C after surface pre-growth preparation.

(a)

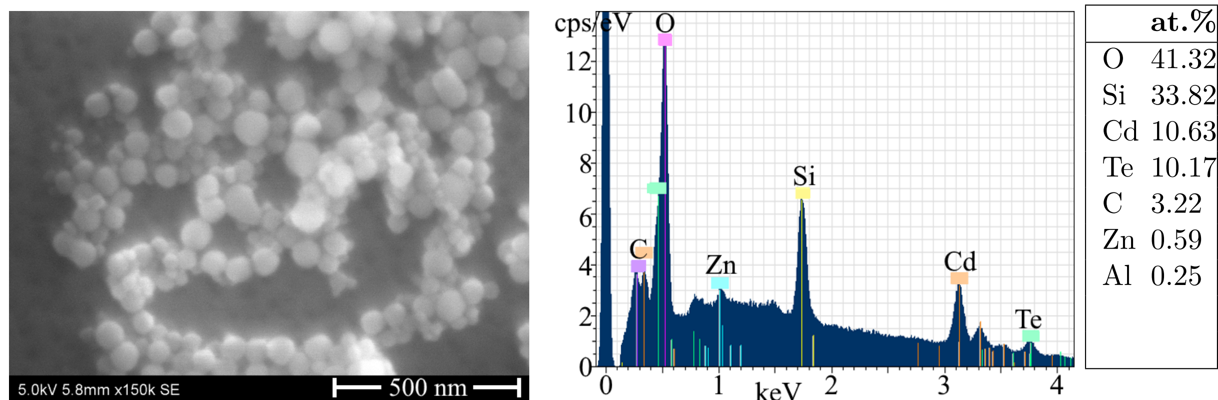

(b)

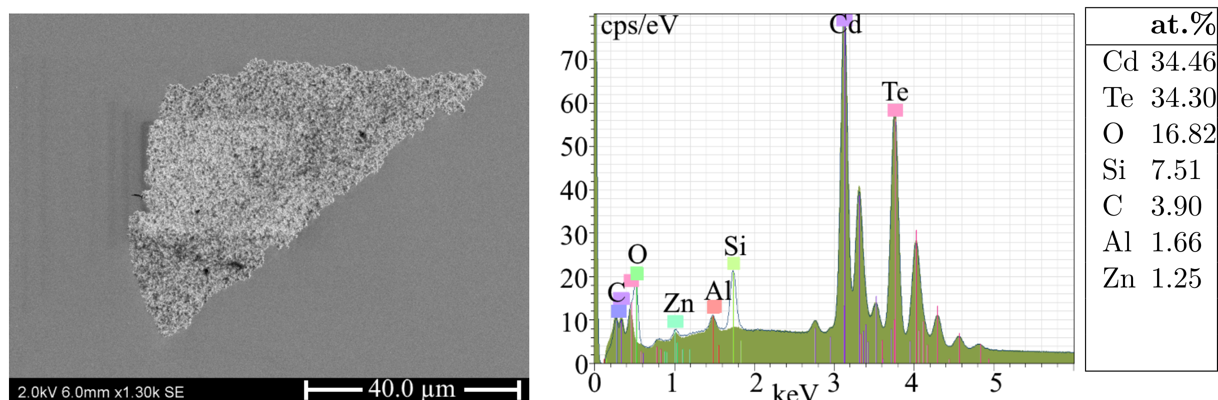

(c)

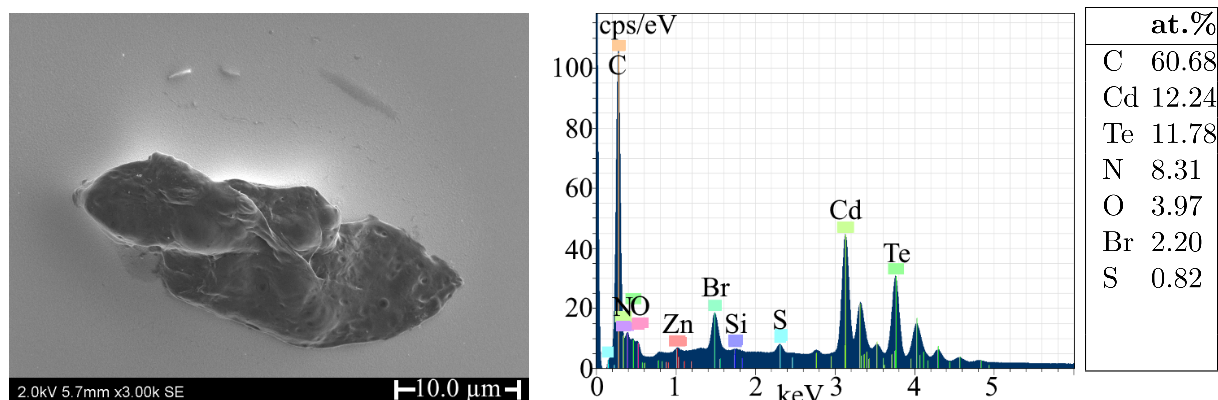

Figure 4.49: High resolution SEM images of two different types of particles found on substrate C after surface pre-growth preparation and the corresponding EDS spectra and atomic compositions: (a) Silica (SiO_2) polishing grit; (b) large silica agglomeration; and (c)–(d) carbon-based particles.

(d)

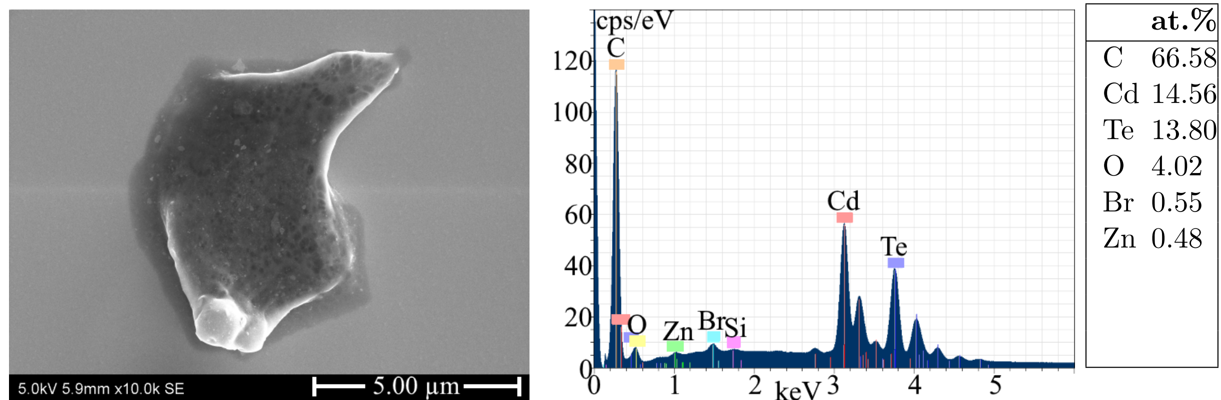

	at.%
C	66.58
Cd	14.56
Te	13.80
O	4.02
Br	0.55
Zn	0.48

Figure 4.49: *(continued)*

Silica (SiO_2) polishing grit and agglomerations

Silica polishing grit were found on the surface of the substrate after Br:methanol etch, see Fig. 4.49a. However, the polishing grit density was lower than before the etch. The silica polishing grit were found all over the surface with a tendency of higher density towards the upper right, lower right, and lower left corners. The particle density was found to be between $2 \cdot 10^5\,\mathrm{cm}^{-2}$ and $1 \cdot 10^7\,\mathrm{cm}^{-2}$. The average particle density was $3 \cdot 10^6\,\mathrm{cm}^{-2}$, with a standard deviation of $3 \cdot 10^6\,\mathrm{cm}^{-2}$. The polishing grit density was reduced by a factor 10 compared to the average density before etch. A graphical representation of the particle density at 25 different locations on substrate C can be seen in Fig. 4.50.

The sample Pearson correlation coefficient demonstrated that there was a weak negative correlation of -0.3 between the density of polishing grit on the as-received substrate C and the density of polishing grit after surface pre-growth preparation. This was not enough to claim that the density before and after preparation was correlated.

Some large silica agglomerations with size ranging up to 50 µm were observed near the edges of substrate C, see Fig. 4.49b. As the EDS spectrum had CZT as the major contributor to the signal, this indicates that the grit particles form a thin layer on the surface. The silica particles from the as-received substrate could have been redistributed over the surface by the etch solution and at the same time collected into larger agglomerations.

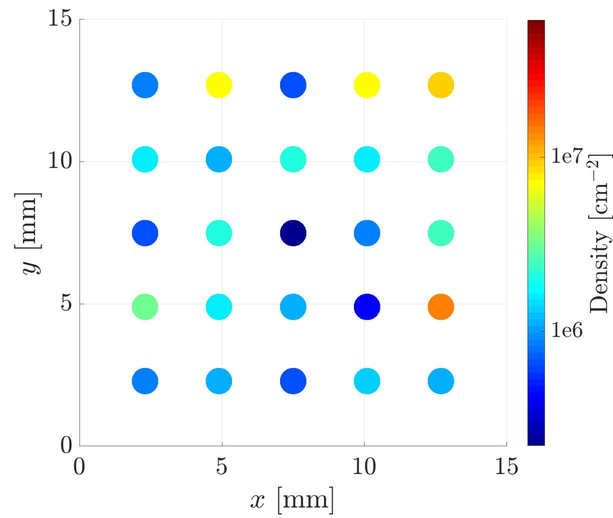

Figure 4.50: A map of the polishing grit density at 25 different locations on the 15 mm × 15 mm substrate C after surface pre-growth preparation. The density measurements were obtained by counting the number of polishing grits in SEM images covering 25.4 µm × 17.8 µm areas. In total, 0.005 % of the substrate surface was measured. The polishing grit density was observed to vary between $2 \cdot 10^5\,\mathrm{cm}^{-2}$ and $1 \cdot 10^7\,\mathrm{cm}^{-2}$.

Carbon-based particles

In addition to the polishing grit, some larger particles with size 5 µm–10 µm was observed on the surface, as seen in Fig. 4.49c and Fig. 4.49d. The particles consisted mainly of carbon and could be the same carbon-based particles from before the etch. The signal from nitrogen was also present before etch, but the bromine would come from the Br:methanol etch and had possibly sticked to the carbon-based particle.

4.6.2 Surface Roughness

The Br:methanol etched substrate C was characterised for surface topography by AFM. Images of 5 µm × 5 µm areas were taken at three different locations on the substrate surface: near the centre, upper edge, and upper left corner, as seen in Fig. 4.51. The RMS roughness was calculated to be 1.4 nm, 1.4 nm, and 2.8 nm, respectively, using Eq. 2.15. The roughness had increased by 50 % near the centre, indifferent at the edge, and increased by a factor 2 near the corner compared to the substrate before etch.

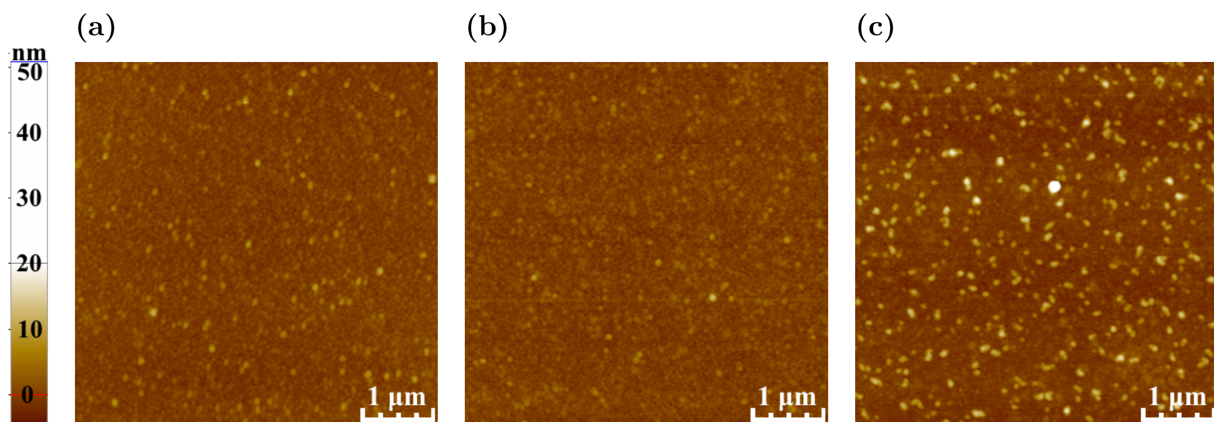

Figure 4.51: AFM measurements of substrate C with surface pre-growth preparation. Images of 5 µm × 5 µm areas are taken at three different locations on the substrate surface: (a) near the centre, RMS roughness 1.4 nm; (b) near the upper edge, RMS roughness 1.4 nm; and (c) near the upper left corner, RMS roughness 2.8 nm.

4.6.3 Impurity Analysis – EDS

EDS was used to get a quantitative analysis of the chemical composition of substrate C after a Br:methanol etch. The results can be seen in Table 4.7. The same elements were

identified as before the etch: Te, Cd, Zn, Al, Si, C, and O. The atomic concentration of Si was the same as before the etch, which was surprising as the polishing grit density was reduced by a factor of 10.

Table 4.7: Results of the EDS impurity analysis at three different locations on the 15 mm × 15 mm (211)B CZT substrate C after a Br:methanol etch (atomic concentration %). The X-ray signal was acquired from 1270 µm × 890 µm areas near the centre, upper edge, and upper left corner.

	Te (at.%)	**Cd** (at.%)	**Zn** (at.%)	**Al** (at.%)	**Si** (at.%)	**C** (at.%)	**O** (at.%)
Near centre	44.70	44.56	1.43	2.12	0.51	5.78	0.90
Near edge	44.31	44.38	1.42	2.31	0.53	6.01	1.05
Near corner	44.67	44.77	1.38	1.77	0.53	5.79	1.10

4.7 MCT Film Grown by LPE on Substrate A

A film of $Hg_{1-x}Cd_xTe$ was grown on substrate A by LPE. Nomarski optical microscopy images revealed that the surface of the MCT film was non-planar in the form of wavy structures with a large number of circular features, as seen in Fig. 4.52. Two different types of circular features were observed: large circular defects with diameter of 25 µm–40 µm, as seen in Fig. 4.53a, and doughnut-shaped defects with a diameter of 10 µm–14 µm, as seen in Fig. 4.53b.

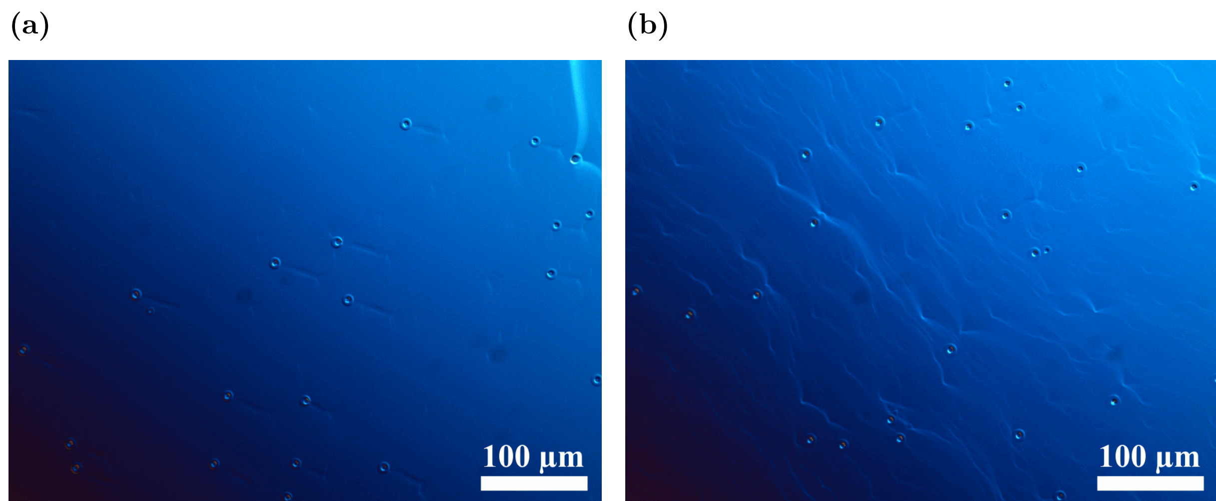

Figure 4.52: Nomarski phase contrast microscopy images of MCT film grown by LPE on (111)B-oriented substrate A: (a) Near the centre; and (b) near the right edge.

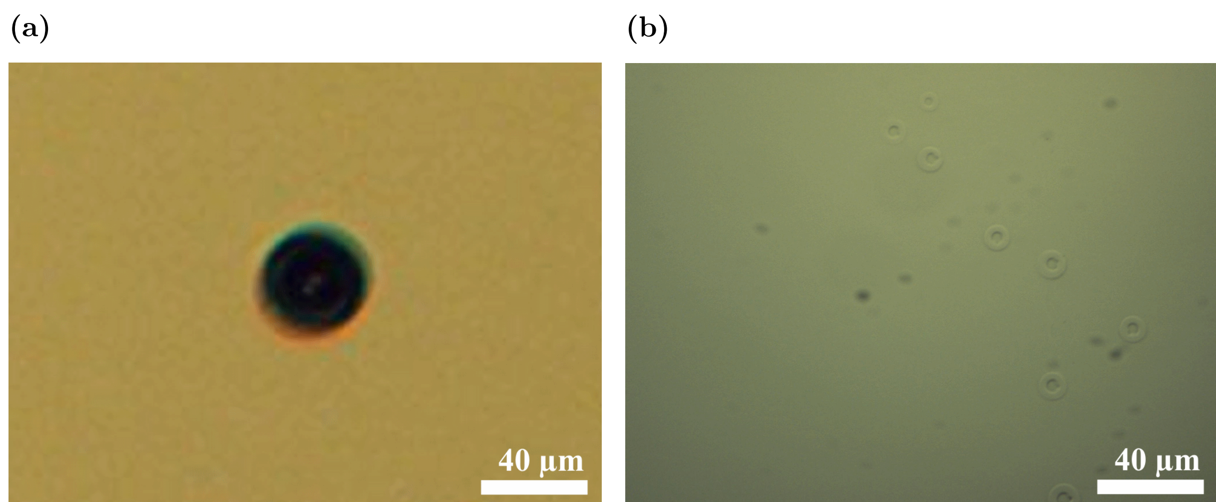

Figure 4.53: Bright field optical microscopy images of: (a) 40 µm wide defect; and (b) doughnut-shaped defects 10 µm wide seen on MCT film grown by LPE on (111)B-oriented substrate A.

The wavy structures, called terrace patterns in the literature, are typical of LPE growth and it has been confirmed that these patterns are caused by the misorientation of the substrate surface (Benz and Bauser, 1980; Parker et al., 1988). Li et al. (1998) showed that the best crystal quality was achieved with growth on 1.2°–2° off (111)A-oriented substrate. The LPE growth in this study was not performed under these conditions, and consequently, there were a lot of wavy structures.

The large defects were infrequent with respect to the doughnut-shaped defects. Only four large defects were observed in the lower right quadrant of the sample, which gave a density of $\sim 2\,\mathrm{cm}^{-2}$. The density of doughnut-shaped defects, on the other hand, was found to be between $4 \cdot 10^3\,\mathrm{cm}^{-2}$–$6 \cdot 10^4\,\mathrm{cm}^{-2}$. The average density was $2 \cdot 10^4\,\mathrm{cm}^{-2}$ with a standard deviation of $2 \cdot 10^4\,\mathrm{cm}^{-2}$. A graphical representation of the density at different locations on the film can be seen in Fig. 4.54. The sample Pearson correlation coefficient between the occurrence of polishing grit on substrate A and the occurrence of doughnut-shaped defects on the film was determined to be -0.04, which was a very weak negative correlation.

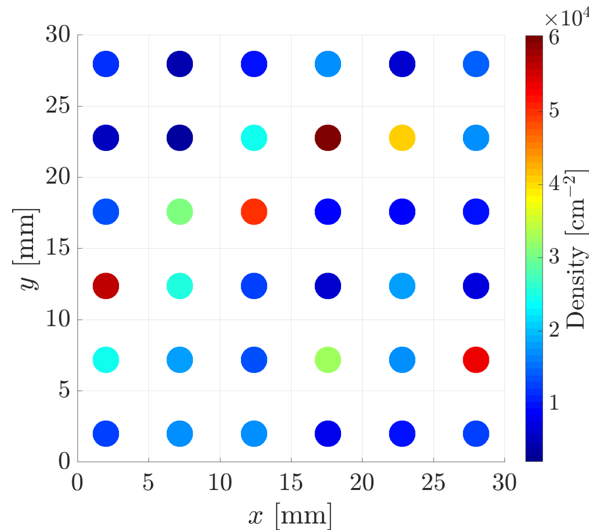

Figure 4.54: A map of the density of doughnut-shaped structures at 36 different locations on the 30 mm × 30 mm MCT film grown on substrate A. The density measurements were obtained by counting the number of doughnut-shaped defects in Nomarski optical microscopy images covering 558 µm × 419 µm areas. In total, 0.94 % of the substrate surface was measured. The density was observed to vary between $4 \cdot 10^3\,\mathrm{cm}^{-2}$–$6 \cdot 10^4\,\mathrm{cm}^{-2}$ with an average defect density of $2 \cdot 10^4\,\mathrm{cm}^{-2}$.

The doughnut-shaped defects had an elevated outer circle with a lowered centre, as seen in Fig. 4.55a. EDS spectra revealed that both the elevated and lowered part of the doughnut-

(a)

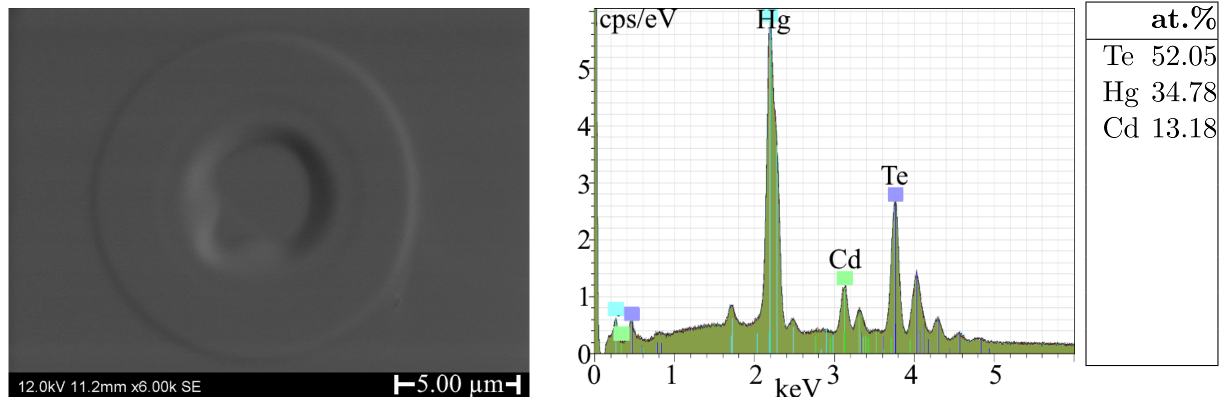

(b)

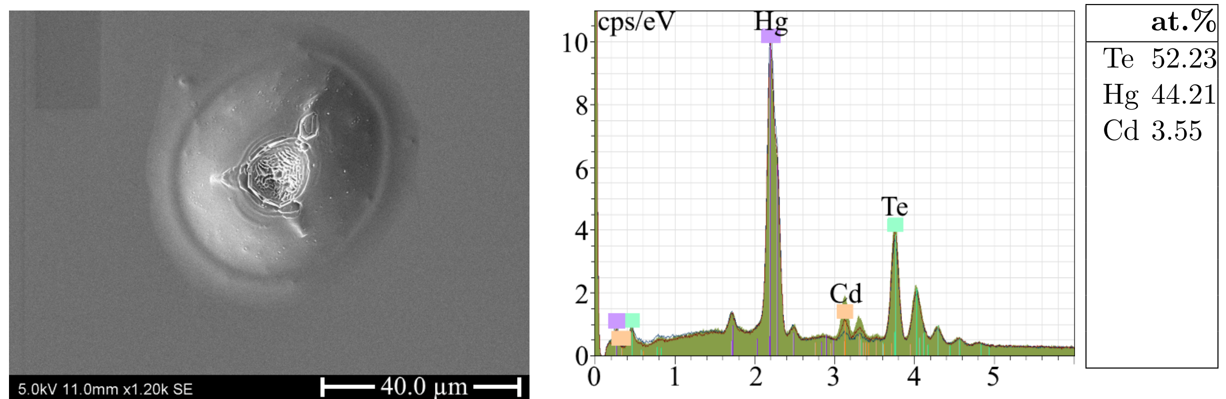

(c)

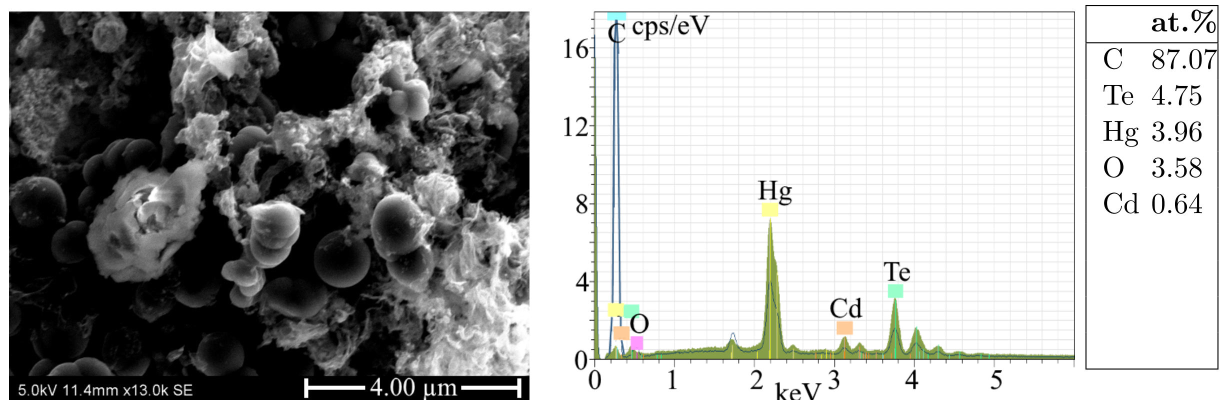

Figure 4.55: High-resolution SEM images of five different types of particles and defects found on the MCT film grown on substrate A and the corresponding EDS spectra and atomic compositions: (a) doughnut-shaped defect; (b) large circular defect; (c) carbon based particles; (d) boron nitride (B_2N_3) particle; and (e) MCT particle. The blue line represents the EDS spectrum of the particle, while the filled green represents the EDS spectrum of the underlying substrate.

(d)

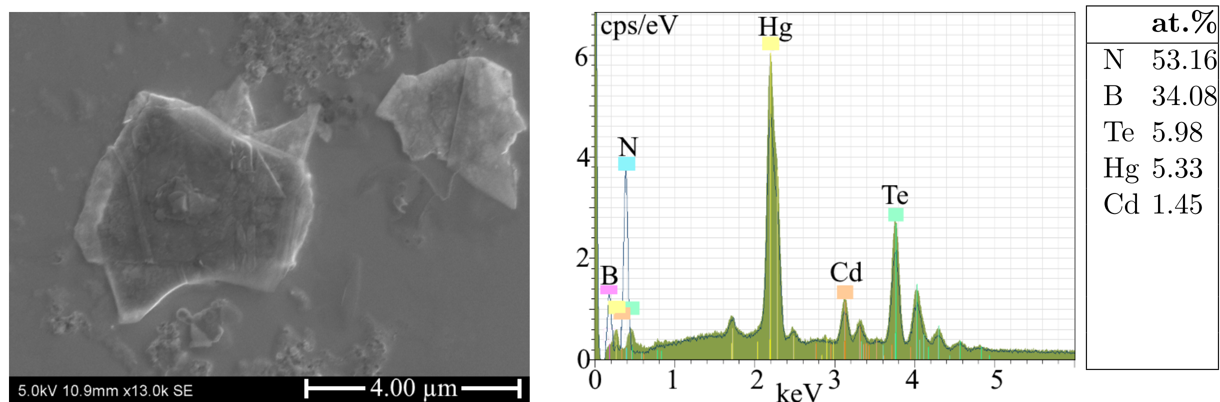

(e)

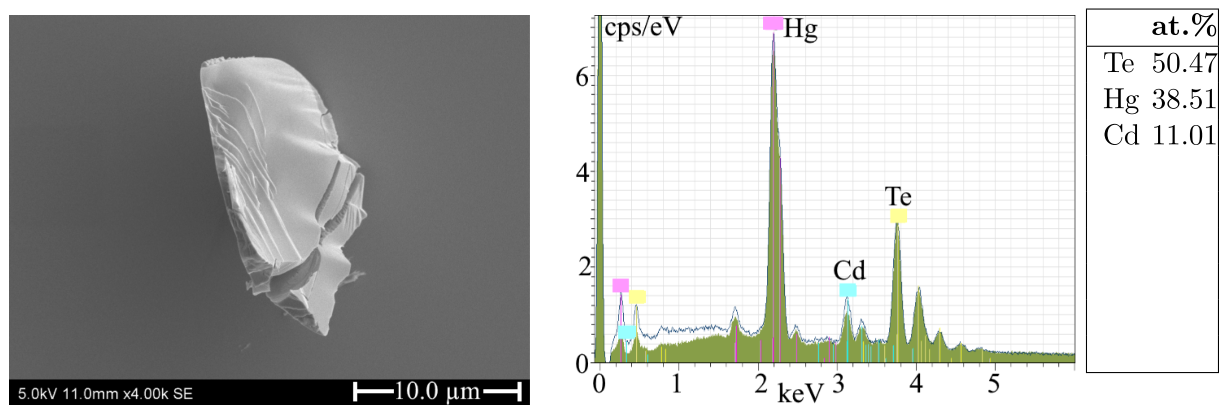

Figure 4.55: *(continued)*

shaped defect consisted of the same material as the surrounding substrate. According to Radhakrishnan et al. (2003), the doughnut-shaped defects appeared because of inherent substrate defects, i.e. oxides on the surface or graphite particles from the slider boat, which prevented the melt from wetting the surface, and hence, induced pits in the grown layer.

The large circular defects were pits in the substrate surface with a bright triangular shaped inclusion/precipitate inside them, as seen in Fig. 4.55b. The EDS spectrum of the centre of the defect revealed that it consisted of HgTe, while the EDS spectrum of the side walls of the pit revealed that they consisted of the same material as the surrounding substrate.

According to Pelliciari (1994), the density of large defects corresponds well with the density of tellurium precipitates in the substrate prior to growth. Pelliciari (1994) measured a density of large defects twice as big as the one measured on the film grown on substrate A.

It was observed that a few of the doughnut-shaped defects had residual particles trapped in the middle, as seen in Fig. 4.56. The particles were found to be carbon based, see Fig. 4.55c, and boron nitride (B_2N_3), see Fig. 4.55d. Boron nitride is a part of the LPE equipment where it keeps the substrate fixed during growth. The boron nitride piece was polished once in a while to remove residue from the growth process. It may be the debris from the polishing which had settled on the grown film.

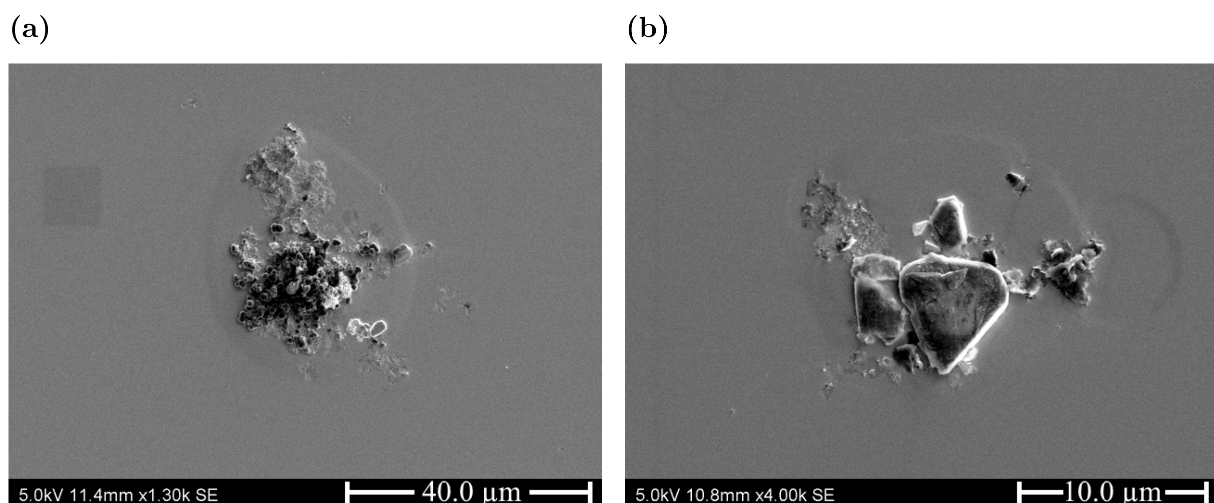

Figure 4.56: SEM images of doughnut-shaped defects filled with (a) carbon based particles and (b) boron nitride particles seen on MCT film grown by LPE on (111)B-oriented substrate A.

In addition to the particles found in connection with the doughnut-shaped defects, some MCT particles were found near the upper left corner of the substrate, see Fig. 4.55e.

4.7.1 Composition and Thickness

FTIR transmission spectra were recorded from the MCT film at the same 11×11 grid spots as before growth. The IR transmittance was between 6 %–40 % in the wavenumber range between $400\,\mathrm{cm}^{-1}$–$1400\,\mathrm{cm}^{-1}$, see Fig. 4.57. The film must be heat treated under annealing conditions to reduce the metal vacancy concentration before further fabrication. This will give increased transmission through the substrate. The average cut-on wavenumber was $2062.1\,\mathrm{cm}^{-1}$, which corresponds to a wavelength of 4.85 µm. Consequently, the x-value was 0.267 according to the Brice equation (Brice, 1975). The thickness of the MCT film was calculated to be on average 28.5 µm by using Eq. 2.16.

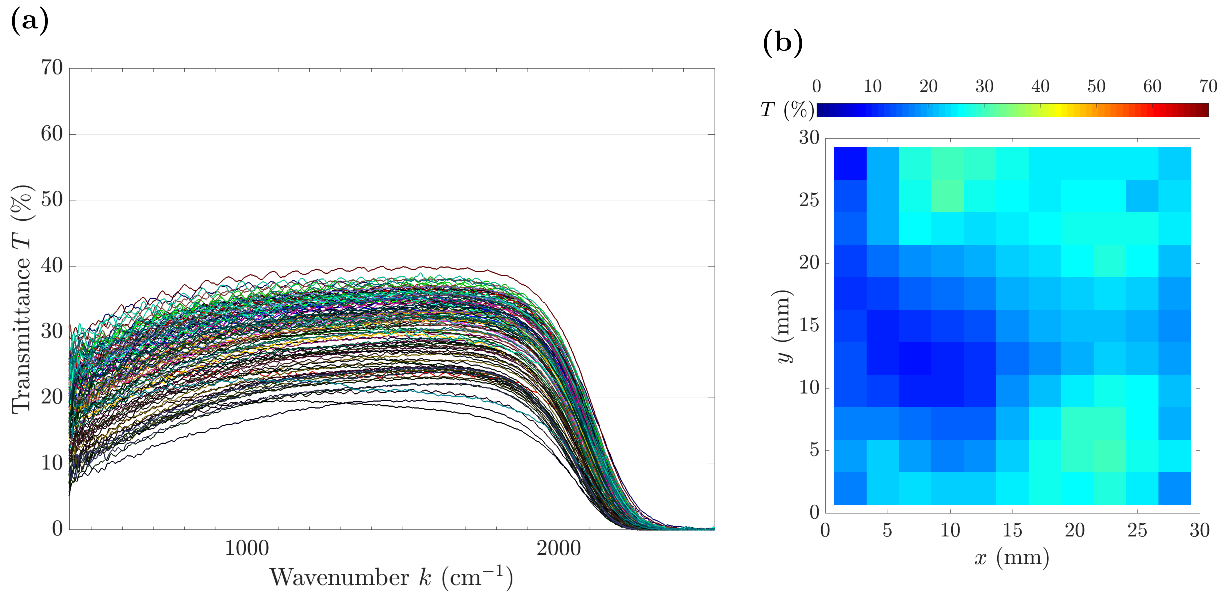

Figure 4.57: FTIR measurements recorded from a 11×11 grid on the $30\,\mathrm{mm} \times 30\,\mathrm{mm}$ MCT film grown on substrate A: (a) Transmission spectra; (b) transmission map at wavenumber $k = 500\,\mathrm{cm}^{-1}$ showing the transmittance T in percentage of incoming light at each grid point.

4.7.2 Impurity Analysis – EDS

EDS was used to get a quantitative analysis of the chemical composition of the MCT film grown by LPE on substrate A. The results can be seen in Table 4.8. The following

elements were identified: Te, Hg, Cd, C, O, and Al. The relative concentrations of Cd, Zn, and Te were $Hg_{0.71}Cd_{0.29}Te$, $Hg_{0.77}Cd_{0.23}Te$, and $Hg_{0.76}Cd_{0.24}Te$ for the centre, edge, and corner respectively. For the first time, Si was not found on the surface or in the outermost layer of the sample.

Table 4.8: Results of the EDS impurity analysis at three different locations on the 30 mm × 30 mm MCT film grown by LPE on (111)B-oriented substrate A (atomic concentration %). The X-ray signal was acquired from 1270 µm × 890 µm areas near the centre, upper edge, and upper left corner.

	Te (at.%)	**Hg** (at.%)	**Cd** (at.%)	**C** (at.%)	**O** (at.%)	**Al** (at.%)
Near centre	43.96	30.82	12.39	11.38	1.28	0.17
Near edge	43.87	33.27	9.80	11.70	1.13	0.23
Near corner	43.58	32.74	10.24	11.98	1.18	0.27

4.8 MCT Film Grown by LPE on Substrate B2

A film of MCT was grown on substrate B2 by LPE. Nomarski optical microscopy images revealed that the surface of the MCT film was non-planar in the form of wavy structures with a large number of circular features, as seen in Fig. 4.58. The same type of circular features were observed on this MCT film as the one grown on substrate A: Large circular defects with diameter of 38 µm–70 µm and doughnut-shaped defects with diameter of 8 µm–16 µm.

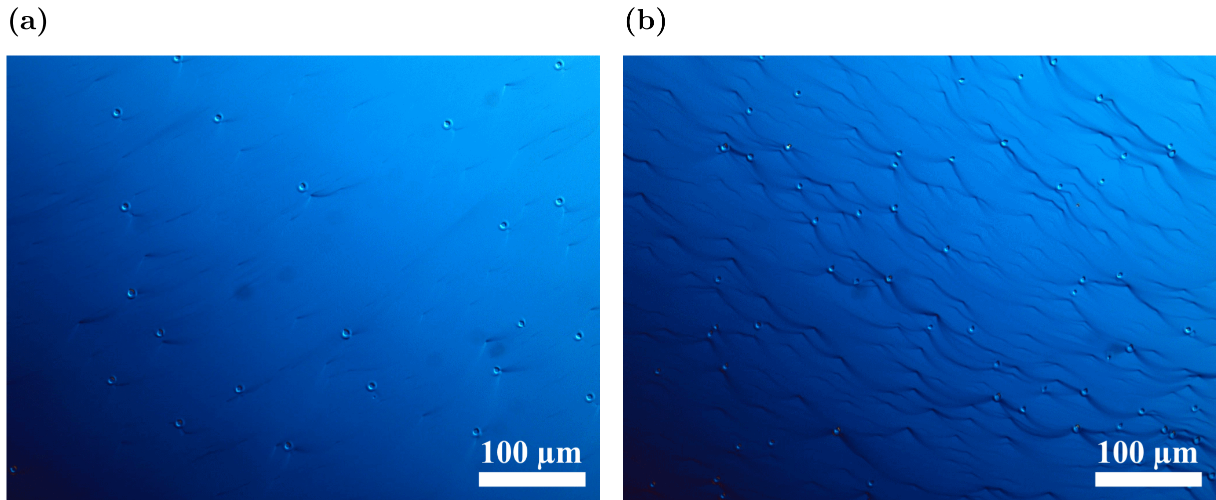

Figure 4.58: Nomarski phase contrast microscopy images of MCT film grown by LPE on (111)B-oriented substrate B2: (a) Centre; and (b) upper right corner.

Like for the MCT film on substrate A, the large defects on the MCT film on substrate B2 were infrequent with respect to the doughnut-shaped defects. Only four large defects were observed in the upper right quadrant of the sample. This gave a large circular defect density of $\sim 2\,\mathrm{cm^{-2}}$, which was the same as for film A. The density of doughnut-shaped defects was, on the other hand, found to be between $2 \cdot 10^3\,\mathrm{cm^{-2}}$–$3 \cdot 10^4\,\mathrm{cm^{-2}}$. The average density was $1 \cdot 10^4\,\mathrm{cm^{-2}}$, with a standard deviation of $5 \cdot 10^3\,\mathrm{cm^{-2}}$. The doughnut-shaped defects were more evenly distributed than on film A, as seen in the graphical representation of the density at different locations on the film in Fig. 4.59.

The sample Pearson correlation coefficient between the occurrence of polishing grit on substrate B2 and the occurrence of doughnut-shaped defects on the film was determined to be 0.68, which is a strong positive correlation. As the occurrence of polishing grit on substrate A and the occurrence of doughnut-shaped defects on the corresponding film showed no correlation, this relation should be investigated further in future studies.

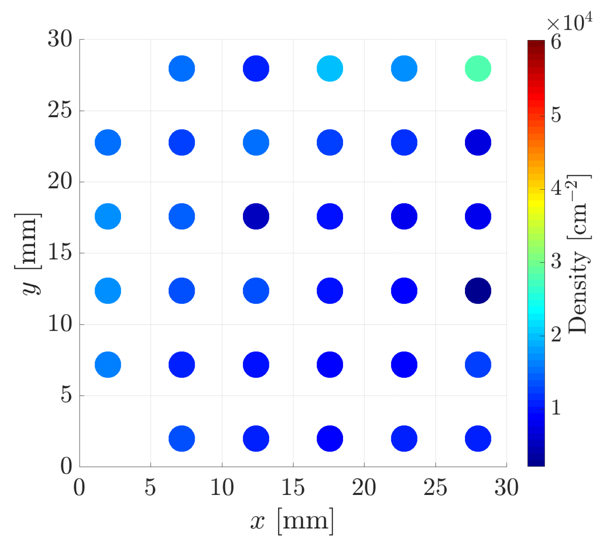

Figure 4.59: A map of the density of doughnut shaped structures at 34 different locations on the 30 mm × 30 mm MCT film grown on substrate B2. The density measurements were obtained by counting the number of doughnut-shaped defects in Nomarski optical microscopy images covering 558 µm × 419 µm areas. In total, 0.94 % of the substrate surface was measured. The density was observed to vary between $2 \cdot 10^3\,\text{cm}^{-2}$–$3 \cdot 10^4\,\text{cm}^{-2}$ with an average defect density of $1 \cdot 10^4\,\text{cm}^{-2}$.

Similarly to the film grown on substrate A, there were found spherical carbon-based particles and boron nitride particles in connection with a few of the doughnut-shaped defects. In addition, MCT particles was found towards the edges of the film.

4.8.1 Composition and Thickness

FTIR transmission spectra were recorded from the MCT film at the same 11×11 grid spots as before growth. The IR transmittance was between 0 %–42 % in the wavenumber range between 400 cm^{-1}–1400 cm^{-1}, see Fig. 4.60. As for the film grown on substrate A, this film must be annealed to reduce the metal vacancy concentration before further fabrication. The average cut-on wavenumber was 2083.3 cm^{-1}, which corresponds to a wavelength of 4.80 µm. Consequently, the x-value was 0.269 according to the Brice equation (Brice, 1975). The thickness of the MCT film was calculated to be on average 28.1 µm by using Eq. 2.16.

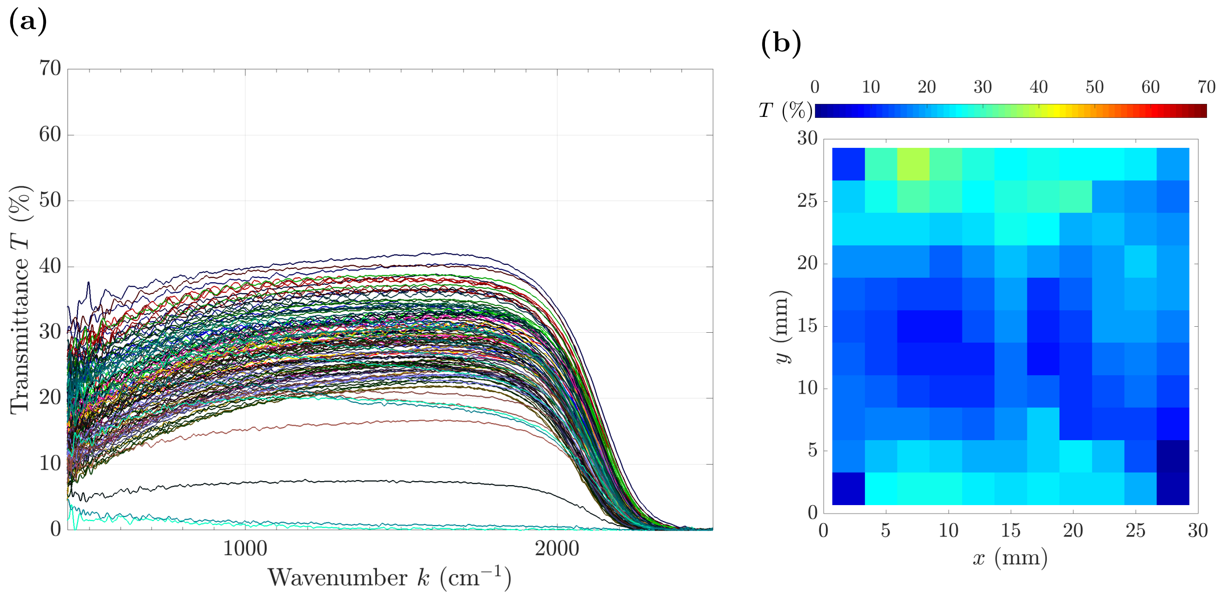

Figure 4.60: FTIR measurements recorded from a 11×11 grid on the 30 mm $\times$ 30 mm MCT film grown on substrate B2: (a) Transmission spectra; (b) transmission map at wavenumber $k = 500$ cm^{-1} showing the transmittance T in percentage of incoming light at each grid point.

4.8.2 Impurity Analysis – EDS

EDS was used to get a quantitative analysis of the chemical composition of the MCT

film grown by LPE on substrate A. The results can be seen in Table 4.9. The following elements were identified: Te, Hg, Cd, C, O, and Al. The relative concentrations of Cd, Zn, and Te were $Hg_{0.71}Cd_{0.28}Te_{1.01}$, $Hg_{0.74}Cd_{0.25}Te_{1.01}$, and $Hg_{0.74}Cd_{0.25}Te_{1.01}$ for the centre, edge, and corner respectively.

Table 4.9: Results of the EDS impurity analysis at three different locations on the 30 mm × 30 mm MCT film grown by LPE on (111)B-oriented substrate A (atomic concentration %). The X-ray signal was acquired from 1270 µm × 890 µm areas near the centre, upper edge, and upper left corner.

	Te (at.%)	**Hg** (at.%)	**Cd** (at.%)	**C** (at.%)	**O** (at.%)	**Al** (at.%)
Near centre	44.36	31.14	12.19	11.30	0.86	0.16
Near edge	44.12	32.26	10.81	11.49	1.14	0.18
Near corner	44.26	32.58	10.71	11.23	1.03	0.19

4.9 MCT Film Grown by MBE on Substrate C

A film of $Hg_{1-x}Cd_xTe$ was grown on substrate C by MBE. Bright field microscopy images revealed that the surface of the MCT film was planar with a large number of angular features, as seen in Fig. 4.61.

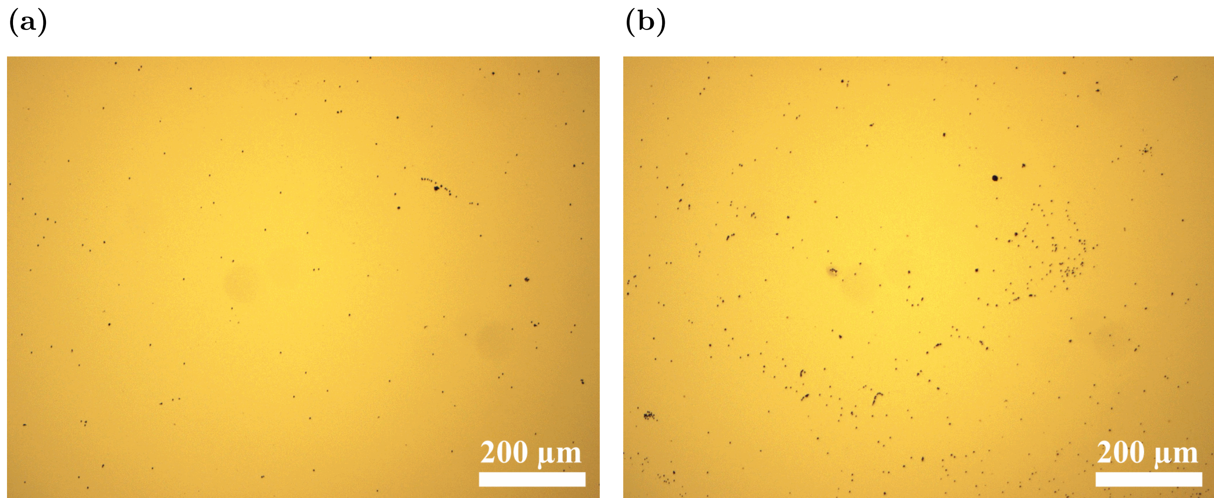

Figure 4.61: Bright field microscopy images of MCT film grown by MBE on (211)B-oriented substrate C: (a) Near the centre; and (b) near the lower left corner.

Selvig et al. (2007) describe the irregularly shaped defects with sizes extending from 10 µm to a few hundred microns as high temperature voids and the ones with size less than 10 µm as microvoids. These types of defects are typically formed during the growth of the material and the density is dependent on the deviation from ideal growth conditions. High temperature voids are formed at substrate temperatures higher than the Te-phase limit. Microvoids are formed at all substrate temperatures, but the density increases with lower substrate temperature. It was not observed any high temperature voids on the surface of the film, and hence, the film was grown at temperatures below the Te-phase limit.

The size of the microvoids was between 1 µm–3 µm. They were diamond-shaped with a longer axis towards the upper edge of the substrate and a shorter axis towards the right edge of the substrate, as seen in Fig. 4.62a. EDS point spectra across the microvoids showed no difference between the composition of the microvoid and the surrounding layer. The microvoids were either single, single with some smaller microvoids around their edges, or in clusters, as seen in Fig. 4.63. The clusters typically consisted of 3–6 microvoids.

The density of microvoids was found to be between $2 \cdot 10^4\ \mathrm{cm}^{-2}$–$1 \cdot 10^6\ \mathrm{cm}^{-2}$. The average

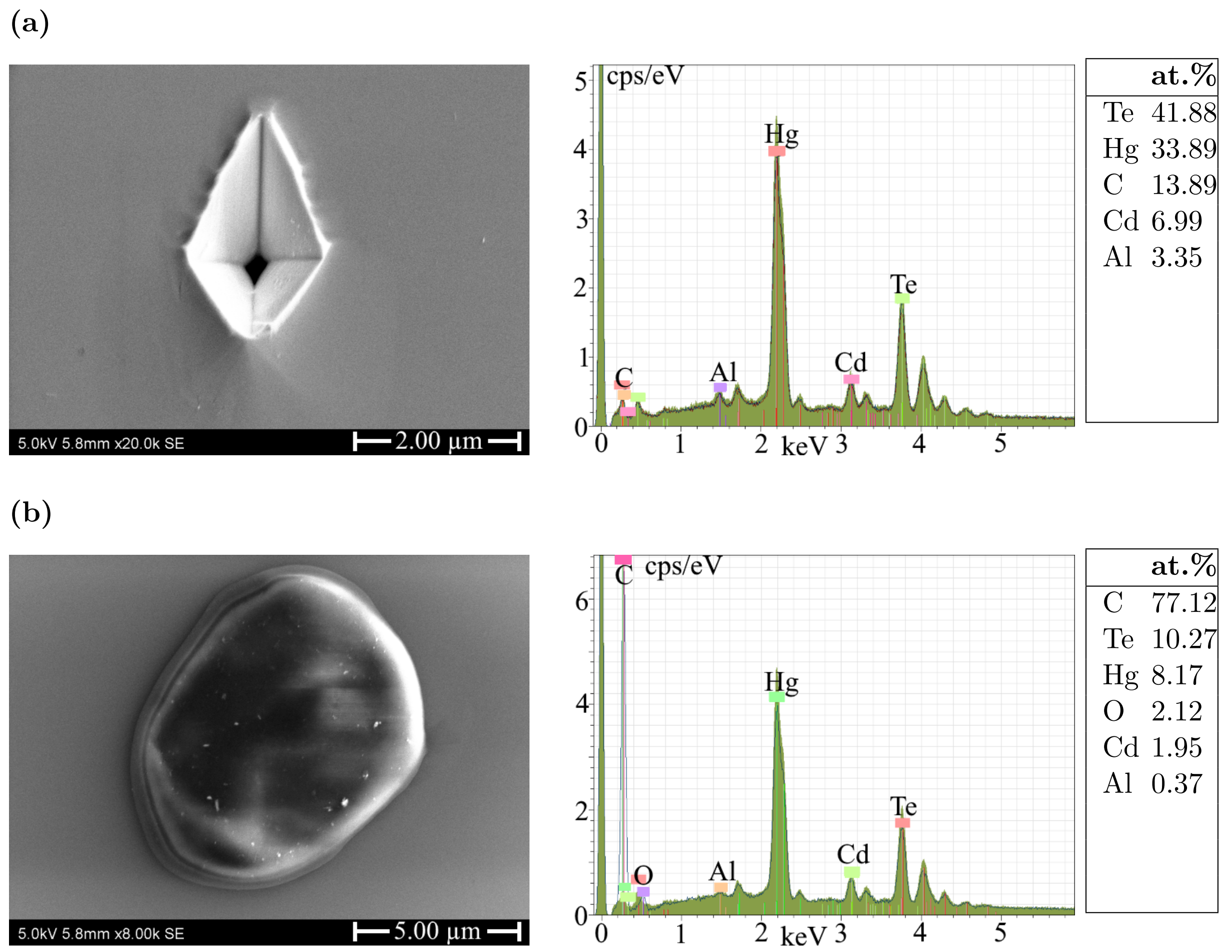

Figure 4.62: High-resolution SEM images of one defect and one particle found on the MCT film grown on substrate C and the corresponding EDS spectra and atomic compositions: (a) Microvoid; and (b) carbon based particle. The blue line represents the EDS spectrum of the particle, while the filled green represents the EDS spectrum of the underlying substrate.

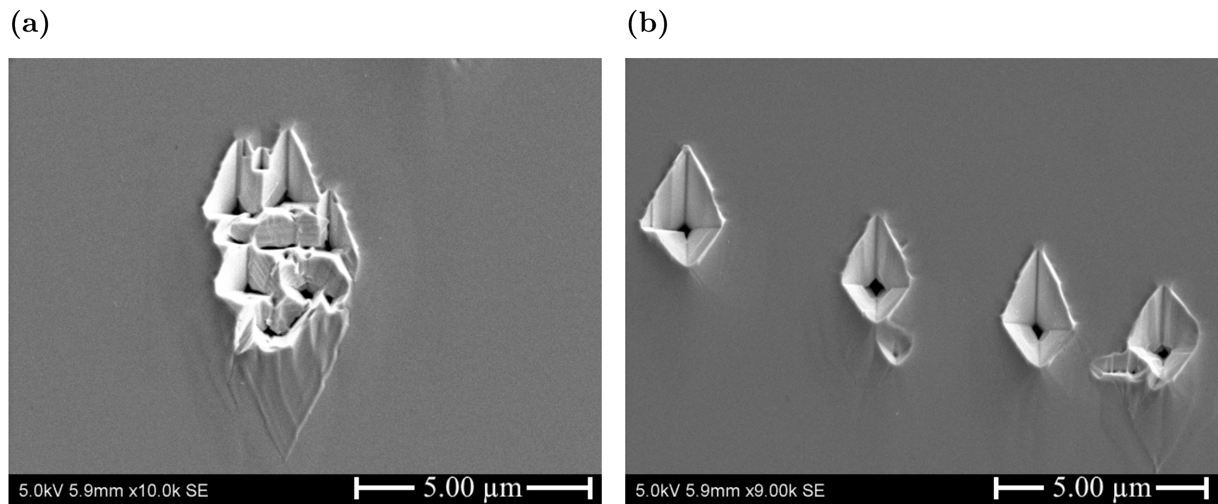

Figure 4.63: SEM images of microvoids found in MCT film grown by MBE on substrate C: (a) Cluster of diamond-shaped microvoids; and (b) single diamond-shaped microvoids, some with smaller microvoids around their edges.

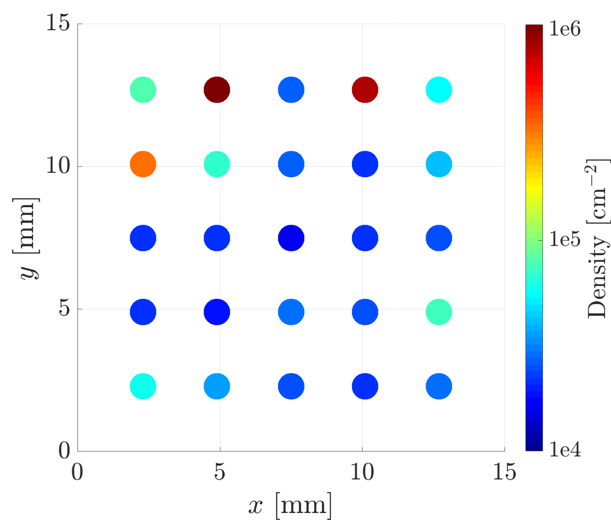

Figure 4.64: A map of the density of microvoids at 36 different locations on the 15 mm × 15 mm MCT film grown by MBE on substrate C. The density measurements were obtained by counting the number of microvoids in bright field optical microscopy images covering 558 µm × 419 µm areas. In total, 0.94 % of the substrate surface was measured. The density was observed to vary between $2 \cdot 10^4\,\text{cm}^{-2}$–$1 \cdot 10^6\,\text{cm}^{-2}$ with an average defect density of $1 \cdot 10^5\,\text{cm}^{-2}$.

density was $1 \cdot 10^5\,\mathrm{cm}^{-2}$ with a standard deviation of $3 \cdot 10^5\,\mathrm{cm}^{-2}$. The average density of the 3×3 centre points in the grid was $3 \cdot 10^4\,\mathrm{cm}^{-2}$, while the average density around the edges and corner was $2 \cdot 10^5\,\mathrm{cm}^{-2}$. A graphical representation of the density at different locations on the film can be seen in Fig. 4.64.

The sample Pearson correlation coefficient between the occurrence of polishing grit on the etched substrate C and the occurrence of microvoid defects on the film was determined to be 0.40, which is a moderate positive correlation. The residue from the evaporation of an acetone droplet, which settled on the surface while removing the etched substrate from the SEM holder, was clearly visible in the layer as a formation of microvoids, as seen in Fig. 4.65. As the density of microvoids was counted from a larger area than the area used to count the density of polishing grit, this correlation coefficient is not entirely accurate and it could be even higher as the images in Fig. 4.65 indicate.

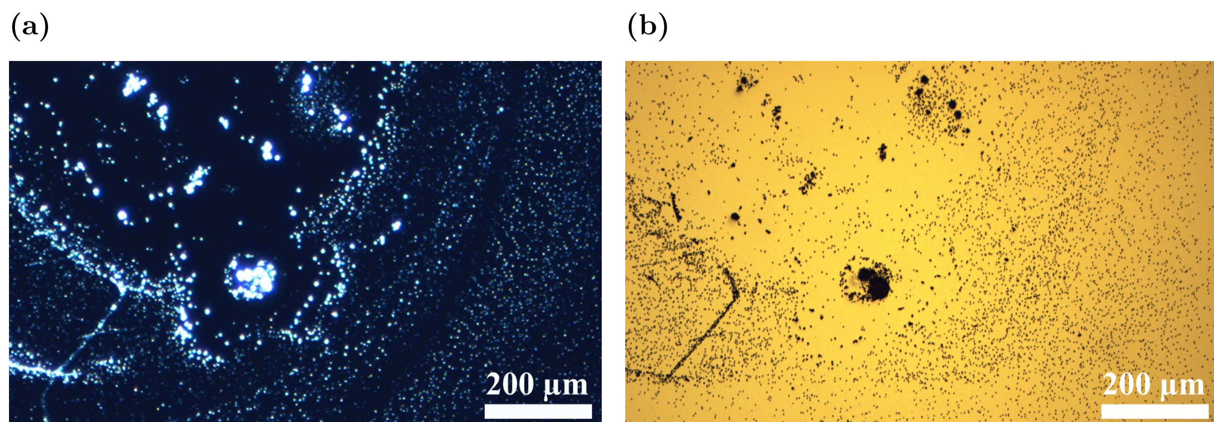

Figure 4.65: The residue from the evaporation of a acetone droplet on the etched substrate C was correlated with microvoids in the MCT film grown on substrate C: (a) Dark field microscopy image of etched substrate C; (b) bright field microscopy of MCT film.

A second type of defect was observed on the film. This was a round particle with a size of 4 µm–10 µm. The particle appeared darker than the substrate in SEM and did not have any sharp edges, as seen in Fig. 4.62b. The EDS spectrum of the particle revealed that it mainly consisted of carbon. This type of particle was infrequent with respect to the microvoids with a density of $\sim 1 \cdot 10^2\,\mathrm{cm}^{-2}$.

4.9.1 Composition and Thickness

An FTIR transmission spectrum was recorded from one spot in the centre of the MCT film. The IR transmittance was between 50 %–63 % in the wavenumber range between

400 cm^{-1}–1400 cm^{-1}, see Fig. 4.66. The cut-on wavenumber was 1564.7 cm^{-1}, which corresponds to a wavelength of 6.39 µm. Consequently, the x-value was 0.224 according to the Brice equation (Brice, 1975). The thickness of the MCT film was calculated to be 11.0 µm–11.6 µm by using Eq. 2.16.

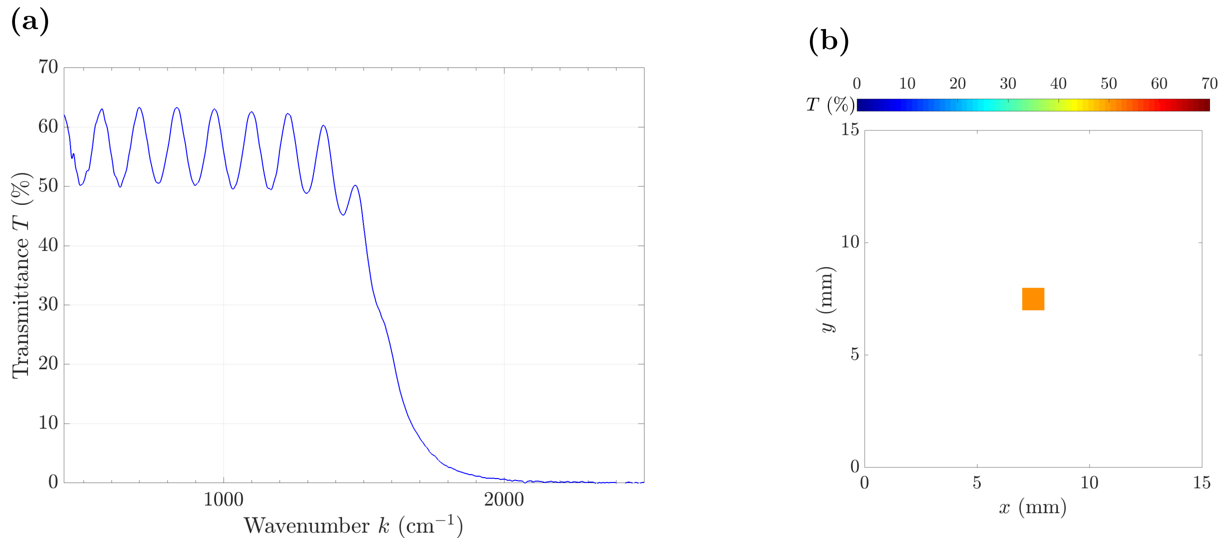

Figure 4.66: FTIR measurements recorded from one spot on the 15 mm × 15 mm MCT film grown on substrate C: (a) Transmission spectrum; (b) transmission map at wavenumber $k = 500\,\text{cm}^{-1}$ showing the transmittance T in percentage of incoming light at the point.

4.9.2 Impurity Analysis – EDS

EDS was used to get a quantitative analysis of the chemical composition of the MCT film grown by MBE on substrate C. The results can be seen in Table 4.10. The following elements were identified: Te, Hg, Cd, C, and Al. The relative concentrations of Cd, Zn, and Te were $Hg_{0.76}Cd_{0.24}Te$, which was a 0.02 percentage point difference from the value calculated from the FTIR spectrum.

Table 4.10: Results of the EDS impurity analysis at three different locations on the 15 mm × 15 mm MCT film grown by MBE on (211)B-oriented substrate C (atomic concentration %). The X-ray signal was acquired from 1270 µm × 890 µm areas near the centre, upper edge, and upper left corner.

	Te (at.%)	**Hg** (at.%)	**Cd** (at.%)	**C** (at.%)	**Al** (at.%)
Near centre	41.86	31.27	9.97	13.78	3.12
Near edge	41.81	31.23	9.84	13.77	3.36
Near corner	41.85	31.35	9.70	14.14	2.96

Chapter 5

Conclusions

In order to fabricate high-performance photovoltaic IR detectors, it is necessary to start with high-quality narrow-gap semiconductor material. MCT is the material of choice, as it has high absorption, high electron mobility, small lattice mismatch to CZT substrates, and it covers both the MWIR and the LWIR regions. One of the factors that influences the quality of the grown MCT material is the CZT substrate. Both the crystal quality and the surface preparation of the substrate is crucial to growing a good film. Therefore, a study of CZT substrates for LPE and MBE growth of MCT film was performed.

One (111)B substrate from vendor A (substrate A), two (111)B substrates from vendor B (substrate B and substrate B2), and one (211)B substrate from vendor A (substrate C) were investigated using bright and dark field microscopy, SEM, EDS, AFM, near-IR transmission microscopy, and FTIR. The substrates were investigated both as-received and after surface pre-growth preparation, except substrate B2, which was not investigated as-received. As the final step, an MCT film was grown on each substrate, except the shattered substrate B, and the same characterisation as was performed on the substrates was conducted to correlate the number of defects and the type of defects in the grown MCT layer with the preparation of the substrate.

The as-received substrate A had the best surface polish and crystal quality and had almost no particles on the surface. However, EDS spectra showed trace amounts of Al and Si on the surface even where no particles were seen in SEM. Surprisingly, substrate A got more particles on the surface after the etch procedure performed at FFI, which was undesirable. The additional particles might originate from silica grit left on the edges or underneath the substrate by the vendor's preparation method. Then, the particles were dissolved and

distributed over the surface during etching. The reason it had not been detected earlier was that LPE is somewhat forgiving of impurities on the surface, as there is a period of surface melting before the film starts to grow. Nevertheless, it will most likely influence the film quality.

The as-received substrate B had scratches, particles, and voids on the surface, and it had a larger surface roughness than the as-received substrate A by a factor of 10. The roughness decreased after the polishing procedure to about the same value as the etched substrate A. The number of particles also decreased, but it was not as low as on substrate A as-received or etched. Furthermore, the voids were indicative of poorer crystal quality than substrate A. Substrate A may, therefore, have earned the label of state-of-the-art both because of the surface preparation by the vendor and the crystal quality. The results from the polished substrate B was reproduced on the polished substrate B2. The low-transmission area in substrate B2 was visible in the SEM images by being brighter than the surrounding substrate. A possible explanation to the contrast in SEM is that the low-transmission area had a higher free carrier concentration, i.e. p-doped, than the surrounding substrate, which resulted in an increased SEM signal.

While the as-received (111)B-oriented substrate A from the same vendor had a density of polishing grit less than $2 \cdot 10^4\,\mathrm{cm}^{-2}$ on the surface, the (211)-oriented substrate C had an average density of $4 \cdot 10^7\,\mathrm{cm}^{-2}$. It could be the fact that the (211)-oriented surface was not atomically flat, but consisted of (111)-oriented steps, that caused the high density of polishing grit residue. The polishing grit density was reduced by a factor of 10 after the Br:methanol etch. The results from the characterisation of substrate C were similar to the results of Benson et al., but their etch seemed better than the one performed at FFI.

Observation of surface morphology of the MCT epilayers, which was grown by LPE on substrate A and substrate B2, showed wavy structures caused by thickness variations in the film, which are typical of LPE growth. In addition, doughnut-shaped defects and large circular defects were observed on the surface with a density of $1 \cdot 10^4\,\mathrm{cm}^{-2}$–$2 \cdot 10^4\,\mathrm{cm}^{-2}$ and $\sim 2\,\mathrm{cm}^{-2}$ respectively. The doughnut-shaped defects correlated with the polishing grit on substrate B2, but showed no correlation with the polishing grit on substrate A. The MCT epilayer, which was grown by MBE on substrate C, had a microvoid density of $1 \cdot 10^5\,\mathrm{cm}^{-2}$. The microvoids correlated with particles observed on the surface of the substrate before growth.

The findings in this thesis confirm that the surface preparation procedure is important for

the growth of high-quality MCT film. Substrate A had the lowest density of particles and defects on the surface and the highest crystal quality, but the surface preparation needs to be improved. Further understanding of how to perfect the substrate surface could be the key to making even better infrared detector elements.

Chapter 6

Recommendations for Future Work

It would be useful to repeat the measurements on an additional (111)B-oriented substrate from vendor A to verify that the results from this study are reproducible, both in regards to the low density of particles on the as-received surface and the higher density after etch. The source of the grit particles that appeared on the surface after etch should be located by studying the bevelled edges and underneath the substrate, e.g. using SEM with EDS.

If the polishing grit observed on the etched surface of substrate A is revealed to originate from the substrate itself, ways to remove particles from the bevelled edges and underneath the substrate should be found. Possible methods could be rubbing a cleanroom swab soaked in solvent around the edges, mounting the substrate upside down to be able to remove particles from underneath, and try other standard semiconductor cleaning techniques (Reinhardt and Kern, 2008).

Then, different preparation etch procedures, i.e. shorter etch time or spray etching, should be examined. Seeing that Benson et al. (2016) reports that their Br:methanol-based MBE preparation etch removes residual SiO_2 polishing grit from the substrates, a procedure that replicates their results should be developed.

A possible improvement of the preparation polish procedure could be to use both silica and alumina polishing grit during polishing. At the moment, alumina is used alone as the abrasive in the polishing procedure, but as both silica and alumina were present on the as-received substrates from vendor A, it could be assumed that a combination of these two is advantageous.

As a final test of the new preparation method, MCT films should be grown on one substrate prepared by the new method and one prepared by the old method. It would be interesting to compare the material properties and the quality of the resulting IR detector element of the two films.

Appendix A

Summary and Comparison of the Substrates

A summary of the different particles and features, the particle and feature density, and the RMS roughness that were observed on the substrate surfaces can be seen in Table A.1, Table A.2, and Table A.3 respectively. The density of the defects that were observed on the MCT films, which were grown on substrate A, substrate B2, and substrate C, can be seen in Table A.4.

Table A.1: Comparison of the types of particles observed on the four CZT substrates which have been studied. A tick (✓) identifies for which substrates the feature given in the first column was present, while a dash (—) points out for which substrates the feature was not observed.

	A as-received	**A** pre-growth	**B** as-received	**B** pre-growth	**B2** pre-growth	**C** as-received	**C** pre-growth
Polishing grit	✓	✓	✓	✓	✓	✓	✓
Voids	—	—	✓	—	—	—	—
CZT	✓	—	✓	✓	✓	—	—
HgTe	—	—	—	✓	✓	—	—
C-based	—	✓	✓	✓	✓	✓	✓
Ti	✓	—	—	—	—	—	—
NaClO	—	—	✓	—	—	—	—
Fe	—	—	✓	—	—	—	—

Table A.2: Comparison of the density of polishing grit, features with size >0.5 µm, and voids on the four CZT substrates which have been studied. A dash (—) points out for which substrates the feature was not observed. The density of the observed features are given for the substrates both as-received and with surface pre-growth preparation (cm^{-2}).

	A as-received	**A** pre-growth	**B** as-received	**B** pre-growth	**B2** pre-growth	**C** as-received	**C** pre-growth
Polishing grit	$<2 \cdot 10^4$	$2 \cdot 10^6$	$6 \cdot 10^5$	$7 \cdot 10^6$	$1 \cdot 10^7$	$3 \cdot 10^7$	$3 \cdot 10^6$
>0.5 µm	$4 \cdot 10^2$	$1 \cdot 10^3$	$1 \cdot 10^5$	$5 \cdot 10^3$	$5 \cdot 10^3$	$3 \cdot 10^1$	$8 \cdot 10^3$
Voids	—	—	$7 \cdot 10^3$	—	—	—	—

Table A.3: Comparison of the RMS roughness in the centre of the four CZT substrates which have been studied. The roughness was calculated from AFM measurements taken of a 5 µm × 5 µm area in the centre of the substrate. The RMS roughness are given for the substrates both as-received and with surface pre-growth preparation (nm).

A as-received	**A** pre-growth	**B** as-received	**B** pre-growth	**B2** pre-growth	**C** as-received	**C** pre-growth
0.31	0.51	3.7	0.85	0.91	0.95	1.4

Table A.4: Comparison of the defects in the MCT films that were grown on the CZT substrates which have been studied. A tick (✓) identifies for which substrates the feature given in the first column was present, a dash (—) points out for which films the feature was not observed, and a number represents the density of the feature (cm^{-2}).

	A film	**B** film	**C** film
Wavy structures	✓	✓	—
Large circular defects	∼2	∼2	—
Donut-shaped defects	$2 \cdot 10^4$	$1 \cdot 10^4$	—
Microvoids	—	—	$1 \cdot 10^5$
Carbon-based particles	✓	✓	✓
Boron nitride particles	✓	✓	—
MCT particles	✓	✓	—

References

Allen, E., Smith, P., and Henshaw, J. (2001). *A Review of Particle Agglomeration*. US Department of Energy.

Ashida, K., Kajino, T., Kutsuma, Y., Ohtani, N., and Kaneko, T. (2015). Crystallographic orientation dependence of SEM contrast revealed by SiC polytypes. *Journal of Vacuum Science & Technology B, Nanotechnology and Microelectronics: Materials, Processing, Measurement, and Phenomena*, 33(4):04E104.

Benson, J. D., Bubulac, L. O., Jaime-Vasquez, M., Lennon, C. M., Arias, J. M., Smith, P. J., Jacobs, R. N., Markunas, J. K., Almeida, L. A., Stoltz, A., Wijewarnasuriya, P. S., Peterson, J., Reddy, M., Jones, K., Johnson, S. M., and Lofgreen, D. D. (2016). Analysis of etched CdZnTe substrates. *Journal of Electronic Materials*, pages 1–9.

Benson, J. D., Bubulac, L. O., Jaime-Vasquez, M., Lennon, C. M., Smith, P. J., Jacobs, R. N., Markunas, J. K., Almeida, L. A., Stoltz, A., Arias, J. M., Wijewarnasuriya, P. S., Peterson, J., Reddy, M., Vilela, M. F., Johnson, S. M., Lofgreen, D. D., Yulius, A., Carmody, M., Hirsch, R., Fiala, J., and Motakef, S. (2015). As-received CdZnTe substrate contamination. *Journal of Electronic Materials*, 44(9):3082–3091.

Benson, J. D., L. O. Bubulac, P. J. S., Jacobs, R. N., Markunas, J. K., Jaime-Vasquez, M., Almeida, L. A., Stoltz, A., Wijewarnasuriya, P. S., Brill, G., Chen, Y., Peterson, J., Reddy, M., Vilela, M. F., Johnson, S. M., Lofgreen, D. D., Yulius, A., Bostrup, G., Carmody, M., Lee, D., and Couture, S. (2014). Impact of tellurium precipitates in CdZnTe substrates on MBE HgCdTe deposition. *Journal of Electronic Materials*, 43(11):3993–3998.

Benz, K. and Bauser, E. (1980). Crystals: Growth, properties, and applications. *Springer, Berlin*, page 2.

Bhushan, B. (1998). *Handbook of micro/nano tribology.* CRC press.

Birdi, K. (2003). *Scanning probe microscopes: applications in science and technology.* CRC press.

Brandon, D. and Kaplan, W. D. (2013). *Microstructural characterization of materials.* John Wiley & Sons.

Brice, J. (1975). Some thermodynamic aspects of the growth of strained crystals. *Journal of Crystal Growth*, 28(2):249–253.

Briggs, D. and Seah, M. P. (1990). *Practical Surface Analysis: Auger and X-ray Photo-electron Spectroscopy*, volume 1. John Wiley & Sons.

Bruker (2008). *Quantax Microanalysis system based on energy-dispersive spectrometry. User manual.* Bruker-AXS Microanalysis GmbH, Berlin, Germany.

de Broglie, L. (1924). *Recherches sur la théorie des quanta.* PhD thesis, Migration-université en cours d'affectation.

Dhar, N. K., Dat, R., and Sood, A. K. (2013). *Advances in Infrared Detector Array Technology.* INTECH Open Access Publisher.

Eaton, P. and West, P. (2010). *Atomic force microscopy.* Oxford University Press.

Edwall, D., Gertner, E., and Tennant, W. (1984). Liquid phase epitaxial growth of large area $Hg_{1-x}Cd_xTe$ epitaxial layers. *Journal of applied physics*, 55(6):1453–1460.

Egan, C., Dabrowski, P., Klusek, Z., and Brinkman, A. (2009). A scanning probe microscopy study of $Cd_{1-x}Zn_xTe$. *Journal of electronic materials*, 38(8):1528–1532.

Everson, W., Ard, C., Sepich, J., Dean, B., Neugebauer, G., and Schaake, H. (1995). Etch pit characterization of cdte and cdznte substrates for use in mercury cadmium telluride epitaxy. *Journal of electronic materials*, 24(5):505–510.

Goldstein, J., Newbury, D. E., Echlin, P., Joy, D. C., Romig Jr., A. D., Lyman, C. E., Fiori, C., and Lifshin, E. (2012). *Scanning electron microscopy and X-ray microanalysis: a text for biologists, materials scientists, and geologists.* Springer Science & Business Media.

Griffiths, P. R. and De Haseth, J. A. (2007). *Fourier transform infrared spectrometry,*

volume 171. John Wiley & Sons.

Hansen, G. L., Schmit, J. L., and Casselman, T. N. (1982). Energy gap versus alloy composition and temperature in $Hg_{1-x}Cd_xTe$. *Journal of Applied Physics*, 53(10):7099–7101.

Hirsch, L., Haakenaasen, R., Colin, T., Ziemer, K., Stinespring, C., Lovold, S., and Myers, T. (1999). X-ray photoelectron spectroscopy study of oxide and Te overlayers on as-grown and etched HgCdTe. *Journal of electronic materials*, 28(6):810–816.

Lauten, O. (2017). Characterisation of As-Received CdZnTe Substrates. Specialisation Project, Norwegian University of Science and Technology, unpublished.

Lee, B., Gan, T., Boning, D., Hester, P., Poduje, N., and Baylies, W. (2000). Nanotopography effects on chemical mechanical polishing for shallow trench isolation. In *Advanced Semiconductor Manufacturing Conference and Workshop, 2000 IEEE/SEMI*, pages 425–432. IEEE.

Li, B., Zhang, X., Zhu, J., and Chu, J. (1998). Crystallinity improvement of $Hg_{1-x}Cd_xTe$ films grown by a liquid-phase epitaxial technique. *Journal of Crystal Growth*, 184/185:1242–1246.

Liboff, R. L. (2003). *Introductory quantum mechanics*. Addison-Wesley.

Moulder, J. F., Stickle, W. F., Sobol, P. E., and Bomben, K. D. (1995). Handbook of x-ray photoelectron spectroscopy: a reference book of standard spectra for identification and interpretation of XPS data. *Physical Electronics*.

Naval Air Warfare Center (2013). *Electronic warfare and radar systems: Engineering handbook*. Naval Air Warfare Center.

Nicolet, T. (2001). Introduction to Fourier transform infrared spectrometry. *Thermo Nicolet Corporation*.

Parker, S., Weirauch, D., and Chandra, D. (1988). Terracing in HgCdTe LPE films grown from Te solution. *Journal of Crystal Growth*, 86(1-4):173–182.

Pelliciari, B. (1994). Te-rich liquid-phase epitaxy of $Hg_{1-x}Cd_xTe$. *Progress in crystal growth and characterization of materials*, 29(1-4):1–39.

PSIA (2002). *XE-100 High Accuracy Small Sample SPM. User's Manual*. PSIA Corpo-

ration, Sungnam, Korea.

Radhakrishnan, J., Sitharaman, S., and Gupta, S. (2003). Surface morphology of $Hg_{0.8}Cd_{0.2}Te$ epilayers grown by LPE using horizontal slider. *Applied Surface Science*, 207(1):33–39.

Rayleigh, L. (1879). Investigations in optics, with special reference to the spectroscope. *Philosophical Magazine and Journal of Science Series 5*, 8(49):261–274, 403–411, 477–486.

Rayleigh, L. (1880). Investigations in optics, with special reference to the spectroscope. *Philosophical Magazine and Journal of Science Series 5*, 9:40–55.

Reddy, M., Lofgreen, D., Jones, K., Peterson, J., Radford, W., Benson, J., and Johnson, S. (2013). Cross-sectional study of macrodefects in MBE dual-band HgCdTe on CdZnTe. *Journal of electronic materials*, 42(11):3114.

Reinhardt, K. and Kern, W. (2008). *Handbook of silicon wafer cleaning technology.* William Andrew.

Sealy, C. P., Castell, M. R., and Wilshaw, P. R. (2000). Mechanism for secondary electron dopant contrast in the SEM. *Journal of electron microscopy*, 49(2):311–321.

Selvig, E., Tonheim, C., Kongshaug, K., Skauli, T., Hemmen, H., Lorentzen, T., and Haakenaasen, R. (2008a). Defects in CdHgTe grown by molecular beam epitaxy on (211)B-oriented CdZnTe substrates. *Journal of Vacuum Science & Technology B*, 26(2):525–533.

Selvig, E., Tonheim, C., Kongshaug, K., Skauli, T., Lorentzen, T., and Haakenaasen, R. (2007). Defects in HgTe grown by molecular beam epitaxy on (211)B-oriented CdZnTe substrates. *Journal of Vacuum Science & Technology B*, 25(6):1776–1784.

Selvig, E., Tonheim, C., Lorentzen, T., Kongshaug, K., Skauli, T., and Haakenaasen, R. (2008b). Defects in HgTe and CdHgTe grown by molecular beam epitaxy. *Journal of Electronic Materials*, 37(9):1444–1452.

Sivananthan, S., Chu, X., Reno, J., and Faurie, J. (1986). Relation between crystallographic orientation and the condensation coefficients of Hg, Cd, and Te during molecular-beam-epitaxial growth of $Hg_{1-x}Cd_xTe$ and CdTe. *Journal of applied physics*, 60(4):1359–1363.

Smith, B. C. (2011). *Fundamentals of Fourier transform infrared spectroscopy.* CRC press, 2nd edition.

Smith, G. T. (2013). *Industrial metrology: surfaces and roundness.* Springer Science & Business Media.

Stuart, B., George, B., and Mclntyre, P. (2008). *Modern Infrared Spectroscopy.* John Wiley & Sons.

Tanuma, S., Powell, C. J., and Penn, D. R. (1991). Calculations of electron inelastic mean free paths. ii. data for 27 elements over the 50–2000 ev range. *Surface and Interface Analysis*, 17(13):911–926.

Thomas, T. R. (1999). Amplitude parameters. In *Rough Surfaces*, pages 133–150. Imperial College Press, London.

Triboulet, R. and Siffert, P. (2009). *CdTe and Related Compounds; Physics, Defects, Hetero-and Nano-structures, Crystal Growth, Surfaces and Applications, Part I: Physics, CdTe-based Nanostructures, CdTe-based Semimagnetic Semiconductors, Defects.* Elsevier.

Wang, T., Jie, W., and Zeng, D. (2008). Observation of nano-scale Te precipitates in cadmium zinc telluride with HRTEM. *Materials Science and Engineering: A*, 472(1):227–230.

Yadava, R., Sundersheshu, B., Anandan, M., Bagai, R., and Borle, W. (1994). Precipitation in CdTe crystals studied through Mie scattering. *Journal of electronic materials*, 23(12):1349–1357.

Yujie, L., Zhi, G., Guoqiang, L., and Wangqi, J. (2004). Infrared transmission spectra of $Cd_{1-x}Zn_xTe$ (x = 0.04) crystals. *Journal of electronic materials*, 33(8):861–866.